論文 / 著書情報
Article / Book Information

題目(和文)	陰イオン包接C12A7および鉄ヒ化物超伝導体の結晶化学に関する研究
Title(English)	Study on crystal chemistry of anion-encaged C12A7 and iron arsenide superconductors
著者(和文)	野村尚利
Author(English)	Takatoshi Nomura
出典(和文)	学位:博士(工学), 学位授与機関:東京工業大学, 報告番号:甲第8015号, 授与年月日:2010年3月26日, 学位の種別:課程博士, 審査員:細野 秀雄,神谷 利夫
Citation(English)	Degree:Doctor (Engineering), Conferring organization: Tokyo Institute of Technology, Report number:甲第8015号, Conferred date:2010/3/26, Degree Type:Course doctor, Examiner:,
学位種別(和文)	博士論文
Type(English)	Doctoral Thesis

Study on Crystal Chemistry of Anion-encaged C12A7 and Iron Arsenide Superconductors

by

Takatoshi Nomura

Department of Materials Science and Technology

Tokyo Institute of Technology

2009

Contents

Chapter 1: General Introduction

Crystal structure is one of the important factors to determine the physical and chemical properties of function materials. Hosono laboratory at Tokyo Institute of Technology has been developed many intriguing functional materials by taking advantages of various unique structures of oxides. By using nanospaces in crystals such as the nanocage structure in C12A7 ($12CaO{\cdot}7Al_2O_3$) and the channel structure in apatites, the incorporation of active anions, such as oxygen radical ions (i.e. O_2^-, O^-) and H^- ions, have been tried for applications to catalytic agents and anion storage, even though they are known as good oxygen ion conductors. In addition, two-dimensional layered structure is applied to transparent *n*- or *p*-type semiconductors and catalytic agents (e.g. IGZO, LaCuOS and delafossite). A recently-discovered iron arsenide superconductor, LaFeAsO also have a layered crystal structure and unique Fe tetragonal planes contributing to the high-T_c superconductivity. The above mentioned unique properties could be more or less attributed to the characteristic crystal structures. To achieve further developments and to search new functional materials, detailed researches on the crystal structures are required to gain deeper insight into them.

In this study, I focused on various anion-incorporated C12A7 crystals and iron arsenide high-T_c superconductors, and the relation between the physical properties and the crystal structure was investigated and discussed from the viewpoint of crystal chemistry to reveal the origins of the properties. In this chapter, firstly, the backgrounds of the two material systems are reviewed, and then, the objective and the outline of this study are summarized.

1.1. Novel Properties and Unique Crystal Structure of C12A7

1.1.1. Nanoporous Crystal C12A7 and Various Encaged-anion Species

A nanoporous crystal, $12CaO \cdot 7Al_2O_3$ (C12A7) is known as one of cement components in the $CaO\text{-}Al_2O_3$ system since early times and the glass state was studied due to the curious behaviors [1]. The crystal structures of C12A7 are shown in Fig. 1-1. The structure is constructed of only one type of cage structure with inner free space of ~0.4 nm. The cages are linked three-dimensionally, sharing the framework with each other. Each unit cell contains 12 cages and can be denoted as $[Ca_{24}Al_{28}O_{64}]^{4+} \cdot 2O^{2-}$; the lattice framework has four positive elemental charges per unit cell, thus one-third charge is allocated to each cage. The positive charge is compensated by O^{2-} ions which randomly incorporated one-sixth of the cages in the stiochiometric composition. The O^{2-} ions are not belongs to the framework, therefore, it is called as 'extra-framework oxide ions'. C12A7 is known as a fast ionic conductor due to the extra-framework oxide ions which can migrate the three-dimensionally linked cages at high temperature [2].

The extra-framework oxide ion can be partially or completely replaced by other anions; for example, OH^- [3,4], O_2^- [2,5], O^- [5,6], F^- [7,8], Cl^- [7,9], H^- [10] and Au^- [11]. Especially, oxygen radicals (ex. O_2^-, O^-) and H^- ions are unstable active anion species at ambient temperature and pressure, however, they can remain stable even at a few hundred Celsius degrees in the C12A7 crystal. The oxygen radicals or the H^- ions can be incorporated in the cage only by annealing at O_2 or H_2 gas atmosphere at suitable temperatures [5,6,10]. The incorporation of these active anions drastically changes the properties of C12A7: The C12A7 encaging oxygen radicals exhibits outstanding oxidative reactivity enough to oxidize Pt metal [10]. Taking advantage of super-oxidation ability, catalytic applications such as O^- beam generator have been tried [12]. Whereas, the H^- incorporated C12A7 is colorless insulator in the

as grown state, however, UV irradiation changes its color to light green and induces persistent conductivity with ~1 $S \cdot cm^{-1}$. The conductive state can be reversed to the initial state by annealing at 300°C for a few hours. It is noteworthy that C12A7 defied the common sense that oxides composed only by light elements would not exhibit electronic conduction. C12A7 is only composed by abundant and eco-friendly elements, therefore, it possibly sheds light on the developments of transparent conductors where the depletion of rare elements like as Indium is serious problem.

1.1.2. Chemical Properties and Metal-Insulator Transition of C12A7electride

In addition to above-mentioned various anion species, electrons (e^-) can be incorporated in the framework of C12A7 [13]. The reduction process of a single crystal of C12A7 using base metal (e.g. Ca metal) extracts the extra-framework oxide ions from the crystal, instead, electrons are incorporated in the cages to balance the total charge. The electron encaged C12A7 is stable at ambient temperature and exhibits electron conduction contrast to the insulative stiochiometric C12A7. The electron concentration can be roughly tunable by changing the reduction temperature and time. The sample color changes from colorless to yellow, green, and finally black according to the degree of reduction process (i.e. electron concentration).

The crystals in which the trapped electrons behave as anions can be called as “electrides”. The first report of electrides is $Cs^+(18\text{-crown-}6)_2 \cdot e^-$ of which structure is composed of Cs^+ ions and crown ether molecules trapping an electron at the inside of the framework [14]. Dye *et al*. discovered and developed other organic electrides, nevertheless, they cannot keep the structure up to room temperature. On the other hand, C12A7 electride is not easily oxidized at ambient atmosphere and remains stable up to about 300°C. Therefore, many industrial applications can be expected taking advantage of the noble properties.

One of the most interesting features of C12A7 electride is the outstanding low work function. The work function of C12A7 electride determined by a photoconduction measurement was ~2.5 eV [15], which is comparable to the work functions of alkali elements, despite the stability in the air. Therefore, the industrial applications such as a cold cathode, an electrode for light emitting diodes (LED) and so on, were expected taking advantage of the low work function. Electron field emission was already demonstrated by our group [16].

Further developments of the reduction process could realize fully electron doped C12A7 ($[Ca_{24}Al_{28}O_{64}]^{4+}\cdot 4e^{-}$); If the electron concentration is below 1×10^{21} cm^{-3}, the conductivity at room temperature is 0.01~100 $S\cdot cm^{-1}$ [13], and the temperature dependence (σ-*T*) shows a thermal activated behavior, which suggests the hopping conduction of the encaged electron as supported by results of terahertz time domain spectroscopy [17,18]. While, at ~1×10^{21} cm^{-3} electron concentration (critical concentration), the resistivity hardly depends on temperature, and further electron doping turns the temperature dependency to a metallic behavior [17]. The conductivity of the fully electron doped C12A7 reduced by Ti metal shows 1500 $S\cdot cm^{-1}$ at room temperature and reaches to 5000 $S\cdot cm^{-1}$ at 10 K. In addition, the carrier mobility of C12A7 electride is not exceed 0.5 $cm^2\cdot V\cdot s^{-1}$ below 1×10^{21} cm^{-3} electron concentration, but it drastically increases above the critical concentration, reaching to ~4 $cm^2\cdot V\cdot s^{-1}$ in the fully electron doped C12A7 [17]. Such the "metal-insulator transition" is one of the intriguing properties of C12A7 electride.

Theoretical calculations for the encaged electron in C12A7 electride are examined by some methods. According to the calculation with embedded cluster model, the doped electron is stabilized in the cage accompanied by lattice relaxation [18,19]. On the other hand, density function theory (DFT) calculations of the fully electron doped C12A7 suggests that the introduced electrons are delocalized and distribute to all cages equivalently [20,21]. Such the

discrepancy indicates that the phenomenon is not simple.

1.1.3. Crystal Structure and Lattice Relaxation of C12A7

The crystal structure of stoichiometric C12A7 was already investigated by X-ray diffraction (XRD) [22] and neutron diffraction [23] measurements in the past. Stoichiometric C12A7 belongs to cubic $I\bar{4}3d$ space group and the lattice constant is ~1.199 nm. A unit cell is composed of 12 cages and the two of them are randomly occupied by an extra-framework oxide ion. According to the structure model suggested by Ref. 22, all Ca atoms occupy one site placed on the S_4 symmetry axis (24*d* site). The Al atoms occupy Al1 or Al2 sites; the former site is coordinated by three bridging O atoms and one non-bridging O atom (16*c* site), and the latter site is coordinated by four equivalent bridging O atom (12*a* site). The O atoms occupy O1, O2 or O3 sites; O1 and O2 sites belong to the framework and correspond to bridging oxygen (48*e* site) and non-bridging oxygen (16*c* site), respectively. While, the O3 site corresponds to extra-framework oxygen and places on the S_4 symmetry axis (24*d* site).

If an anion is incorporated in a cage, surrounding framework atoms would be more or less deformed owing to the Coulomb interaction with the encaged anion. Especially, Ca atoms on the S_4 axis would be significantly affected by the encaged anion because of the ionic feature compared with covalent framework Al and O atoms and of the position directly facing to the cage center. The cage deformation has not been observed experimentally, however, some theoretical calculations suggest the framework deformation. According to the embedded cluster calculation, framework Ca and Al atoms are displaced to the cage center attracted by the encaged anions (Fig. 1-1(c)). The calculation estimated that encaged O^{2-} and H^- ions displace the Ca atoms to the cage center ~0.054 nm and ~0.03 nm, respectively [26, 27]. While, the calculation predicts that incorporation of a localized electron induces 0.02~0.04 nm of Ca

displacement [20]. As suggested by the theoretical calculation, the anion-induced lattice relaxation largely stabilized the total crystal energy, which would be one of reasons why C12A7 can stably encage many active anions.

1.2. Discovery and Developments of Fe-based Superconductors

1.2.1. History of Superconductors and Discovery of Fe-based Superconductivity

Figure 1-2 shows the history of representative superconductors and developments of the superconducting temperatures (T_c). Superconductivity was firstly discovered by Kamerlingh Onnes in 1911 [28], which was achieved in elemental Hg at ~4.2 K by the observation of the zero resistance. Then, he also demonstrated that many simple elements, such as Sn, Pb and so on change to superconductors below 10 K [29]. (Today, it has been confirmed that more than 30 species of simple elements show the superconductors at ambient pressure.) In addition, many intermetallic compounds, especially containing Nb, exhibit comparatively high T_c [30–33]. The T_c gradually increased with further studies of intermetallic compounds and reached to ~25 K in Nb_3Ge in 1973 [33]. Their superconductive properties and the mechanism can be explained by BCS theory proposed by Bardeen, Cooper, and Schrieffer in 1957 [34], assuming that the Cooper pairs are formed by the phonon-mediated attraction interaction. The theory predicts that the T_c would not exceed 30~40 K, and actually, the highest T_c of BCS-type superconductor is limited to ~39 K in MgB_2 discovered in 2000 so far [35]. In 1986, Bednorz and Muller suggested that La-Ba-Cu-O system exhibits the superconductivity at ~20 K [36], however, most researchers did not care the results, regarding it as minor or an experimental mistake. In November of the year, Tanaka group of Tokyo University reexamined the experimental results and confirmed that $(La,Ba)_2CuO_{4-y}$ exhibits the superconductivity by demonstrating the zero resistance and the Meissner effect [37]. Then, so-called “superconductivity fever” was occurred

and worldwide researches of Cu oxide superconductors were conducted. The T_c was drastically increased to ~93 K by the discovery of $YBa_2Cu_3O_7$ (YBCO) in the next year [38], and the highest T_c record at ambient pressure was established in $HgBa_2Ca_2Cu_3O_x$ with T_c ~130 K [39], which was further increased up to ~160 K by applying high pressure (~3 GPa) [40]. Such the drastic increase of T_c sets our expectation that room-temperature superconductivity could be achieved in near future, however, no more T_c improvements in the Cu oxide system so far have been achieved for more than 15 years. Additionally, the mechanism of high-T_c superconductivity was discussed by many theorists for a long time, however, the theory is still controversial and has not been clarified yet. It would be one of the reasons for the theoretical stagnation that new superconductors with T_c exceeding 40 K have not been discovered excepting Cu-based superconductors. Therefore, the discoveries of new high-T_c superconductors are essential for the T_c developments and the theoretical progress of high-T_c superconductivity.

In January of 2008, our group reported that F-substituted LaFeAsO exhibits the superconductivity at ~26 K [41]. This report attracted much interest of many researchers and induced the recurrence of a new superconductivity fever. Then, the T_c was immediately improved to ~55 K by the substitution of other rare-earth elements for the La site [42–44]. The Fe-based superconductors are the "second" high-T_c superconductors breaking the T_c limit of the BCS theory and the discoveries would be a breakthrough for the clarification of the mechanism and further improvements of the superconductive properties.

1.2.2. Recent Advances in Fe-based Superconductors

Figure 1-3 shows the recent representative advances of Fe-based superconductors and the T_c developments. The first Fe-based superconductivity was discovered in LaFePO with the T_c ~ 4 K by Kamihara *et al.* in 2006 [45]. Although the T_c was not so high, the discovery attracted the

interest of many researchers of superconductivity, because Fe-based compounds generally does not show the superconductivity owing to the strong magnetic behaviors of the Fe ions. In the next year, Watanabe *et al.* have found the LaNiPO is also a superconductor although the T_c did not exceed 3 K [46]. To improve the superconductive properties of the LaFePO, LaFeAsO was fabricated by replacing As with the P although the compound was already reported in the past [47]. The stoichiometric compound did not exhibit superconductivity, however, the temperature-dependent resistivity (ρ-*T*) curve shows an steep decrease at ~150 K. Kamihara substituted F atoms for the O site to dope electron carriers to the FeAs layer, then, the superconductivity was induced by more than 4% of the F substitution and the highest T_c about 26 K was observed with the ~10% F substitution [41]. The T_c was further improved to ~43 K by applying the high pressure up to ~3 GPa, while, the T_c was decreased by applying more pressure [48]. The isostructural nickel arsenide, LaNiAsO, also shows the superconductivity at 2.4 K [49], but it occurs in the stoichiometric composition and any substitution does not induce the high T_c more than 5 K, which substantially differs from the properties of LaFeAsO. After the publication of superconductivity in LaFeAsO, some Chinese groups reported that the replacement of smaller-radius rare-earth elements such as Ce, Sm, for La site of LaFeAsO:F leads high T_c more than 40 K [42,43]. The T_c was further increased to ~55 K with F-substituted NdFeAsO and SmFeAsO by the high pressure synthesis and the optimization of the F concentration [44,50,51]. It also made an impact on us that the formation of the oxygen vacancies by high pressure synthesis leads the carrier doping to FeAs layer and induces the superconductivity [52,53]. Above-mentioned *Ln*FeAsO-type (*Ln*: lanthanoids or rare-earth elements) compounds are called as 1111-type compounds due to the element ratio of the composition.

The first report of the superconductivity in transition-metal pnictides goes back to 1987:

Jeitschko *et al.* discovered the superconductivity in $LaRu_2P_2$ with the $ThCr_2Si_2$-type structure at ~4 K [26]. The $ThCr_2Si_2$-type compound has been widely studied due to the simple structure and the various compositions, and at least, more than 600 species of the compounds have been discovered. The any other superconductive "122-type" pnictides had not discovered until the $BaNi_2P_2$ was discovered by Mine *et al.* in 2008 [55]. The $BaNi_2P_2$ shows the superconductivity at ~4 K and its structure contains Ni_2P_2 layers as well as the superconductive LaNiPO. These facts implied that the Ni_2P_2 layer relates with the superconductivity. In May of 2008, Rotter *et al*. reported that K-substituted $BaFe_2As_2$ exhibits the superconductivity at ~38 K [56], which gave us two important hints for the development of Fe-based superconductors: (1) $BaFe_2As_2$ includes FeAs layers as well as *Ln*FeAsO, indicating that the FeAs layer plays the important role for the high T_c superconductivity. (2) Not only electron doping, but also hole doping is effective for the induction of the high T_c, at least $AeFe_2As_2$ (*Ae*: alkali-earth elements) system. (It is still controversial whether the hole doping is also effective or not for *Ln*FeAsO system [57].) The *Ae* site of $AeFe_2As_2$ can be replaced by Sr, Ca and Eu, and each maximum T_c is ~37 K, ~20 K, and ~34.7 K, respectively [58–60]. The isostructural 122-type iron phosphides, $AeFe_2P_2$, were also successfully synthesized in the composition of *Ae* = Ca, Sr Ba and Eu, however, they did not exhibit the superconductivity [61–63]. The 122-type FeAs compounds have been widely used for many measurements for the physical properties and the electronic structure (e.g. anisotropic electrical and magnetic measurements [64,65], neutron scattering measurements [66,67], angle-resolved photoelectron spectroscopy (ARPES) [68,69] and so on) because of the simple composition and easiness for obtaining the high-quality large single crystals.

After the discoveries of the 122-type FeAs compounds, some important Fe-based superconductors with new-type structure were discovered one after another. Wang et al. demonstrated that LiFeAs shows superconductivity at ~18 K without elemental substitution in

June of 2008 [70]. They suggested that the LiFeAs is likely to be stabilized in the Li-poor composition (i.e. $Li_{1-x}FeAs$), and the vacancies seems to induce the superconductivity, reserving carriers to the FeAs layers. The other 111-type compounds, NaFeAs and LiFeP have also been discovered, and their T_cs were reported as ~9 K and ~6 K, respectively [71,72]. In July of 2008, Hsu et al. reported that β-FeSe with α-PbO-type structure (*P*4/*nmm* space group) exhibits the superconductivity at ~8 K without elemental substitution [73]. The phase diagram of the β-FeSe indicates the β-phase stabilizes in Fe-rich composition, $Fe_{1+x}Se$ (x = 0.01~0.025) [74], which would relate to carrier doping and appearance of superconductivity as well as LiFeAs. The T_c of β-FeSe have been increased to ~37 K by applying high pressure up to 9 GPa [75,76], although further pressure changes it into hexagonal δ-FeSe phase. It is also impressed that Te substitution for the Se site enhance the T_c up to 14 K at $FeSe_{0.5}Te_{0.5}$ composition [77,78].

One of the important features of Fe-based superconductivity is that Co substitution for the Fe site induces the superconductivity. Sefat *et al.* reported that ~10% Co-substituted LaFeAsO exhibits the superconductivity at ~10 K, although it is nearly half of the maximum T_c of F-substituted one [79,80]. They also demonstrated that the Co substitution is effective to induce superconductivity in 122-compounds [81–83]. It could be explained that the Co substitution for the Fe site introduces conductive electrons to the FeAs layer due to the one more *d* electron of Co than Fe, which would induce the superconductivity. For the similar reason, it has been confirmed that the Ni substitution for the Fe site induces the superconductivity [84–86]. However, it has been so far considered that any substitutions for the superconducting layer break the superconductivity as demonstrated in Cu-based superconductors [87], in contrast to the Co-substituted Fe-based superconductors. This fact would reflect the substantial difference of superconductive properties between Fe-based and Cu-based superconductors.

At any rate, the discoveries of the Co substitution methods encourage the development of

Fe-based superconductors. In the case of CaFeAsF, which is reported by Matsuishi *et al*. as the first FeAs fluoride, the conventional F substitution could not be applicable and any other substitutions also did not accomplish successful outcomes. To induce the superconductivity, we tried ~10% Co substitution for the Fe site and achieve the superconductivity at 22 K [88]. This experience showed us that Co substitution is effective to confirm whether the parent Fe-based compounds exhibit the superconductivity or not. The first superconducting thin film was also accomplished by the Co substitution. Hiramatsu *et al.* firstly succeeded in the fabrication of epitaxial thin films of LaFeAsO and $SrFe_2As_2$ by pulse laser deposition (PLD) technique using the high-quality targets [89,90]. Nevertheless, the thin films of F-substituted LaFeAsO and K-substituted $SrFe_2As_2$ were difficult to induce the superconductivity, because the F and K atoms easily evaporate in the thin-film fabrication process in a vacuum chamber at a high temperature. On the other hand, the Co atom would be a suitable dopant for superconducting thin films due to the lower vapor pressure. Taking the advantage of the Co substitution, Hiramatsu *et al.* could succeed in the first fabrication of a superconducting thin film using $SrFe_{2-x}Co_xAs_2$ target [90]. Furthermore, they recently discovered that water vapor in the air induces the superconductivity of parent $SrFe_2As_2$ thin film [91]. Such the phenomenon would be attributed to the surface-sensitive feature of the thin films. The developments of superconducting thin films are important for the superconductive devices and the characterization of the Fe-based superconductivity, and further discoveries and applications could be expected in this field.

After the discoveries of 1111-type FeAs superconductors, above-mentioned simpler Fe-based superconductors (i.e. 122, 111 and 11 compounds) have been discovered, however, their T_cs have not exceeded the highest T_c of the 1111 compounds. To break the stagnation of the T_c developments, discovery of new FeAs superconductors were expected. Recently, $Sr_2ScFePO_3$,

a new-type Fe-based superconductor including Perovskite-like [Sr_2ScO_3] unit in the blocking layer, has been reported by Ogino *et al*. [92]. The observed T_c ~17 K is higher than that of the other superconducting iron phosphides [46,72,93] by more than 10 K. The interlayer distance of the $Sr_2ScFePO_3$ (~1.55 nm) is longer than that of *Ln*FePO (~0.9 nm), which is expected to be one of the reasons of the high T_c. The discovery rekindled the search of new Fe-based superconductors and many 21113-type FeAs superconductors, for instance, $Sr_2Sc_{1-x}Ti_xFeAsO_3$ (T_c ~7 K) [94], $Sr_2Cr_{1-x}Ti_xFeAsO_3$ (T_c ~30 K) [95], $Ca_2Sc_{1-x}Ti_xFeAsO_3$ (T_c ~37 K) [94], $Sr_2Mg_{1-x}Ti_xFeAsO_3$ (T_c ~39 K) [96], were discovered. Especially, $Sr_2VFeAsO_3$ exhibits the clear superconductivity at ~37 K without any substitution [97] and the T_c was further increased up to ~46 K by applying high pressure [98], which suggests further T_c enhancement could be expected by improvement of the constituent elements and doping methods. The other type of perovskite-related FeAs compound, $Sr_3Sc_2Fe_2As_2O_5$ (32225-compound), have been discovered by Zhu *et al.* [99], although the superconductivity have not been confirmed yet. At any rate, searching new FeAs compounds including new blocking layers is one of the hopeful solutions for the T_c developments.

1.2.3. A Variety of Crystal Structures of Fe-based Superconductors

Figure 1-4 shows the crystal structures of the reported Fe-based superconductors. All the Fe-based superconductors include Fe*Pn* (or FeSe) layers where centered Fe atom is tetrahedrally coordinated by pnictgen (*Pn* = P, As) atoms. The layer was constructed by the FePn_4 tetrahedrons shearing the edges with the other ones. If the *Pn* atoms are ignored, it can be considered each Fe atom forms a two-dimensional tetragonal Fe-plane.

The *Ln*Fe*Pn*O (1111-compound, Fig 1-4(a)) belongs to tetragonal *P*4/*nmm* space group [41,45] and can be classified into ZrCuSiAs-type compounds which is a well-studied material

group discovered more than 300 species of compounds so far [100]. The Fe*Pn* layer is separated by *Ln*O layers where centered O atom is tetrahedrally coordinated by rare-earth (*Ln*) atoms in the same manner as the Fe*Pn* layer, therefore, the two-type of layers are alternately stacked to the *c*-axis direction. Each layer is expressed in the structure formula as $[Ln^{3+}O^{2-}]$ and $[Fe^{2+}Pn^{3-}]$, and the former layer charged positively and the latter layer charged negatively considering the formal charge of each ion. The Fe*Pn* layer mostly contributes to the conductive properties because the Fermi surface is mainly composed of Fe3d orbitals, which was supported by the results of *ab initio* calculations and X-ray photoelectron spectroscopy (XPS) measurements [101–103]. On the other hand, the density of states (DOS) of *Ln* and O are placed at deep energy level below −2 eV, therefore, the *Ln*O layers act as blocking layers insulating between the conductive Fe*Pn* layers. The contrasting feature of the *Ln*O and FeAs layers enables to introduce extra electron carrier to the Fe*Pn* layer by substitution of monovalent F^- ion for the divalent O^{2-} ion in the *Ln*O layer ("indirect doping method"). The *Ln* site is occupied by lanthanoid elements from La to Tb excepting Pm and Eu [41–44,104–107], however, much smaller rare-earth element, such as Dy, Ho and Y can also be replaced by the high pressure synthesis [108–110]. In addition, $[Ae^{2+}F^-]$ layer is substitutable for the $[Ln^{3+}O^{2-}]$ layer without changing the valence state of the Fe*Pn* layer. So far, it has been reported that Ca, Sr and Eu could be occupied for the *Ae* site [88,111,112].

The $AeFe_2Pn_2$ (122-compound, Fig 1-4(b)) is belongs to tetragonal *I*4/*mmm* space group and isostructure of the $ThCr_2Si_2$-type structure which is popular and studied better than ZnCuSiAs-type compounds due to the simple composition and structure [113]. The $AeFe_2Pn_2$ also includes Fe*Pn* layer as well as *Ln*Fe*Pn*O, however, the alkali-earth elements (Ca, Sr, Ba, Eu and K [58–60,114]) are inserted between the Fe*Pn* layers on behalf of the *Ln*O blocking layers. Unlike *Ln*Fe*Pn*O, the Fe*Pn* layer of the 122-compounds faces each other to wrap the *Ae* atom

with the concave parts. Such the geometry forms the *Pn*-*Pn* homo bond between the pnictogen atoms facing each other. Especially, in the case of $CaFe_2As_2$, the phase transition to so-called "collapsed phase" occurs at low temperature due to the strong homo-bond formation [115].

The *A*Fe*Pn* (111-compound, Fig 1-4(c)) belongs to tetragonal *P*4/*nmm* as well as *Ln*Fe*Pn*O. Its structure corresponds to the *Ln*Fe*Pn*O structure from which the O site is removed. The *A* site is occupied by alkali elements such as Li and Na [71–73], and the site tends to be vacant, which seems to introduce the conductive carriers to the Fe*Pn* layer. Furthermore, if the *A* site is removed from the *A*Fe*Pn*, then it corresponds to 11-type β-FeSe structure (Fig. 1-4(d)), although the *Pn* should be replaced by the divalent chalcogen atoms (*Ch*) to keep the total valence without changing the valence of Fe. The β-FeSe is isostructure with α-PbO (tetragonal *P*4/*nmm*) and the Se site can be substituted by the other *Ch* such as S and Te. The β-FeSe is stable at very narrow range in the phase diagram; in slightly Fe-rich composition and the stable temperature range above 300°C and below 450°C [74], which indicates the delicate stability of β-FeSe.

The Ae_2MFe*Pn*O_3 (21113-compound, Fig. 1-4(e)) belongs to tetragonal *P*4/*nmm* as well as 1111-compounds, and it has the thick perovskite-like [Ae_2MO_3] layer unit between the Fe*Pn* layers although it is modified from the actual perovskite structure: The Sr of the layer inside is coordinated by seven oxygen and the *M* site is pyramidal five oxygen coordination ignoring the next nearest As atom. The *M* site can be occupied by many 3d transition elements, such as Sc, Cr, V and (Mg,Ti), while, the *Ae* site is mainly occupied by Sr atoms [92,94–96]. In the case of *M* = Sc, the Ca and Ba can also occupy the *Ae* site, however, it is expected that more 21113-type species could be synthesized by elemental replacements. Whereas, the structure of $Ae_3M_2Fe_2As_2O_5$ (32225-compound, Fig. 1-4(f)) is more similar with the perovskite structure than 21113-compounds; the blocking layer unit [$Ae_3M_2O_5$] can be regarded as a part of the

actual perovskite structure. In the case of isostructural CuS compounds, its structural formula is generalized in $[Sr_{n+1}M_nO_{3n-1}]$ $[Cu_2S_2]$ as a homologous compound; the *n* can be changed from 1 to 3 with the numbers of MO_2 planes [116]. The space group, *I*4/*mmm* is same with 122-compounds, which attributes to the Fe*Pn* layer stacked upside down alternately. The reported 32225-compound is only $Sr_3Sc_2Fe_2As_2O_5$ [99] and the superconductivity has not been reported yet. However, further development could be expected in the homologous system.

1.2.4. Comparison between Fe-based and Cu-based Superconductivity

Fe-based superconductors could be said as the "second" high-T_c superconductors which exceeded the limit of T_c (30~40 K) estimated by the BCS theory followed by Cu-based superconductors. They have some common points, for instance, including 3d metal, the layered structure, the superconductivity induced by carrier doping and so on. On the other hand, many differences can be found between them. The Main similarities and differences between Cu-based and Fe-based high-T_c superconductors are summarized in Fig. 1-5. As the structural feature, each superconductor has layered structure, and the CuO_2 plane and the FeAs layer work as the superconducting layers in each compound. In addition, their phase diagrams as a function of the carrier concentrations (Fig. 1-5) have many common features: Each parent compound is antiferromagnetic phase, and the carrier doping to the superconducting layer turns off the antiferromagnetic ordering and induces the superconductivity, which indicates that the magnetic properties of the parent phases related with their high-T_c superconductivity. In each system, further carrier doping over the optimum concentration decrease the Tc, and finally, it changes to the normal metallic phase. It is still controversial whether pseudogap phases of Fe-based superconductors are exist or not [117]. At any rate, these common features would provide insight into the mechanism of high-T_c superconductivity.

On the other hand, there are many differences between these superconductors. The valence band top of Cu oxide is consisted of Cu $3d_{x2-y2}$ orbital and O $2p$ orbital, and the strong electron-electron interaction of localized electrons on the Cu site makes it a Mott insulator in the parent phase. Such the band structure can be approximated by the single-band Hubbard model [118,119], which was supported by experimental results [120]. In contrast to the Cu oxide compounds, parent FeAs compounds show metallic behaviors, although it differs from the properties of normal metals. According to some band calculations and ARPES measurements of FeAs compounds, the band structure near the Fermi level was consist of the deeply-interacted five Fe3d orbitals, multiple electron- and hole-pockets are exist in the Fermi surface [68,102]. Theoretical studies suggest such the unique band structure contributes the strong nesting of the Fermi surface and the appearance of the high-T_c superconductivity [121,122].

In addition, one of the most interesting differences between them is the substitution effect of 3d transition metal on the superconductivity. In the case of Cu-based superconductors, the superconductivity is induced by oxygen vacancies or element substitution of the blocking layers separating the CuO_2 planes. However, the other transition-metal substitution for Cu site in the superconducting CuO_2 planes strongly suppresses the superconductivity [87]. On the other hand, the superconductivity of FeAs compounds is triggered by not only the oxygen vacancy or elemental substitution of blocking layer, but also the direct substitution of Co or Ni for the Fe in the FeAs layer. Most of FeAs superconductors could be induce the superconductivity by the Co substitution for Fe site with the wide concentration range (5~20%). In addition, Ru, the 4d transition metal with the same valence number with Fe, is also effective as a dopant for the Fe site [123]. Such the contrasting substitution effect on the superconductivity reflects the different electronic characters between them: For the Cu-based superconductors, the Cu $3d^9$ configuration hybridized with the O 2p orbitals is essential for the superconductivity in the

strongly-electron-correlated system, which leads to the sensitive character for the substitution. In contrast, the Fe-based superconductivity is attributed to the delocalized Fe 3d orbitals remotely related with the As orbitals, which would cause the insensitive character for the transition-metal substitution. These facts set our expectation that the high T_c may be achieved by using the other transition metals other than Fe.

1.2.5. Relation between Structure in FeAs Layer and Superconducting Temperature

The relation between the crystal structure of Fe-based superconductors and the superconductive property was suggested and discussed from the early stage of the study, and some papers so far evaluate the T_c based on some structural parameters. For instance, some reports arranged the T_c as a function of *a*-axis length (corresponding to √2 times the nearest Fe-Fe distance) and *c*-axis length [124], however, the most popular parameter used in many papers is As-Fe-As bond angle suggested by Lee *et al.* [125]. (There are two way to define the As-Fe-As angle, α and β angles (see the inset of Fig. 1-6(a)), nevertheless, there is a definite relation between them due to the confinement of the space group. Therefore, the α angle is adopted for the structural parameter in this paper. Furthermore, some researcher use Fe-As-Fe angle for the parameter, but it is essentially same with the As-Fe-As angle.) They demonstrated that the closer the α angle of *Ln*Fe*Pn*O becomes to the regular tetrahedron angle (109.47°), the higher the T_c become. This result suggests that the shape of FeAs tetrahedron is important for the high T_c. The tendency is likely to be applicable for the Co-substituted 1111-type fluorides as mentioned later (chapter 3).

The relation between T_c and α angle seems to be applicable to 122-type compounds. The α angles of $AeFe_2As_2$ (*Ae* = Ca, Sr, Ba, Eu), of which T_cs are higher than 20 K, are close to the regular tetrahedron angle. Especially, $Ba_{1-x}K_xFe_2As_2$ exhibit the T_c maximum with the 40% K

substitution (x = 0.4) where the α angle becomes closest to the regular tetrahedron angle [114]. In addition, it is suggested that the structural changes induced by high pressure is related with the superconductive property: Kimber *et al*. demonstrated that the structural changes of lattice constants and α angle in $BaFe_2As_2$ induced by high pressure are very resemble to that induced by the K substitution [126]. From these facts, they suggested that the chemical pressure induced by the substitution is more critical for the T_c increase than that of carrier doping. This suggestion is very interesting although further investigations and verifications are needed to conclude.

The empirical "regular tetrahedron rule" has been admitted by many researchers, however, how the FeAs tetrahedron shape affects on the superconductive properties has not elaborated from theoretical viewpoints yet. Assuming that the density of states (DOS) on the Fermi surface increases with the increase of the symmetry around Fe atom due to the degeneration of the Fe3d orbitals, the FeAs tetrahedron shape would be important for the superconductive properties. However, any theoretical papers discussed from the viewpoint have not been published yet to my best knowledge. Recently, Kuroki et al proposed new hypothesis which explains the relation between crystal structure and the T_c from the theoretical viewpoint [122]. They focused on the height of the pnictogen from the Fe plane (h_{Pn}) and calculated the difference of the electronic structure by changing the h_{Pn} as a parameter, considering all the five Fe3d orbitals in the calculation. According to the results, appearance of the Fermi surface around (π, π), which is very sensitive to the parameter h_{Pn}, leads to the nesting effect, affecting the T_c and symmetry of the superconducting gap. They concluded that the T_c increases with increase of the h_{Pn}.

To examine the above-mentioned two hypotheses, the T_cs of reported Fe-based superconductor are plotted as a function of α angle and h_{Pn} in the Fig. 1-6(a) and (b), respectively. For comparison, the selected T_c values are the highest one of each superconductor, and the α or h_{Pn} were those of the parent compounds at room temperature and ambient pressure.

Note that plotted values more or less include errors because the T_c depends on how to take the value from measured data, and the refined structure also depends on the dopant species and concentration, the measured temperature, the sample quality and so on.

In the case of the T_c-α plot (Fig. 1-6(a)), higher T_cs tend to concentrate on around the regular tetrahedron angle (109.47°), which is consistent with the "regular tetrahedron rule". Whereas, some T_cs are not so high even though their bond angles are close to the regular tetrahedron angle: As for the 1111, 122 and 21113-type compounds, the most cases are applicable to the empirical rule, while, the plots of 111-type compounds deviate from the rule. The angles of NaFeAs [71] and LiFeP [72] are close to the regular tetrahedron (~108.5°), however, the T_cs are not so high (~9 K for NaFeAs, ~6 K for LiFeP). Whereas, LiFeAs exhibit higher T_c (~18 K) than the other 111-type compounds although its α angle (~103°) is deviate from the regular tetrahedron angle [127]. The FeAs tetrahedron shape of LiFeAs is elongated to c-axis direction, which is same in the 11-type FeSe compounds. It should be reconsidered the "regular tetrahedron rule" including such the cases because the elongated FeAs tetrahedron shapes are rare in the 1111 and 122-type compounds.

Whereas, according to the T_c-h_{Pn} plot (Fig. 1-6(b)), it seems that the higher *Pn* position does not necessarily leads to the higher T_c if all the compounds were considered. However, this tendency could be applicable in each structure-type system, and the above-mentioned contradiction of 111-type compounds in the "regular tetrahedron rule" is resolved in this plot. Nevertheless, some contradiction could be pointed, for example, KFe_2As_2 exhibit lowest T_c (~4 K) even though it has the highest As position in the superconductive FeAs 122-compounds [128]. For the 11-type FeSe compounds, the T_c was improved up to 14 K by ~50% of Te substitution for the Se site, however, the further substitution decreases the T_c. According to the theory, the T_c is expected to be improved by the further Te substitution because of increase of

the height, nevertheless, the actual results have not shown that. It may suggest that there is a limit to expect the T_c from FeAs structure without consideration of electronic structure or the other factors.

As mentioned above, the structural parameter which can explain all the T_cs of Fe-based superconductors without contradiction has not been discovered yet, nevertheless, the structure of FeAs layer seems to be somehow related with the T_c. It is expected that the relation would be clarified by further investigation and it would contributes to the T_c improvement and clarification of mechanism.

1.3. Objective of the Present Study

I have reviewed the backgrounds of C12A7 and Fe-based superconductors in above sections**.** They exhibit many curious and distinctive properties relevant to the crystal structure. To clarify the detailed structure and the relation with the physical properties would be useful to gain deeper insight into them for performance improvements and new material searches. In this study, the crystal structure of anion-encaged C12A7 and Fe-based superconductors were examined, and the relations with their unique properties are discussed from the viewpoint of crystal chemistry, assisted by *ab initio* calculations.

For C12A7, incorporation of various anions induce the many interesting properties, however, the detailed behaviors of encaged anions and the cage deformation have not been experimentally demonstrated yet. To examine the information would be important to understand the properties of C12A7, therefore, the detailed structures of anion incorporated C12A7 are investigated by MEM/Rietveld. In addition, the C12A7 electride is one of the hottest topics due to the noble and curious properties. Recent improvements in reduction process have enabled to fabricate the fully electron doped C12A7 ($[Ca_{24}Al_{28}O_{64}]^{4+}\cdot 4e^-$). In this study, the crystal

structure of the C12A7 electride was also examined and the origin of the metal-insulator transition was discussed.

As for the Fe-base superconductors, the properties of the high-T_c superconductivity have attracted many researchers' attentions, while it was also intriguing that that parent LaFeAsO exhibits "anomalies" in the resistivity and the magnetic susceptibility at ~160 K. The first objective of this study is to clarify the cause of the anomalies by the crystal structure analysis and theoretical calculation of LaFeAsO at low temperature. Secondly, the progress of T_c has stagnated after the improvement of T_c up to ~55 K with F-substituted SmFeAsO as seen in Fig. 1-3. To break the stagnation and to achieve further progress, improvements and considering the crystal and electronic structures would be needed. Especially, the crystal structure is likely to relate to the T_c as mentioned in the last section. The second objective is to investigate and verify the relation between the crystal structure and the superconductive property of Fe-based superconductors. In addition, searching new iron arsenides is one of the breakthroughs to progress in the Fe-based superconductivity. The third objective of this study is to discover a new iron arsenide with new structure and to induce the superconductivity by carrier doping.

1.4. Outline of This Study

Chapter 2: Effects of O^{2-}, OH^- and H^- ion incorporation on the cage geometry in C12A7 crystals ware examined by the maximum entropy method (MEM)/Rietveld analyses of synchrotron powder X-ray diffraction data. It was experimentally demonstrated that the presence of an extra-framework anion in a cage causes inward displacements of two Ca^{2+} ions axially coordinating to the anion. In addition, it was clarified that positions of the encaged anions and the manners of the cage deformation vary with the species of the encaged anion, which would relate with the property and stability of C12A7.

Chapter 3: The fully electron-doped C12A7 electride was fabricated by Ti treatment and the crystal structure was examined by the MEM/Rietveld analysis to discuss the relation with the metal-insulator transition. The electron density map obtained by the MEM/Rietveld analysis indicated the cage deformation does not occur in the prepared sample and the doped electrons are delocalized and distribute each cage equivalently. Little electron density inner the cage also supports the extra-framework oxide ions are almost perfectly extracted by the reduction process. The origin of the metal-insulator transition with a sharp mobility increase is discussed.

Chapter 4: The crystal structures of the parent (unsubsituted) and 14% F-substituted LaFeAsO at low temperature were investigated. It was demonstrated that parent LaFeAsO exhibits the crystallographic phase transition from tetragonal (*P*4/*nmm*) to orthorhombic (*Cmma*) at around ~150 K where the steep decrease of the resistivity is observed in the ρ-*T* curve. On the other hand, the superconductive F-substituted LaFeAsO did not exhibit the phase transition down to 30 K, suggesting the transition was suppressed by carrier doping. The effects of the tetragonal to orthorhombic phase transition on the magnetic properties of parent LaFeAsO were also examined by *ab initio* calculation.

Chapter 5: The effects of substitution for Fe site and the other site on the crystal structure of LaFeAsO were examined by Rietveld and MEM analysis of Co- and F-substituted LaFeAsO. The Co substitution for Fe site (direct doping) only induces the structural change in FeAs layer without the structural change in the LaO layer. On the other hand, F substitution (indirect doping) induces not only the structural change in FeAs layer, but also local structure changes around the substituted F ion and the decrease in interlayer distance betweem FeAs and LaO layer. The relation between the T_c and the above structure changes was also discussed.

Chapter 6: The superconductive properties of newly found superconductors, AeFe$_{1-x}$Co$_x$AsF (Ae = Ca or Sr and x = 0, 0.06, 0.12) were discussed from the viewpoint of the crystal structure. The refined structures reveal that deference of the $FeAs_4$ tetrahedron shape between CaFeAsF and SrFeAsF are originated from structural mismatches between FeAs and AeF layer. In the SrFeAsF, the $FeAs_4$ tetrahedron shape is flattened along a–b plane by the horizontal tension caused by the larger Sr_4F tetrahedron. On the other hand, $FeAs_4$ tetrahedron shape in the CaFeAsF is close to the regular one, because the mismatch between the $FeAs_4$ and Ca_4F tetrahedrons is comparatively small. Co substitution further removes the distortion in the CaFeAsF contrast to the SrFeAsF. The discussion of the relation between As-Fe-As bond angle and T_c were suggested to enhance the T_c.

Chapter 7: A new structure-type iron arsenide, $Sr_2CrFe_2As_2O_2$ was successfully fabricated by preparing the starting composition with the ~10% O-poor one. The estimated valence of Cr from the bond-valence sum and the *ab initio* calculation was nearly divalent, which differs from 32225 and 21113-type compounds containing trivalent 3d elements in the blocking layer. The Cr^{2+} ion would lead $3d^4$ configuration with high spin state due to the square-planar O coordination. Considering the temperature-dependent magnetic susceptibility and the calculation results, the magnetic moments of Cr seem to order antiferromagnetically in the CrO_2 plane. Although “anomalies” as observed in the other FeAs superconductor have not been observed yet, it is expected to be the parent compound of high-T_c superconductors by further improvement of the constituent elements or doping methods.

Chapter 8: Finally, the summary of this study is described along with future’s issues.

References

[1] H. Hosono, Y. Abe, Inorg. Chem. **26**, 1192 (1987).

[2] M. Lacerda, J. T. S. Irvine, F. P. Glasser, A. R.West, Nature **332**, 525 (1988).

[3] R. W. Nurse, J. H. Welch, A. J. Majumdar, Trans. Br. Ceram. Soc. **64**, 323 (1965).

[4] K. Hayashi, M. Hirano, H. Hosono, J. Phys. Chem. B **109**, 11900 (2005).

[5] K. Hayashi, S. Matsuishi, M. Hirano, H. Hosono, J. Phys. Chem. Soc. B **108**, 8920 (2004).

[6] K. Hayashi, M. Hirano, S. Matsuishi, H. Hosono, J. Am. Chem. Soc. **124**, 738 (2002).

[7] J. Jeevaratnam, F. P. Glasser, L. S. D. Glasser, J. Am. Ceram. Soc. **47**, 105 (1964).

[8] P. P. Williams, Acta. Crystallogr. B **29**, 1550 (1973).

[9] Q. L. Feng, F. P. Glasser, R. Alan-Howie,. E. E. Lachowski, Acta. Crystallogr. C **44**, 589 (1988).

[10] K. Hayashi, S. Matsuishi, T. Kamiya, M. Hirano, H. Hosono, Nature **419**, 462 (2002).

[11] M. Miyakawa, H. Kamioka, M. Hirano, T. Kamiya, P. V. Sushko, A. L. Shluger, N. Matsunami, H. Hosono, Phys. Rev. B **73**, 205108 (2006)

[12] Q. X. Li, K. Hayashi, M. Nishioka, H. Kshiwagi, M. Hirano, Y. Torimoto, H. Hosono, M. Sadakata, Appl. Phys. Lett. **80**, 4259 (2002).

[13] S. Matsuishi, Y. Toda, M. Miyakawa, K. Hayashi, T. Kamiya, M. Hirano, I. Tanaka, H. Hosono, Science **301**, 626 (2003).

[14] J. L. Dye, Science **247**, 663 (1990).

[15] Y. Toda, H. Yanag, E. Ikenaga, J. J. Kim, M. Kobat, S. Ueda, T. Kamiya, M. Hirano, K. Kobayashi, H. Hosono, Adv. Mater. **19**, 3564 (2007).

[16] Y. Toda, S. Matsuishi, K. Hayashi, K. Ueda, T. Kamiya, M. Hirano, H. Hosono, Adv. Mater. **16**, 685 (2004).

[17] H. Harimochi, J. Kitagawa, M. Ishizaka, M. Kadoya, M. Yamanishi, S. Matsuishi, H. Hosono, Phys.Rev. B **70**, 193104 (2004).

[18] J. Kitagawa, M. Ishizaka, Y. Kadoya, S. Matsuishi, H. Hosono, J. Phys.Soc. Jpn. **75**, 084715 (2006).

[19] S. W. Kim, S. Matsuishi, T. Nomura, Y. Kubota, M. Takata, K. Hayashi, T. Kamiya, M. Hirano and H. Hosono, Nano Lett. **7**, 1138 (2007).

[20] P. V. Sushko, A. L. Shluger, K. Hayashi, M. Hirano, H. Hosono, Phys. Rev. Lett. **91**, 126401 (2003).

[21] P. V. Sushko, A. L. Shluger, K. Hayashi, M. Hirano, H. Hosono, Mater. Sci. Eng. C **25**, 722 (2005).

[22] Z. Li, J. Yang, J. G. Hou, Q. Zhu, Angwe. Chem. **116**, 6641 (2004).

[23] J. E. Medvedeva, A. J. Freeman, Appl. Phys. Lett. **85**, 955 (2004).

[24] H. Bartl, T. Scheller, Neues Jahrb. Mineral. Monatshefte **35**, 547 (1970).

[25] A. N. Cristensen, Acta Chem. Scand. A **41**, 110 (1987).
[26] P. V. Sushko, A. L. Shluger, Appl. Phys. Lett. **86**, 092101 (2005).
[27] P. V. Sushko, A. L. Shluger, Phys. Rev. B **73**, 14101 (2006).
[28] H. Kamerlingh Onnes, Akademie van Wetenschappen (Amsterdam) **14**, 113 (1911).
[29] H. Kamerlingh Onnes, Akademie van Wetenschappen (Amsterdam) **16**, 673 (1913).
[30] W. Meissner and H. Fraxz, Zeitschrift für Physik **65**, 30 (1930).
[31] G.. Aschermann, E. Frmdrich, E. Justi and J. Krame, Physikalische Zeitschrift **42**, 349 (1941).
[32] B. T. Matthias, T. H. Geballe, S. Geller, and E. Corenzwit, Phys. Rev. **95**, 1435 (1954).
[33] J. R. Gavaler, Appl. Phys. Lett. **23**, 480 (1973).
[34] J. Bardeen, L. Cooper and J. R. Schrieffer, Phys. Rev. **108**, 1175 (1957).
[35] J. Nagamatsu, N. Nakagawa, T. Muranaka, Y. Zenitani and J. Akimitsu, Nature **410**, 63 (2001).
[36] J. G. Bednorz and K. A. Müller, Zeitschrift für Physik B: Condensed matter **64**, 189 (1986).
[37] H. Takagi, S. Uchida, K. Kitazawa and S. Tanaka, Jpn. J. Appl. Phys. **26**, L123 (1987).
[38] M. K. Wu, J. R. Ashburn, C. J. Torng, P. H. Hor, R. L. Meng, L. Gao, Z. J. Huang, Y. Q. Wang and C. W. Chu, Phys. Rev. Lett. **58**, 908 (1987).
[39] A. Schilling M. Cantoni J. D. Guo and H. R. Ott, Nature **363**, 56 (1993).
[40] L. Gao, Y. Y. Xue, F. Chen, Q. Xiong, R. L. Meng, D. Ramirez and C. W. Chu, Phys. Rev. B **50**, 4260 (1994).
[41] Y. Kamihara, T. Watanabe, M. Hirano and H. Hosono, J. Am. Chem. Soc. **130**, 3296 (2008).
[42] G. F. Chen, Z. Li, D. Wu, G. Li, W. Z. Hu, J. Dong, P. Zheng, J. L. Luo and N. L. Wang Phys. Rev. Lett. **100**, 247002 (2008).
[43] X. H. Chen, T. Wu, G. Wu, R. H. Liu, H. Chen and D. F. Fang, Nature **453**, 761 (2008).
[44] Z. A. Ren, W. Lu, J. Yang, W. Yi, X. L. Shen, Z. C. Li, G. C. Che, X. L. Dong, L. L. Sun, F. Zhou and Z. X. Zhao, Chin. Phys. Lett. **25**, 2215 (2008).
[45] Y. Kamihara, M. Hirano, H. Yanagi, T. Kamiya, Y. Saitoh, E. Ikenaga, K. Kobayashi and H. Hosono, Phys. Rev. B **77**, 214515 (2008).
[46] T. Watanabe, H. Yanagi, T. Kamiya, Y. Kamihara, H. Hiramatsu, M. Hirano and H. Hosono, Inorg. Chem. **46**, 7719 (2007).
[47] B. I. Zimmer, W. Jeitschko, J. H. Albering, R. Glaum and M. Reehuis, J. Alloys Compounds **229**, 238 (1995).
[48] H. Takahashi, K. Igawa, K. Arii, Y. Kamihara, M. Hirano and H. Hosono, Nature **453**, 376 (2008).

[49] T. Watanabe, H. Yanagi, Y. Kamihara, T. Kamiya, M. Hirano, H. Hosono, J. Sol. State Chem. **181** 2117 (2008).

[50] R. H. Liu, G. Wu, T. Wu, D. F. Fang, H. Chen, S. Y. Li, K. Liu, Y. L. Xie, X. F. Wang, R. L. Yang, L. Ding, C. He, D. L. Feng, and X. H. Chen, Phys. Rev. Lett. **101**, 087001 (2008).

[51] Z. A. Ren, J. Yang, W. Lu, W. Yi, X. L. Shen, Z. C. Li, G. C. Che, X. L. Dong, L. L. Sun, F. Zhou and Z. X. Zhao, Europhys. Lett. **82**, 57002 (2008).

[52] Z. A. Ren, G. C. Che, X. L. Dong, J. Yang, W. Lu, W. Yi, X. L. Shen, Z. C. Li, L. L. Sun, F. Zhou and Z. X. Zhao, Europys. Lett. **83**, 17002 (2008).

[53] H. Kito, H. Eisaki and A. Iyo, J. Phys. Soc. Jpn. **77**, 063707 (2008).

[54] W. Jeitschko, R. Glaum and L. Boonk, J. Solid State Chem. **69**, 93 (1978).

[55] T. Mine, H. Yanagi, T. Kamiya, Y. Kamihara, M. Hirano and H. Hosono, Solid State Commun. **147** 111 (2008).

[56] M. Rotter, M. Tegel and D. Johrendt, Phys. Rev. Lett. **101**, 107006 (2008).

[57] X. Zhu, F. Han, P. Cheng, G. Mu, B. Shen, L. Fang and H. H. Wen; Europhys. Lett. **85**, 17011 (2009).

[58] G. F. Chen, Z. Li, G. Li, W. Z. Hu, J. Dong, X. D. Zhang, P. Zheng, N. L. Wang, J. L. Luo, Chen, Chin. Phys. Lett., **25**, 3403 (2008)

[59] G. Wu, H. Chen, T. Wu, Y. L. Xie, Y. J. Yan, R. H. Liu, X. F. Wang, J. J. Ying and X. H. Chen, J. Phys.: Condens. Matter **20**, 422201 (2008).

[60] Y. P. Qi, Z. S. Gao, L. Wang, D. L. Wang, X. P. Zhang, and Y. W. Ma, New J. Phys. **10**, 123003 (2008).

[61] A. Mewis, Z. Naturforsch. **35b**, 141 (1980).

[62] M. Reehuis, J. Phys. Chem. Solids, **51**, 961 (1990).

[63] E. Gustenau, P. Herzig and A. Neckel, J. Alloys Compd. **262**, 516 (1997).

[64] N. Ni, S. L. Bud'ko, A. Kreyssig,, S. Nandi, G. E. Rustan, A. I. Goldman, S. Gupta, J. D. Corbett, A. Kracher and P. C. Canfield, Phys. Rev. B **78**, 014507 (2008).

[65] J. Q. Yan, A. Kreyssig, S. Nandi, N. Ni, S. L. Bud'ko, A. Kracher, R. J. McQueeney, R. W. McCallum, T. A. Lograsso, A. I. Goldman and P. C. Canfield Phys. Rev. B **78**, 024516 (2008).

[66] R. A. Ewings, T. G. Perring, R. I. Bewley, T. Guidi, M. J. Pitcher, D. R. Parker, S. J. Clarke and A. T. Boothroyd, Phys. Rev. B **78**, 220501(R) (2008).

[67] J. Zhao, D. T. Adroja, D. X. Yao, R. Bewley, S. Li, X. F. Wang, G. Wu, X. H. Chen, J. Hu and P. Dai, Nature Phys. **5**, 555 (2009).

[68] K. Nakayama, T. Sato, P. Richard, Y. M. Xu, Y. Sekiba, S. Souma, G. F. Chen, J. L. Luo, N. L. Wang, H. Ding and T. Takahashi, Europhys. Lett. **85**, 67002 (2009).

[69] H. Ding, P. Richard, K. Nakayama, K. Sugawara, T. Arakane, Y. Sekiba, A. Takayama, S. Souma, T. Sato, T. Takahashi, Z. Wang, X. Dai, Z. Fang, G. F. Chen, J. L. Luo and N. L. Wang, Europhys. Lett. **83**, 47001 (2008).

[70] X. C. Wang, Q. Q. Liu, Y. X. Lv, W. B. Gao, L. X. Yang, R. C. Yu, F. Y. Li and C. Q. Jin, Solid State Commun. **128** 538 (2008).

[71] D. R. Parker, M. J. Pitcher, P. J. Baker, I. Franke, T. Lancaster, S. J. Blundell and S. J. Clarke, Chem. Commun. 2189 (2009).

[72] Z. Deng, X. C. Wang, Q. Q. Liu, S. J. Zhang, Y. X. Lv, J. L. Zhu, R. C. Yu, C. Q. Jin, Europhys. Lett. **87**, 3704 (2009).

[73] F. C. Hsu, J. Y. Luo, K. W. Yeh, T. K. Chen, T. W. Huang, P. M. Wu, Y. C. Lee, Y. L. Huang, Y. Y. Chu, D. C. Yan and M. K. Wu, Proc. Natl. Acad. Sci. USA **105**, 14262 (2008).

[74] T. M. McQueen, Q. Huang, V. Ksenofontov, C. Felser, Q. Xu, H. Zandbergen, Y. S. Hor, J. Allred, A. J. Williams, D. Qu, J. Checkelsky, N. P. Ong, and R. J. Cava Phys. Rev. B **79**, 014522 (2009).

[75] Y. Mizuguchi, F. Tomioka, S. Tsuda, T. Yamaguchi and Y. Takano, Appl. Phys. Lett. **93**, 152505 (2008).

[76] S. Medvedev, T.M. McQueen, I. Trojan, T. Palasyuk, M.I. Eremets, R. J. Cava, S. Naghavi, F. Casper, V. Ksenofontov, G. Wortmann and C. Felser, Nature Mater. **8**, 630 (2009).

[77] M. H. Fang, H. M. Pham, B. Qian, T. J. Liu, E. K. Vehstedt, Y. Liu, L. Spinu, and Z. Q. Mao, Phys. Rev. B **78**, 224503 (2008)

[78] K. W. Yeh, T. W. Huang, Y. L. Huang, T. K. Chen, F. C. Hsu, P. M. Wu, Y. C. Lee, Y. Y. Chu, C. L. Chen, J. Y. Luo, D. C. Yan and M. K. Wu, Europhys. Lett. 84, 37002 (2008).

[79] A. S. Sefat, A. Huq, M. A. McGuire, R. Jin, B. C. Sales, D. Mandrus, L. M. D. Cranswick, P. W. Stephens and K. H. Stone, Phys. Rev. B **78**, 104505 (2008).

[80] C. Wang, Y. K. Li, Z. W. Zhu, S. Jiang, X. Lin, Y. K. Luo, S. Chi, L. J. Li, Z. Ren, M. He, H. Chen, Y. T. Wang, Q. Tao, G. H. Cao, and Z. A. Xu, Phys. Rev. B **79**, 054521 (2009).

[81] A. S. Sefat, R. Jin, M. A. McGuire, B. C. Sales, D. J. Singh, D. Mandrus, Phys. Rev. Lett. **101**, 117004 (2008).

[82] A. Leithe-Jasper, W. Schnelle, C. Geibel, and H. Rosner, Phys. Rev. Lett. **101**, 207004 (2008).

[83] G. F. Chen, Z. Li , G. Li, W. Z. Hu, J. Dong, J. Zhou, X. D. Zhang, P. Zheng, N. L. Wang and J. L. Luo, Chin. Phys. Lett. **25**, 3403 (2008).

[84] G. G. Cao, S. Jiang, X. Lin, C. Wang, Y. Li, Z. Ren, Q. Tao, C. Feng, J. Dai, Z. Xu and F. C. Zhang, Phys. Rev. B **79**, 174505 (2009).

[85] Y. K. Li, X. Lin, T. Zhou, J. Q. Shen, Q. Tao, G. H. Cao and Z. A. Xu, J. Phys.: Condens. Matter **21**, 355702 (2009).

[86] L. J. Li, Y. K. Luo, Q. B. Wang, H. Chen, Z. Ren, Q. Tao, Y. K. Li, X. Lin, M. He, Z. W. Zhu, G. H. Cao and Z. A. Xu, New J. Phys. **11**, 025008 (2009).

[87] J. M. Tarascon, L. H. Greene, P. Barboux, W. R. McKinnon, G. W. Hull, T. P. Orlando, K. A. Delin, S. Foner and E. J. McNiff, Phys. Rev. B **36**, 8393 (1987).

[88] S. Matsuishi, Y. Inoue, T. Nomura, H. Yanagi, M. Hirano and H. Hosono, J. Am. Chem. Soc. **130**, 14428 (2008).

[89] H. Hiramatsu, T. Katase, T. Kamiya, M. Hirano and H. Hosono, Appl. Phys. Lett. 93, 162504 (2008).

[90] H. Hiramatsu, T. Katase, T. Kamiya, M. Hirano and H. Hosono, Appl. Phys. Express, **1** 101702 (2008).

[91] H. Hiramatsu, T. Katase, T. Kamiya, M. Hirano, H. Hosono. Phys. Rev. B **80**, 052501 (2009).

[92] H. Ogino, Y. Matsumura, Y. Katsura, K. Ushiyama, S. Horii, K. Kishio, J. Shimoyama, Supercond. Sci. Technol. **22**, 075008 (2009).

[93] Y. Kamihara, H. Hiramatsu, M. Hirano, Y. Kobayashi, S. Kitao S. Higashitaniguchi, Y. Yoda, M. Seto and H. Hosono, Phys. Rev. B **78**, 184512 (2008).

[94] G. F. Chen, T. L. Xia, H. X. Yang, J. Q. Li, P. Zheng, J. L. Luo, N. L. Wang, Supercond. Sci. Tech. **22**, 072001 (2009).

[95] X. Zhu, F. Han, G. Mu, P. Cheng, B. Shen, B. Zeng, H. H. Wen, Sci. China Ser. G **52**, 1876 (2009).

[96] S. Sato, H. Ogino, N. Kawaguchi, Y. Katsura, K. Kishio and J. Shimoyama, arXiv:0912.1840.

[97] X. Zhu, F. Han, G. Mu, P. Cheng, B. Shen, B. Zeng, and H. H. Wen, Phys. Rev. B **79**, 220512 (2009).

[98] H. Kotegawa, T. Kawazoe, H. Tou, K. Murata, H. Ogino, K. Kishio, J. Shimoyama, arXiv:0908.1469.

[99] X. Zhu, F. Han, G. Mu, B. Zeng, P. Cheng, B. Shen, and H. H. Wen, Phys. Rev. B **79**, 024516 (2009).

[100] R. Pottgen, D. Johrendt, Z. Naturforsch. **63b**, 1135 (2008).

[101] D. J. Singh and M. H. Du, Phys. Rev. Lett. **100**, 237003 (2008).

[102] T. Sato, S. Souma, K. Nakayama, K. Terashima, K. Sugawara, T. Takahashi, Y. Kamihara, M. Hirano and H. Hosono, J. Phys. Soc. Jpn. **77**, 063708 (2008).

[103] D. H. Lu, M. Yi, S. K. Mo, A. S. Erickson, J. Analytis, J. H. Chu, D. J. Singh, Z. Hussain, T. H. Geballe, I. R. Fisher and Z. X. Shen, Nature **455**, 81 (2008).

[104] Z. A. Ren, J. Yang, W. Lu, W. Yi, G. C. Che, X. L. Dong, L. L. Sun and Z. X. Zhao, Mater. Res. Innov. 12, 105 (2008).

[105] Z. A. Ren, J. Yang, W. Lu, W. Yi, X. L. Shen, Z. C. Li, G. C. Che, X. L. Dong, L. L. Sun, F. Zhou and Z. X. Zhao; Europhys. Lett. **82**, 57002 (2008).

[106] G. F. Chen, Z. Li, D. Wu, J. Dong, G. Li, W. Z. Hu, P. Zheng, J. L. Luo and N. L. Wang, Chin. Phys. Lett. **25**, 2235 (2008).

[107] L. J. Li, Y. K. Li, Z. Ren, Y. K. Luo, X. Lin, M. He, Q. Tao, Z. W. Zhu, G. H. Cao and Z. A. Xu, Phys. Rev. B **78**, 132506 (2008).

[108] K. Miyazawa, K. Kihou, P. M. Shirage, C. H Lee, H. Kito, H. Eisaki, and A. Iyo, J. Phys. Soc. Jpn. **78** 034712 (2009).

[109] J. Yang, X. L. Shen, W. Lu, W. Yi, Z. C. Li, Z. A. Ren, G. C. Che, X. L. Dong, L. L. Sun, F. Zhou and Z. X. Zhao, New J. Phys. **11**, 025005 (2009).

[110] S. V. Chong, T. Mochiji and K. Kadowaki, J. Phys.: Conf. Ser. **150**, 052036 (2009).

[111] S. Matsuishi, Y. Inoue, T. Nomura, M. Hirano and H. Hosono, J. Phys. Soc. Jpn. **77**, 113709 (2008).

[112] X. Zhu, F. Han, P. Cheng, G. Mu, B. Shen, B. Zeng and H. H. Wen, Physica C **469**, 381 (2009).

[113] G. Just and P. Paufler, J. Alloys Compd. **232**, 1 (1996).

[114] M. Rotter, M. Pangerl, M. Tegel and D. Johrendt, Angew. Chem. Int. Ed. **47**, 7949 (2008).

[115] A. Kreyssig, M. A. Green, Y. Lee, G. D. Samolyuk, P. Zajdel, J. W. Lynn, S. L. Bud'ko, M. S. Torikachvili, N. Ni, S. Nandi, J. B. Leão, S. J. Poulton, D. N. Argyriou, B. N. Harmon, R. J. McQueeney, P. C. Canfield, and A. I. Goldman, Phys. Rev. B **78**, 184517 (2008).

[116] K. Otzschi, H. Ogino, J. Shimoyama and K. Kishio, J. Low Temp. Phys. **117**, 729 (1999).

[117] Y. Ishida, T. Shimojima, K. Ishizaka, T. Kiss, M. Okawa, T. Togashi, S. Watanabe, X. Y. Wang, C. T. Chen, Y. Kamihara, M. Hirano, H. Hosono and S. Shin, Phys. Rev. B **79**, 060503(R) (2009).

[118] F. C. Zhang and T. M. Rice, Phys. Rev. B **37**, 3759 (1988).

[119] H. Matsukawa and H.Fukuyama, J. Phys. Soc. Jpn. **58**, 2845, (1989).

[120] C. Kendziora, D. Mandrus, L. Mihaly and L. Forro; Phys. Rev. B **46**, 14297 (1992).

[121] I. I. Mazin, D. J. Singh, M. D. Johannes and M. H. Du, Phys. Rev. Lett. **101**, 057003 (2008).

[122] K. Kuroki, H. Usui, S. Onari, R. Arita and H. Aoki, Phys. Rev. B **79**, 224511 (2009).

[123] Y. Qi, L. Wang, Z. Gao, D. Wang, X. Zhang and Y. Ma, Physica C **469**, 1921 (2009).

[124] T. Ito, A. Iyo, H. Eisaki, H. Kito, K. Kihou, R. Kumai, N. Takeshita, Y. Tomioka, H. Matsuhata, C. H. Lee, K. Miyazawa, C. H. Lee, P. M. Shirage and M. Ishikado, Kotai Butsuri (written in Japanese) **43**,651 (2009).

[125] C. H. Lee, A. Iyo, H. Eisaki, H. Kito, M. T. Fernandez-Diaz, T. Ito, K. Kihou, H. Matsuhata, M. Braden and K. Yamada; J. Phys. Soc. Jpn. **77**, 083704 (2008).

[126] S. A. J. Kimber, A. Kreyssig, Y. Z. Zhang, H. O. Jeschke, R. Valentí, F. Yokaichiya, E. Colombier, J. Yan, T. C. Hansen, T Chatterji, R. J. McQueeney, P. C. Canfield, A. I. Goldman and D. N. Argyriou, Nature Mater. **8**, 471 (2009).

[127] J. H. Tapp, Z. Tang, B. Lv, K. Sasmal, B. Lorenz, P. C. W. Chu and A. M. Guloy; Phys. Rev. B **78**, 060505 (2008).

[128] S. Rozsa and H. U. Schuster; Z. Naturforsch. **36b**, 1668 (1981).

[129] K. Horigane H. Hiraka and K. Ohoyama, J. Phys. Soc. Jpn. **78**, 074718 (2009).

[130] C. Wang, L. Li, S. Chi, Z. Zhu, Z. Ren, Y. Li, Y. Wang, X. Lin, Y. Luo, S. Jiang, X. Xu, G. Cao and Z. Xu, Europhys. Lett. **83**, 67006 (2008).

[131] J. Zhao, Q. Huang, C. de la Cruz, S. Li, J. W. Lynn, Y. Chen, M. A. Green, G. F. Chen,. G. Li, Z. Li, J. L. Luo, N. L. Wang and P. Dai, Nature Mater. **7**, 953 (2008).

[132] J. Zhao, Q. Huang, C. de la Cruz, J. W. Lynn, M. D. Lumsden, Z. A. Ren, J. Yang, X. Shen, X. Dong, Z. Zhao and P. Dai, Phys. Rev. B **78**, 132504 (2008).

[133] X. Wang, S. R. Ghorbani, G. Peleckis, S. Dou, Adv. Mater. **21**, 236 (2009).

[134] A. Martinelli, A. Palenzona, C. Ferdeghini, M. Putti, and H. Emerich, J. Alloys Compd. **477**, L21 (2009).

[135] J. W. G. Bos, G. B. S. Penny, J. A. Rodgers, D. A. Sokolov, A. D. Huxley, and J. P. Attfield, Chem. Commun. 3634 (2008).

[136] F. Ronning, N. Kurita, E. D. Bauer, B. L. Scott, T. Park, T. Klimczuk, R. Movshovich, and J. D. Thompson, J. Phys.: Condens. Matter **20**, 342203 (2008).

[137] M. Tegel, M. Rotter, V. Weiss, F. M. Schappacher, R. Pöttgen and D. Johrendt, J. Phys.: Condens. Matter **20**, 452201 (2008).

[138] M. Rotter, M. Tegel, D. Johrendt, I. Schellenberg, W. Hermes, and R. Pöttgen, Phys. Rev. B **78**, 020503(R) (2008).

[139] M. J. Pitcher, D. R. Parker, P. Adamson, S. J. Herkelrath, A. T. Boothroyd, R. M. Ibberson, M. Brunelli, S. J. Clarke, Chem. Commun. 5918 (2008).

[140] M. Tegel, F. Hummel, S. Lackner, I. Schellenberg, R. Poettgen, D. Johrendt, Z. Anorg. Allg. Chem. **635**, 2242 (2009).

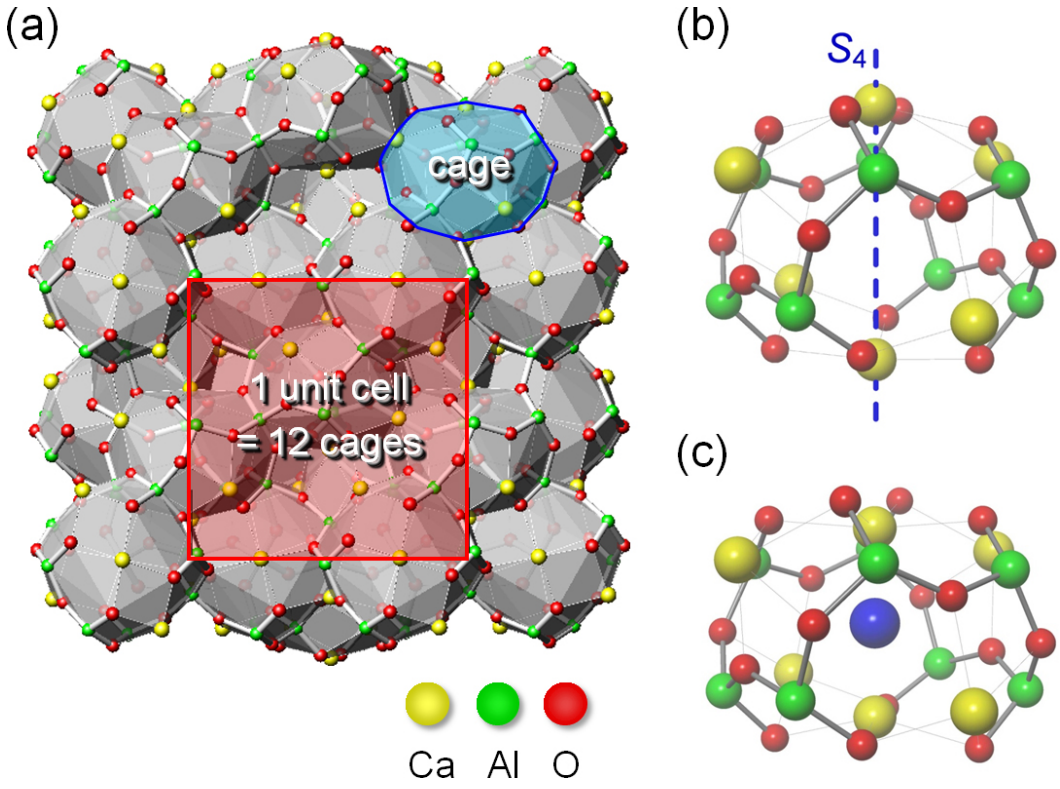

Figure 1-1. Crystal structure of C12A7. (a) An overview from (100) direction. The structure is composed of one type of cage structure (blue shade). The red square corresponds to a unit cell including 12 cages. (b) A cage structure without encage anion. An S_4 symmetry axis passing through two Ca ions is indicated. (c) A cage structure incorporating an anion. Theoretical calculations predict that the Ca atoms on the S_4 axis are displaced to cage center, induced by the encaged anion.

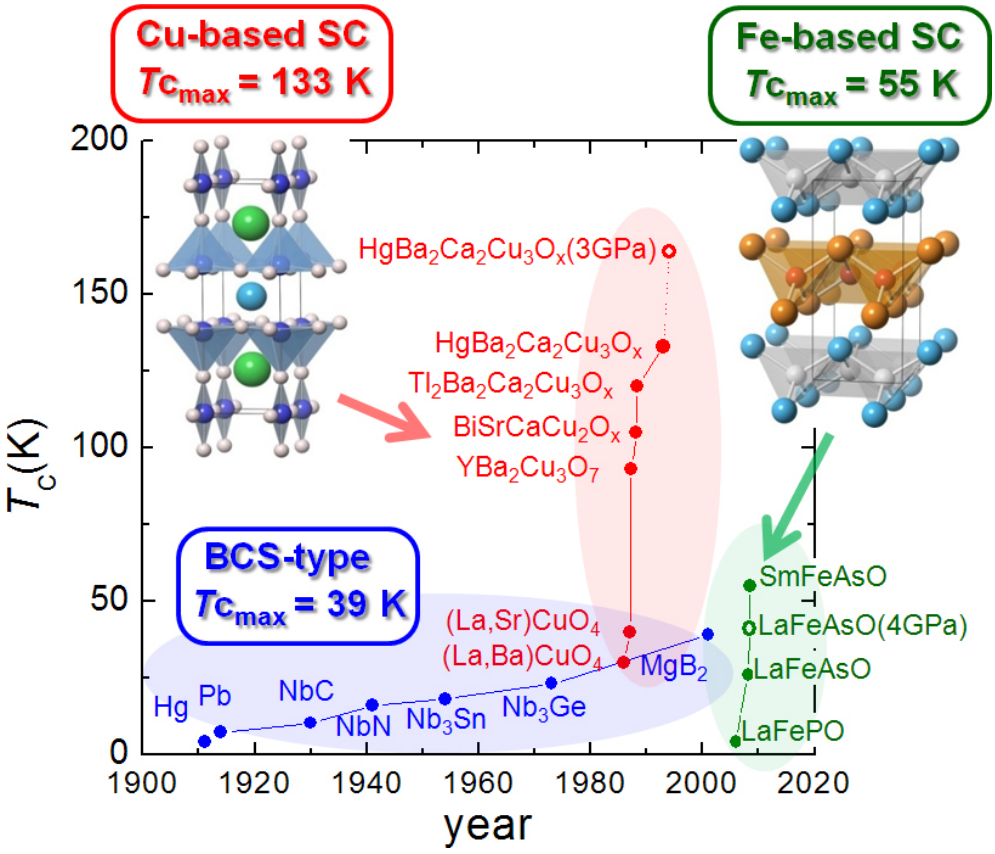

Figure 1-2. The history of superconductors and developments of the superconducting temperatures (T_c). The open symbols represent the records under high pressure.

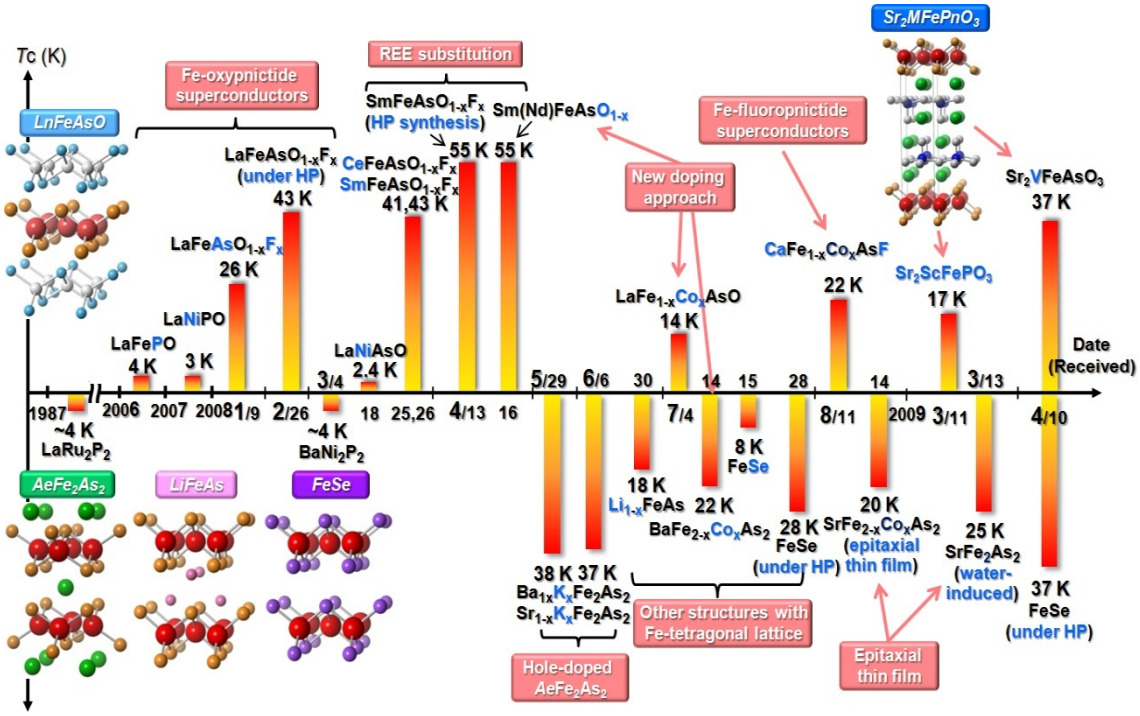

Figure 1-3. Recent advances of Fe(Ni)-based superconductors and the superconducting temperature (T_c). The upper side represents the progresses of the 1111-type and 21113-type compounds, while the lower side represents that of 122-type, 111-type and 11-type compounds. The horizontal axis indicates the received date for journals or the submitted date for a preprint server "arXiv" (Cond-mat). The remarkable points are colored with blue in the chemical formulae.

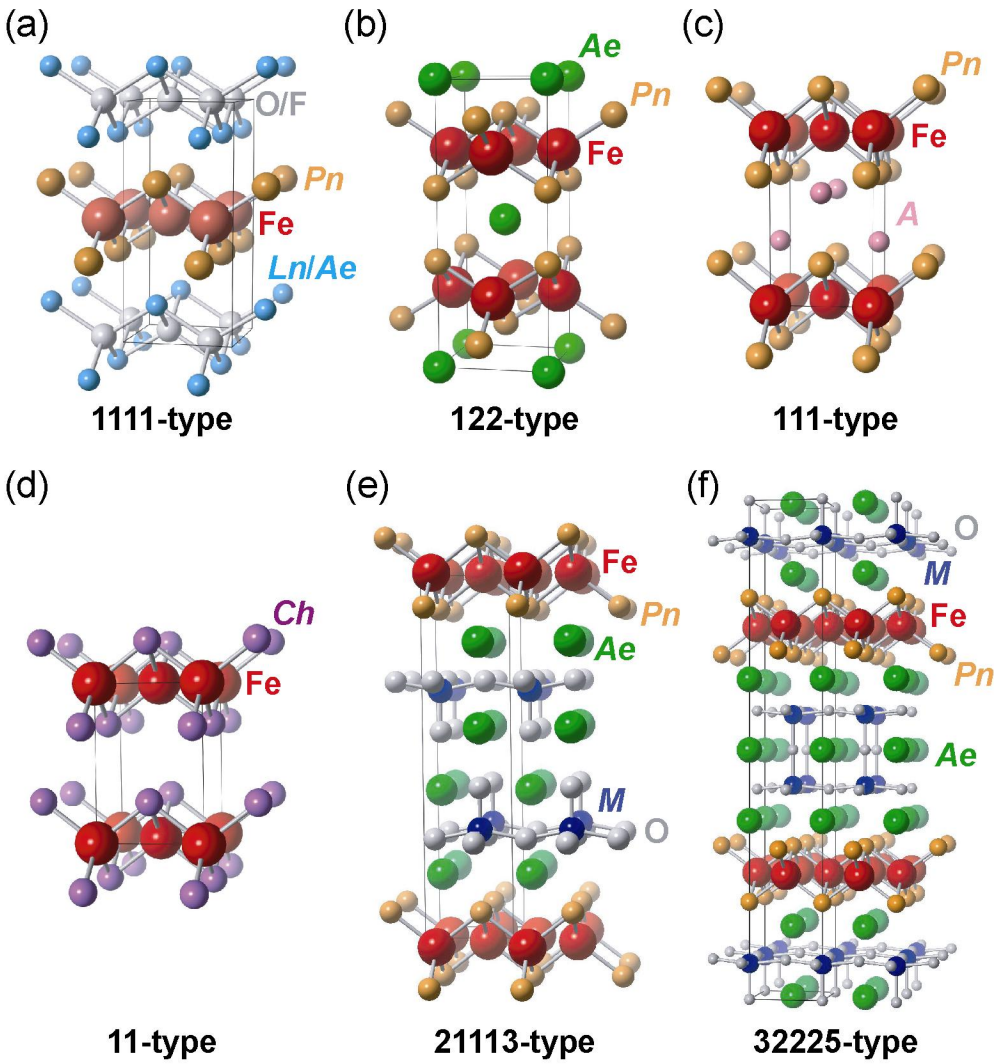

Figure 1-4. The crystal structures of the reported Fe-based superconductors for *Ln*Fe*Pn*O (1111) type (a), AeFe$_2$$Pn_2$ (122) type (b), *A*Fe*Pn* (111) type (c), Fe*Ch* (11) type (d) Ae_2MFePnO$_3$ (21113) type (e), Ae_3M_2Fe$_2$$Pn_2O_5$ (32225) type (f). Each symbol represents as follows; *Ln*: rare-earth elements, *Ae*: alkali earth elements, *A*: alkali elements, *Pn*: Pnictogen, *Ch*: Chalcogen, *M*: 3d transition elements. The black lines in each structure represent unit cells.

	Cu-based SC	Fe-based SC
SC layer	CuO_2 plane	FeAs layer
Parent phase	Mott Insulater	Bad metal (semi-metal) multi-pockets on E_F
Band structure near Fermi level	Single-band Cu3d_{x2-y2} and O2p orbital	Multi-band complicated Fe3d orbitals
Doping method	Oxygen vacancy, Indirect doping	+ Direct doping (Co, Ni substitution)
Phase diagram	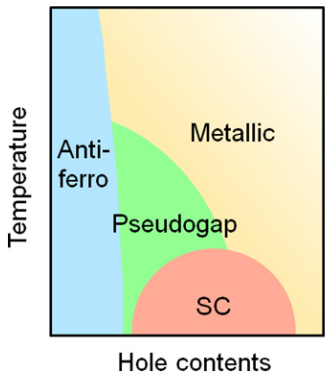	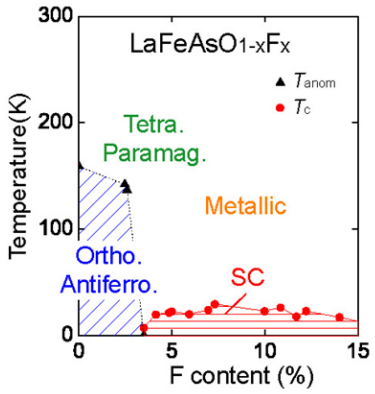

Figure 1-5. Similarities and differences between Cu-based and Fe-based superconductors (SC). The schematic phase diagram captured its typical characters are shown for Cu-based superconductors.

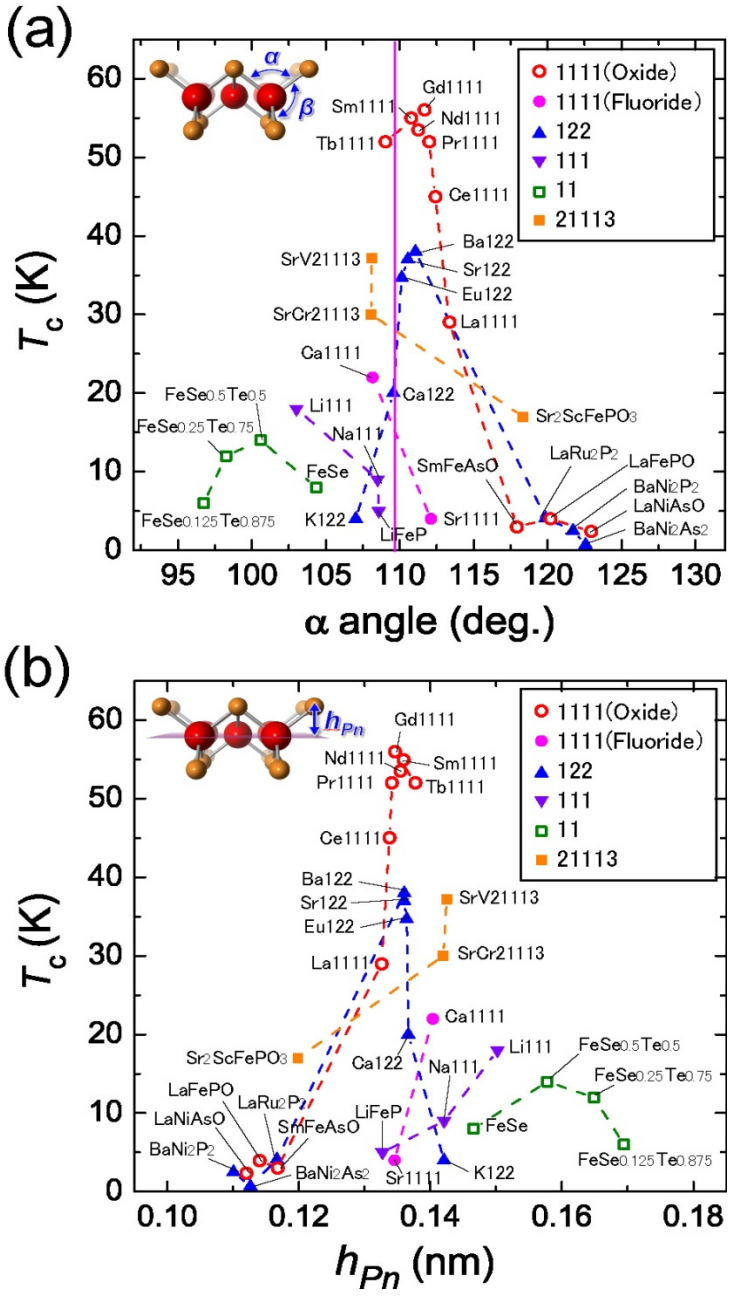

Figure 1-6. The T_c plots arranged as a function of As-Fe-As angle, α (a) and pnictgen height, h_{Pn} (b). The insets show the explanation drawing of α angle and h_{Pn}. The selected T_c values and structural data are those in Ref. 41, 44, 49, 52, 54, 55, 56, 58, 59, 60, 71, 72, 88, 92, 93, 97, 107, 111, 114, 125, 127–140.

Chapter 2: Distribution of Encaged Anion and Anion-induced Cage Deformation in $[Ca_{24}Al_{28}O_{64}]^{4+}\cdot 4X^{-}$ ($X^{-} = O^{2-}, OH^{-}, H^{-}$)

2.1. Introduction

How the incorporated anions distribute in the cage of C12A7 and how they interact with the cage framework are interesting issues of C12A7 to understand the various unique physical and chemical properties. Influence of the anion incorporation on the cage geometry has been predicted by theoretical studies using *ab initio* embedded cluster calculations; two Ca^{2+} ions on the S_4 axis are displaced toward the inner side of the cage upon accommodation of extra-framework anions due to their Coulomb interaction, and monovalent anions tend to locate at the cage center, while the position of divalent O^{2-} ion is off-center and off S_4 axis [1,2]. In this chapter, it is demonstrated that different types of the Ca^{2+} ion displacement are induced by O^{2-} and OH^{-} ions from precise analyses of high-quality X-ray diffraction (XRD) data. The crystal structure of H^{-} ion incorporated C12A7 was also examined and compared with them.

2.2. Experimental and Analysis

Synchrotron powder XRD measurements and the maximum entropy method combined with the Rietveld (MEM/Rietveld) analysis were examined [3]. The MEM analysis is effective to detect and examine the unknown structure changes and abnormal electron density distribution which are not modeled in the Rietveld analysis. This feature enables us to determine the displacements of Ca^{2+} ions and positions of extra-framework anions.

Three types of anion-incorporated C12A7 crystals, stoichiometric C12A7 (C12A7:O^{2-}), fully OH^{-} ion-incorporated C12A7 (C12A7:OH^{-}) and fully H^{-} ion-incorporated C12A7 (C12A7:H^{-}) are prepared for the structure analysis, respectively. A C12A7 single crystal grown

by a floating zone (FZ) method [4] was used as the C12A7:O^{2-} crystals. The OH^- ion and oxygen radical ions (O^- and O_2^-) concentration estimated by infrared absorption spectroscopy [5] and electron spin resonance (ESR) [6] are below 3×10^{19} cm^{-3} and 3×10^{18} cm^{-3}, respectively. For the preparation of C12A7:OH^-, stoichiometric C12A7 powder was annealed at 1193 K for 2 days in a N_2 gas saturated with water vapor at ~300 K ($p(H_2O)$ ~0.04 atm) [7]. The OH^- ion concentration estimated by infrared absorption spectroscopy was $\sim 2.3 \times 10^{21}$ cm^{-3}, which suggests that O^{2-} ions are fully substituted by OH^- ions. To prepare the C12A7:H^- crystals, FZ crystal was annealed with CaH_2 pellets in a evacuated quartz tube. According to the ^1H MAS (magic angle spinning)-NMR measurement using C12A7:OH^- as a standard sample, the ratio of integrated intensity was H^- : OH^- = 1.25 : 1, while the electron concentration estimated by ESR measurements was $\sim 2 \times 10^{19}$ cm^{-1} [8]. These results indicate that that encaged anions are mostly substituted by H^- ion.

The synchrotron powder XRD measurements were performed at BL02B2 beamline [9] in SPring-8 at 298 K in an ambient atmosphere. The incident X-ray wavelength was 0.05 nm, and the reflection data ranging from 4° to 70° with a 0.01° step in 2θ, which corresponds to 0.044 nm resolution, were used for the analysis. A unit cell was divided into 64 × 64 × 64 parts and electron densities on each pixel were determined by the MEM analysis with using a computer program ENIGMA [10].

2.3. Results and Discussion

According to a previous X-ray single crystal structure analysis of a stoichiometric C12A7, the obtained structure model was composed of six sites, namely, five sites for framework atoms (Ca1, Al1, Al2, O1 and O2 site), and one site for the extra-framework O^{2-} ion (O3 site) which was located at a 24d site on S_4 axis position with an occupancy of 1/12 [11]. In this study, three

steps of MEM/Rietveld cycles were operated for each anion-incorporated C12A7 to examine detailed structures with less bias by taking advantages of the MEM method: Firstly, the obtained XRD pattern is fitted using framework-only (five sites) model. Next, the Ca site is divided into two sites keeping the total occupancy to be one for the reason explained below. Finally, a site of the incorporated anion is added to the structure model and the positions are examined.

< Framework-only model >

In the first step, the XRD patterns of each sample are analyzed with the framework-only structure model. These analyses gave poor fitting result with R_I ~8.1% and R_{WP} ~4.3% for C12A7:O^{2-}, R_I ~13.4% and R_{WP} ~7.7% for C12A7:OH^-, R_I ~6.3% and R_{WP} ~3.8% for C12A7:H^-, respectively. Anyway, to clarify the cause of these poor fitting results, preliminary MEM analyses were carried out using the structure factors obtained by the Rietveld analyses. The resultant MEM electron density distributions of each sample (Fig. 2-1(a)~(c)) showed an unusual nonspherical electron distribution at the Ca site; it extends to the inner side of the cage along the S_4 axis, even though the only one Ca site with an isotropic atomic displacement parameter was assumed.

< Ca-split model >

The Rietveld analyses using anisotropic atomic displacement parameters did not improve the fitting results so drastically. Considering the results of theoretical calculations [2], the obtained elongate distribution can be attributed to a spatial displacement of the Ca^{2+} ions induced by the presence of an incorporated anion inside a cage. Provided that the position of Ca are different between anion-occupied and -unoccupied cages, the electron density of the Ca^{2+} ions in the MEM electron density map has a bimodal distribution due to the superposition of the displaced and remained Ca^{2+} ions. Thus, the Ca site of each sample was split into two sites (i.e. Ca1 and Ca2) with keeping the total occupancy constant. As a result, reliable factors were

drastically reduced to R_I ~5.2% and R_{WP} ~3.4% for C12A7:O^{2-}, R_I ~10.1% and R_{WP} ~6.4% for C12A7:OH^-, R_I ~2.9% and R_{WP} ~2.9% for C12A7:H^-, respectively. The reduction of the R factors in each sample is ~1% for R_I and ~3% for R_{WP}, respectively. The resultant occupancies of Ca2 site were for ~0.1 for C12A7:O^{2-}, ~0.3 for C12A7:OH^- and ~0.2 for C12A7:H^-, respectively. The cross sections of obtained MEM electron density distribution on a (100) plane are shown for each sample in Fig.2-2. For the C12A7:OH^-, the electron density corresponding to the OH^- ion clearly appears at the cage center (Fig. 2-2(b)) although no site corresponding to the encaged anion is assumed in the structure model. According to the obtained MEM map of C12A7:O^{2-}, the electron density is likely to distribute away from the cage center (Fig 2-2(a)) in contrast to that of C12A7:OH^-. On the other hand, the electron density distribution in the cage of C12A7:H^- could not be seen clearly from the MEM map (Fig. 2-2(c)) due to the low density.

< Final structure model ~determination of the encaged anion distribution~ >

The positions of the encaged anions in each C12A7 crystal are examined keeping in mind the results of the preliminary MEM/Rietveld analyses. As for C12A7:OH^-, O3 site corresponding to O atom of OH^- ion was added to the structure model, where the hydrogen atom was neglected considering the weak scattering factor. The O3 site can locate three possible sites in the Rietveld structure model; 12*a* site (on the cage center), 24*d* site (on the S_4 axis), 48*e* site (off-center and off-axis), and each occupancy was fixed to 1/3, 1/6 and 1/12, respectively, considering the total amount of encaged anions. The resulting R factors were R_I ~2.5% and R_{WP} ~3.4% for every model and there is almost no difference between them. In the 48*e* model, the refined O3 position is only below ~0.015 nm away from the cage center, which indicates that O3 site is essentially located at the cage center. In addition, the electron density information obtained by following MEM analysis shows the isotropic distribution of the OH^- ion at the cage center (Fig. 2-5(b)), supporting that the incorporated OH^- ion tends to be located at the cage

center.

The position of O3 site in C12A7:O^{2-} was also examined in the same manner as C12A7:OH^-. The Rietveld refinements with 12*a*, 24*d* and 48*e* models were carried out with keeping the occupancy of O3 site to 1/6, 1/12 and 1/24, respectively. The resulting *R* factors using each model are R_I ~3.5% and R_{WP} ~3.0% for the 12*a* model, R_I ~3.0% and R_{WP} ~2.9% for the 24*d* model, R_I ~2.9% and R_{WP} ~2.9% for the 48*e* model, respectively. These results suggest that the O^{2-} ion is not likely to occupy the cage center in contrast to C12A7:OH^-, which is consistent with the result of the preliminary MEM analysis (Fig. 2-2(a)). The refined O3 position with the 48*e* model did not converge to S_4 axis (24*d* site), and the position is significantly displaced from the cage center by ~0.045 nm and from the S_4 axis by ~0.035 nm, In addition, the 48*e* site model gave a little bit lower *R* values than the 24*d* site model, therefore, above results suggest that the 48*e* site is more feasible site for the encaged O^{2-} ion. The reason why the 48*e* model is plausible will be discussed later.

As for the C12A7:H^-, the H1 site was added to the Rietveld structure model as same as the O3 site of the C12A7:O^{2-}, however, the H1 site set to 24*d* or 48*e* site was not converged to a specific position in the refinements due to the weak scattering ability of the H^- ion. The preliminary MEM results did not provide a clear hint, therefore, the H1 site was tentatively set to the 12*a* site with keeping the occupancy to 1/3. The atomic displacement parameter of H1 site was fixed to 2.0 $Å^2$ to avoid it from divergence. Then, the fitting was improved and the resulting *R* factors were significantly reduced to ~2.3% for R_I and ~2.8% for R_{WP}, respectively, although the clear position of H^- ion was not determined.

The final Rietveld fitting results and refined structure parameters were shown in Fig. 2-3 and Table 2-1–4. The other important structure parameters for evaluation of the structure were the occupancies and the positions of Ca2 site. The refined occupancy ratio of Ca1 : Ca2 for

C12A7:OH^- was 0.701(4) : 0.299(4), which is close to the ratio of empty and OH^--occupied cages (2 : 1 = 0.666.. : 0.333..), suggesting that the encaged OH^- ion induces equal inward displacements of two Ca^{2+} ions ("symmetric" Ca displacements). On the other hand, the ratio for the C12A7:O^{2-} was 0.886(2) : 0.114(2), which is significantly deviated from the theoretical ratio of empty and O^{2-} ion-occupied cages (5 : 1 = 0.833.. : 0.166..). In addition, the ratio for C12A7:H^-, Ca1 : Ca2 = 0.789(4) : 0.211(4), was also deviated from the ideal one (i.e. 2 : 1 = 0.666.. : 0.333..). These deviations suggest an "asymmetric" displacement of the Ca^{2+} ions as will be discussed later.

The primary origin of the Ca^{2+} ion displacement along the S_4 axis is attributable to local atomic bonding and lattice structure around the Ca^{2+} ion. The electron density isosurface of C12A7:O^{2-} in Fig. 2-4 demonstrates bondings between framework Al^{3+} and O^{2-} ions have covalent nature, while Ca^{2+} ions appear to be completely isolated at the same density level, indicating their bondings to the framework O^{2-} ions are highly ionic. Furthermore, an inner cage side of Ca^{2+} ion is not screened by framework O^{2-} ions, thereby is exposed completely to the inner space of the cage. Consequently, the Ca^{2+} ion is electrostatically attracted by anionic species in the cages. Thus, the observation of larger displacement by the O^{2-} ion (0.069 nm) than the OH^- ion (0.046 nm) and H^- ion (0.043 nm) is ascribed to difference in their charge states. In contrast, the MEM electron density distributions of framework Al^{3+} and O^{2-} ions are nearly spherical, indicating that their displacements are likely no more than the magnitudes of the thermal vibration. Only two Ca^{2+} ions on the S_4 axis are displaced dominantly by the anion incorporation.

Figure 2-5 displays the two-dimensional electron density map of final MEM analyses. The bimodal distribution of the Ca site in Rietveld analysis can be seen in both MEM maps. Locations of the O^{2-} ion at off-axis position (Fig. 2-5(a)) and OH^- ion at the cage center (Fig.

2-5(b)) are consistent with the theoretical calculations [6]. As for the C12A7:OH^-, the distance from Ca2 to O3 site is ~0.237 nm which is agree well with the distance between Ca and O of other calcium oxyhydrates (~0.24 nm). In the case of C12A7:O^{2-}, the distance between the O3 site and the nearest Ca2 site (~0.18 nm) is far smaller than the sum of their ionic radii (~0.24 nm), provided that the two Ca^{2+} ions are symmetrically displaced in the O^{2-} ion-occupied cage. The apparent spatial proximity can be explained by the "asymmetric" displacement of two Ca^{2+} ions; one Ca^{2+} ion is displaced to the position of the Ca2 site, while the other remains near the Ca1 site, and the O^{2-} ion locates around the middle of the two Ca^{2+} ions as illustrated in Fig. 2-6. The asymmetric displacement in C12A7:O^{2-} ideally provides an 11 : 1 (= 0.9166.. : 0.0833..) occupancy ratio of Ca1 and Ca2 sites. The refined ratio is closer to this value than that expected from the symmetric displacement model, further supporting validity of the asymmetric displacement model. According to a heat capacity measurement of C12A7:O^{2-} at low temperatures, the encaged O^{2-} ion seems to occupy multiple positions in the cage [12]. In the case of 24*d* site model, the O^{2-} ion should occupy a single site for an asymmetric displacement mode, while, the O^{2-} ion can jump to another site in the case of 48*e* site model, which is consistent with the conclusion of the heat capacity measurement. Figure 2-6 illustrates the difference of the anion distribution and Ca displacement between C12A7:O^{2-} and C12A7:OH^-. Such the difference would be caused by the charge state of encaged anion.

In contrast to C12A7:O^{2-} and C12A7:OH^-, the position of the encaged H^- ion have not been determined in the Rietveld analysis as mentioned above. However, the H^- ion is expected to be located at some off-center positions for the following reasons; The refined occupancy ratio of Ca1 : Ca2 = 0.789(4) : 0.211(4) is closer to the ratio expected from the asymmetric displacement model (5 : 1 = 0.833.. : 0.166..) than that expected from the symmetric displacement model (2 : 1 = 0.666.. : 0.333..), suggesting that the asymmetric displacement

model is more dominant in the C12A7:H^-, and in that case, the H^- ion would occupy off-center positions as well as C12A7:O^{2-}. In addition, if the H^- ions occupy the cage center (12*a* site) regularly, the electron density would be high enough to detect the occupied position according to a theoretical expectation [13]. Nevertheless, the actual analysis did not show such the results, therefore, the H^- ion would be distributed some disorder sites. According to the theoretical calculation, encaged H^- ion locates at the cage center and induces symmetric Ca displacements [14], however, it is disagree with our analysis results. An NMR study of C12A7:H^- has revealed that the encaged H^- ion has more broadened 1s orbital than conventional hydrides [8], which might lead to such the complex structure. In any case, the accurate position of the H^- ion should be determined by neutron diffraction method taking advantage of high sensitivity for hydrogen atoms.

2.4. Conclusion

In summary, results of MEM/Rietveld analyses have revealed that an encaged O^{2-} ion induces large and asymmetric displacement of a Ca^{2+} ion on the S_4 axis and occupies off-center and off-axis position. In contrast, encaged OH^- ion induces small and symmetric displacement of the Ca^{2+} ions, keeping itself at the center position of the cage (12*a* site). These differences would be caused mostly by the different charge states of the extra-framework anions. The position of encaged H^- ion has not been clarified yet due to the weak scattering ability and broadened electron distribution of the H^- ion, however, it is likely to occupy some off center sites and seems to induce asymmetric Ca displacement like as the encaged O^{2-} ion.

References

[1] P. V. Sushko, A. L. Shluger, K. Hayashi, M. Hirano, H. Hosono, Phys. Rev. B **73**, 14101 (2006).

[2] K. Hayashi, P. V. Sushuko, D. Munoz-Ramo, A. L. Shluger, S. Watauchi, I. Tanaka, S. Matuishi, M. Hirano, H. Hosono, J. Phys. Chem. B **111**, 1946 (2007).

[3] M. Takata, E. Nishibori, M. Sakata, Z. Kristallogr. **216**, 71 (2001).

[4] S. Watauchi, I. Tanaka, K. Hayashi, M. Hirano, H. Hosono, J. Cryst. Growth **237–239**, 801 (2002).

[5] K. Hayashi, M. Hirano, H. Hosono, J. Phys. Chem. B **109**, 11900 (2005).

[6] K. Hayashi, S. Matsuishi, M. Hirano, H. Hosono, J. Phys. Chem. B **108**, 8920 (2004).

[7] K. Hayashi, M. Hirano, S. Matuishi, H. Hosono, J. Am. Chem. Soc. **124**, 738 (2002).

[8] P. V. Sushuko *et al.* unpublished.

[9] E. Nishibori, M. Takata, K. Kato, M. Sakata, Y. Kubota, S. Aoyagi, Y. Kuroiwa, M. Yamakata and N. Ikeda Nucl. Instrum. Methods A **467/468** 1045 (2001).

[10] H. Tanaka, M. Takata, E. Nishibori, K. Kato, T. Ishii, M. Sakata, J. Appl. Cryst. **35**, 282 (2002).

[11] H. Bartl, T. Scheller, Neues Jahrb. Mineral. Monatsh. **35**, 547 (1970).

[12] Y. Kohama, T. Tojo, H. Kawaji, T. Atake, S. Matsuishi, H. Hosono, Chem. Phys. Lett. **421**, 558 (2006)

[13] private communication.

[14] P. V. Sushko, A. L. Shluger, M. Hirano, H. Hosono, J. Ame. Chem. Soc. **129**, 942 (2007).

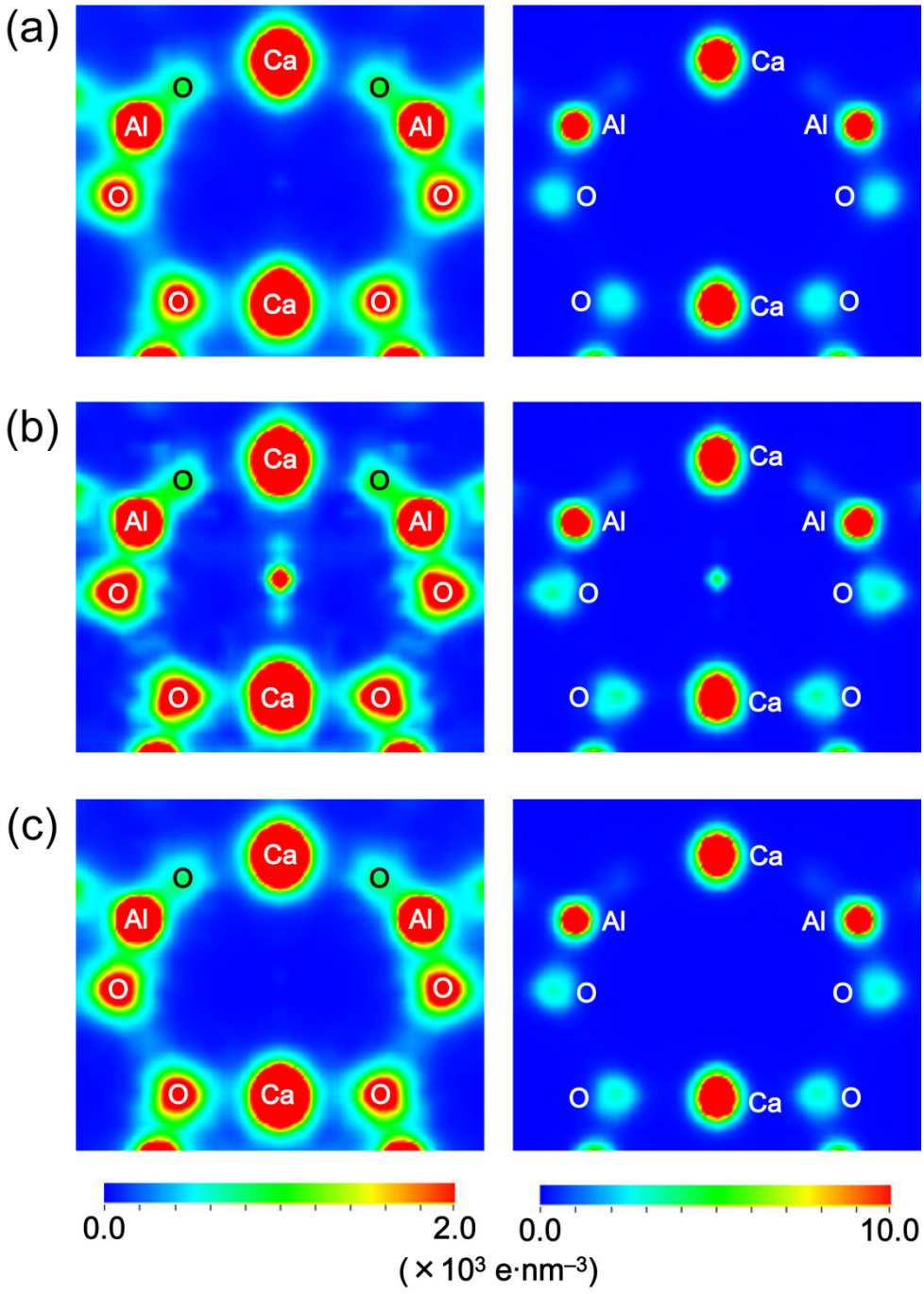

Figure 2-1. The results of first preliminary MEM analyses of C12A7:O^{2-} (a), C12A7:OH^{-} (b) and C12A7:H^{-} (c) using structure factors obtained by Rietveld analysis with the framework-only models. Each electron density map corresponds to a cross section of one cage clipped from a (100) plane. The MEM maps with ranges of up to 2×10^3 electrons·nm^{-3} (left) and 1×10^4 (right) are shown for each sample, respectively. Abnormal distributions of Ca elongating toward the cage center can be observed in every MEM map, in particular, can be seen clearly in the high electron density regions.

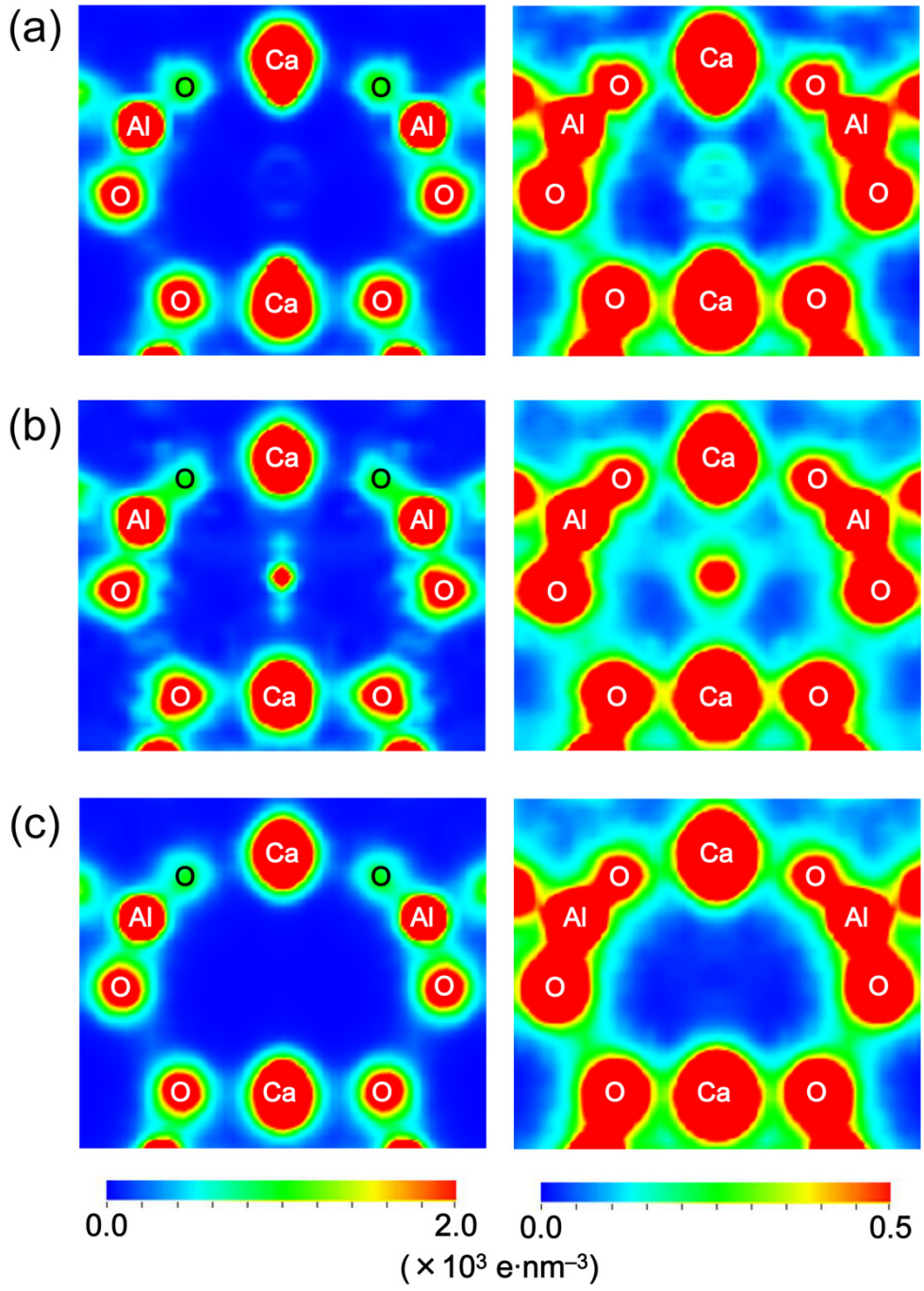

Figure 2-2. The results of second preliminary MEM analyses of C12A7:O^{2-} (a), C12A7:OH^- (b) and C12A7:H^- (c) using structure factors obtained by Rietveld analysis with the Ca-split models. Each electron density map corresponds to a cross section of one cage clipped from a (100) plane. The MEM maps with ranges of up to 2 × 10^3 electrons·nm^{-3} (left) and 0.5 × 10^3 (right) are shown for each sample, respectively. Electron density corresponding to the encaged anion can be seen at around the cage center for the low electron regions of C12A7:O^{2-} and C12A7:OH^-, even though no site was assumed for the encaged anion in the preceding Rietveld analyses.

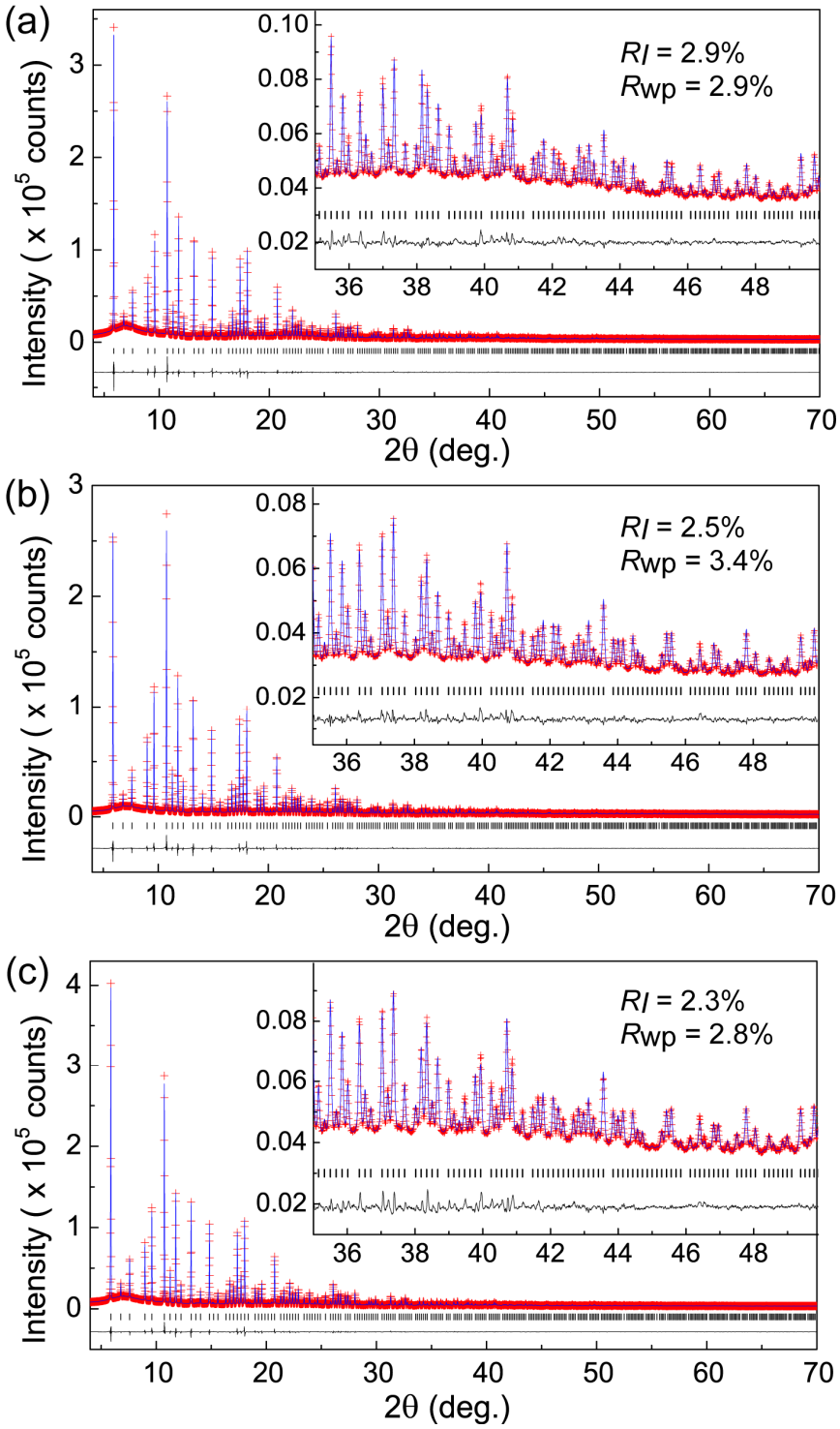

Figure 2-3. The final Rietveld fitting results for C12A7:O^{2-} (a), C12A7:OH^- (b) and C12A7:H^- (c). Insets show magnified views from 35 to 50 degrees. The calculated reflection angles and the difference between the measured and calculated intensities are indicated on the lower side of graphs.

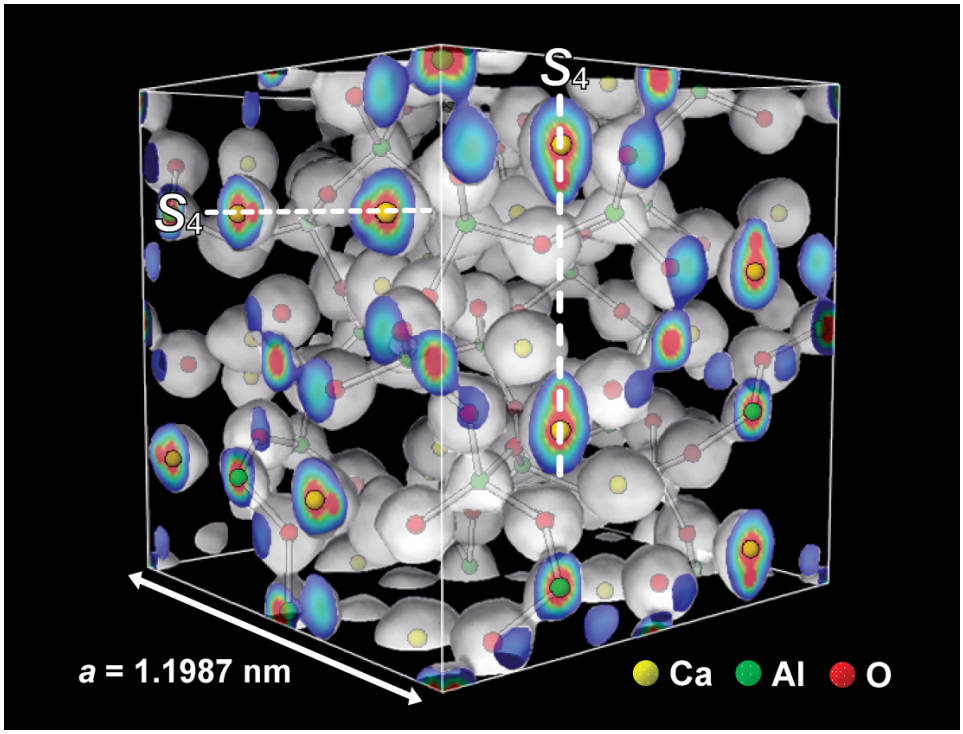

Figure 2-4. Crystal structure of C12A7. An isosurface of electron density at 0.65×10^3 electrons·nm^3 obtained by the MEM/Rietveld analysis of C12A7:O^{2-} sample is also superposed. The S_4 axis points to <100> direction and passes through two Ca^{2+} ions and the cage center.

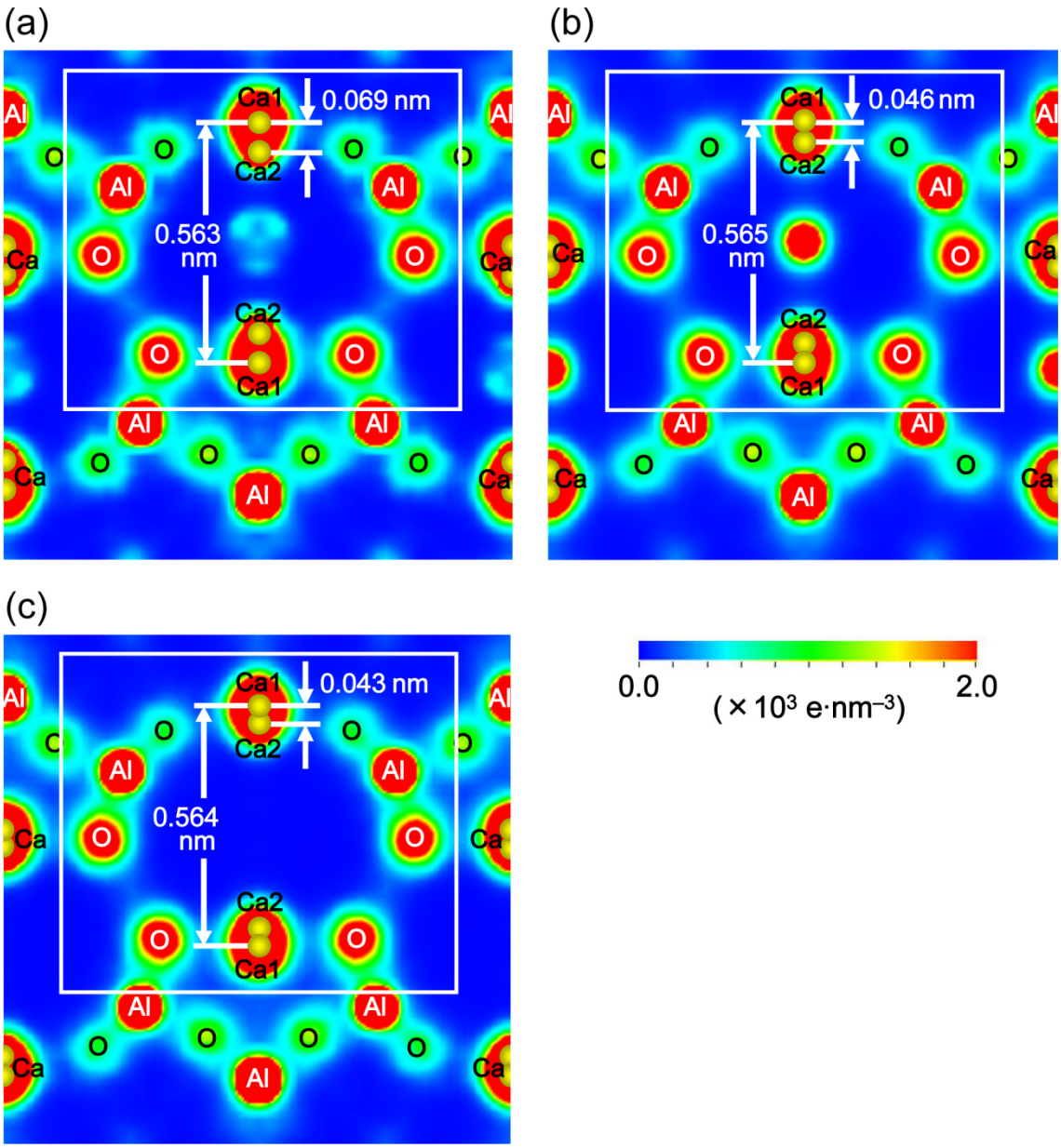

Figure 2-5. MEM electron density distribution on a (400) plane in C12A7:O^{2-} (a), C12A7:OH^{-} (b) and C12A7:H^{-} (c), respectively. The superposed yellow spheres represent the position of Ca1 and Ca2 determined by final Rietveld analyses. The area enclosed by a white line corresponds to a cross section of one cage including the cage center. The Ca1–Ca1 and Ca1–Ca2 distances along the S_4 axis are indicated.

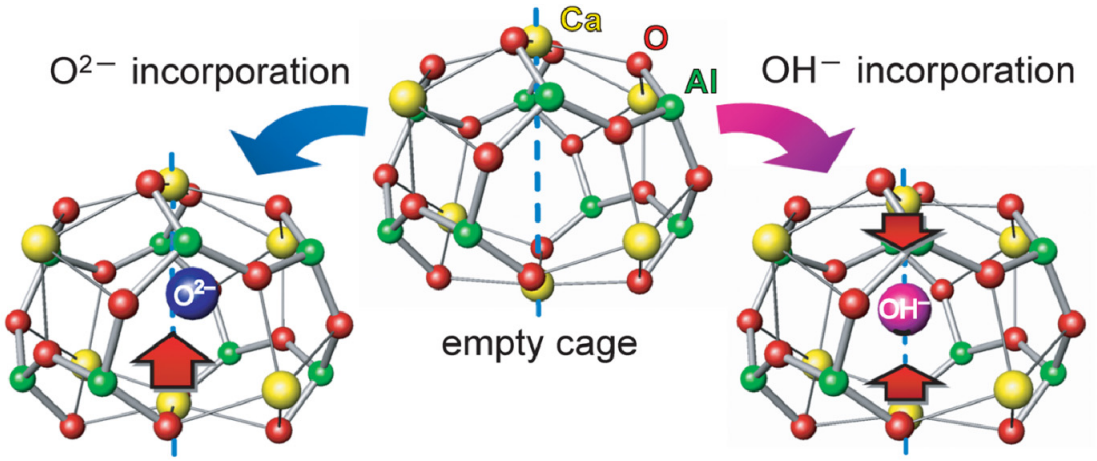

Figure 2-6. Schematic structure model for the cage deformation of C12A7 encaging O^{2-} and OH^- ions. The encaged O^{2-} ion induces large asymmetric displacement of two Ca^{2+} ions on the S_4 axis and occupies off-center and off-axis position (48*e* site). In contrast, OH^- ion induces small and symmetric displacement of the Ca^{2+} ions, keeping itself at the center position of the cage (12*a* site).

Table 2-1. Crystal information for C12A7:O^{2-}, C12A7:OH^- and C12A7:H^- obtained from the final Rietveld analyses.

	C12A7:O^{2-}	C12A7:OH^-	C12A7:H^-
Composition formula	$C_{12}Al_{14}O_{33}$	$C_{12}Al_{14}O_{34}H_2$	$C_{12}Al_{14}O_{32}H_2$
Structural formula	$[C_{24}Al_{28}O_{64}]^{4+}\cdot 2O^{2-}$	$[C_{24}Al_{28}O_{64}]^{4+}\cdot 4OH^-$	$[C_{24}Al_{28}O_{64}]^{4+}\cdot 4H^-$
Formula weight	2773.315	2809.346	2745.348
Crystal system	cubic	cubic	cubic
Space group	$I\bar{4}3d$	$I\bar{4}3d$	$I\bar{4}3d$
Z	2	2	2
Lattice constant (nm)	1.198748(3)	1.197338(3)	1.197424 (3)
Unit cell volume (nm^3)	1.7226	1.7165	1.7169
Calculated density (g/cm)	2.673	2.718	2.655
Number of reflections	976	970	970
R_I	2.9	2.5	2.3
R_{wp}	2.9	3.4	2.8
Anion-induced Ca displacement (nm)	0.069	0.046	0.043
Refined Ca1: Ca2 ratio	0.886(2) : 0.114(2)	0.701(4) : 0.299(4)	0.789(4) : 0.211(4)

Table 2-2. Structural parameters of C12A7:O^{2-} refined by the final Rietveld analysis. The atomic displacement parameters of Ca2 and O3 sites were fixed to that of Ca1 and O2 site, respectively.

	site	g	x	y	z	B (Å^2)
Ca1	24*d*	0.886(2)	0.1401(1)	0	0.25	0.75(1)
Ca2	24*d*	0.114(2)	0.1977(5)	0	0.25	〃
Al1	16*c*	1	0.0189(1)	0.0189(1)	0.0189(1)	1.00(2)
Al2	12*b*	1	0.875	0	0.25	0.50(2)
O1	48*e*	1	0.1510(1)	0.9619(1)	0.0571(1)	1.07(3)
O2	16*c*	1	0.9365(1)	0.9365(1)	0.9365(1)	1.20(6)
O3	48*d*	1/24	0.3445(2)	0.0365(2)	0.2425(5)	〃

Table 2-3. Structural parameters of C12A7:O^{2-} refined by the final Rietveld analysis. The hydrogen atom of OH^- ion was neglected in the analysis.

	site	*g*	*x*	*y*	*z*	*B* (Å^2)
Ca1	24*d*	0.701(4)	0.1390(1)	0	0.25	0.59(1)
Ca2	24*d*	0.299(4)	0.1771(3)	0	0.25	0.59(1)
Al1	16*c*	1	0.0189(1)	0.0189(1)	0.0189(1)	0.37(2)
Al2	12*b*	1	0.875	0	0.25	0.41(2)
O1	48*e*	1	0.1499(1)	0.9634(1)	0.0562 (1)	1.05(3)
O2	16*c*	1	0.936521)	0.9362(1)	0.9362(1)	1.22(5)
O3	12*a*	1/3	0.375	0	0.25	2.5(5)

Table 2-4. Structural parameters of C12A7:H^- refined by the final Rietveld analysis. The atomic displacement parameter of H1 site was fixed to 2.0 to avoid it from divergence.

	site	*g*	*x*	*y*	*z*	*B* (Å^2)
Ca1	24*d*	0.789(4)	0.1396(1)	0	0.25	0.60(1)
Ca2	24*d*	0.211(4)	0.1752(2)	0	0.25	0.57(5)
Al1	16*c*	1	0.0185(1)	0.0185(1)	0.0185(1)	0.40(2)
Al2	12*b*	1	0.875	0	0.25	0.41(2)
O1	48*e*	1	0.1501(1)	0.9632(1)	0.0561 (1)	1.05(3)
O2	16*c*	1	0.9361(1)	0.9361(1)	0.9361(1)	1.26(6)
H1	12*a*	1/3	0.375	0	0.25	2.0

Chapter 3: Crystal Structure of C12A7 Electride and Metal-Insulator Transition

3.1. Introduction

Discoveries of conductive C12A7 crystals, such as C12A7:H^- [1] and C12A7 electride [2], urge theoretical analyses and experimental approaches for their electronic structures. According to the results, the cages in C12A7 form an additional conduction band called "cage conduction band (CCB)" [3-6]. The CCB is located 1–2 eV below the bottom of "framework conduction band" which is primarily composed of Ca 5s orbitals. The electrons with low concentration induce a large lattice deformation due to the Coulomb attractive force between the entrapped electron and the two Ca^{2+} ions on the cage wall in the same manner as the anion-encaged C12A7 as shown in the previous chapter, causing electron localization. Consequently, the conduction occurs via the hopping of the electron from a localized deformed cage (an isolated quantum dot state) to the CCB (i.e. by polaron). This is the reason why the drift mobility is much smaller than 1 $cm^2 \cdot V^{-1} \cdot s^{-1}$, and the conductivity shows a thermally activated behavior in the electron-doped C12A7 reported previously [1,2,7–9].

Some reduction processes enable the extra-framework oxide (O^{2-}) ions to be replaced with electrons [1,2,10,11]. Among them, thermal annealing of C12A7 single crystals in Ca metal vapor at 700°C led to the highest electrical conductivity of 80 $S \cdot cm^{-1}$ at 300 K [2] at that moment. However, the Ca treatment needs a long duration (10 days for a 0.4 mm thick sample) to extract the extra-framework oxide ions because the annealing temperature is limited to 700°C so that C12A7 does not react with Ca. In addition, the extraction of the extra-framework O^{2-} ions by Ca vapor consequently forms a surface CaO layer, which works as a barrier for out-diffusion of the extra-framework O^{2-} ion. These two factors make complete replacement of

the extra-framework O^{2-} ions by electrons almost impossible. In this chapter, these drawbacks have been overcome by employing a Ti treatment because Ti forms stable non-stoichiometric oxides over a wide chemical composition range ($1 < x < 2$ in TiO_{2-x}) and the out-diffusion of the extra-framework O^{2-} ions from C12A7 is not blocked even if a thick titanium oxide layer completely covers the sample surface. In addition, higher annealing temperatures up to 1300°C can be used because Ti does not react with C12A7 up to this temperature. Because an increase in the temperature from 700 to 1100°C enhances the diffusion of the extra-framework O^{2-} ions in C12A7 by several orders of magnitude [12,13], the treatment time can be drastically shortened.

In this chapter, the crystal structure of the Ti treated metallic C12A7 electride was examined by MEM/Rietveld analysis using the synchrotron powder XRD pattern, and the relation with the metal-insulator transition was discussed, assisted by the density functional theory (DFT) calculation. The obtained MEM results clearly suggest that encaged O^{2-} ions almost perfectly extracted by the Ti treatment. The cage deformation induced by anion-incorporation is hardly observed in the fully electron-doped C12A7, which is in contrast to the situation at low electron density according to theoretical calculations. Such the structural changes contribute the metal-insulator transition accompanied with a sharp enhancement of the electron drift mobility.

3.2. Experimental and Calculation

Czochralski (CZ)-grown C12A7 single crystals [14] were subjected to the Ti treatment to dope electrons (Fig. 3-2(b)). The crystal was transparent, but had an orange tint (Fig. 3-2(a)) due to trace Ir ions (concentration ~5×10^{17} cm^{-3}) unintentionally incorporated from the Ir crucible used in the CZ process. The grown single-crystal ingots were sliced into (110)-cut 25 mmφ × 1

mm plates or ~ 10 × 3 × 3 mm^3 blocks. These single-crystals were sealed in a silica glass tube (inner volume ~ 10 cm^3) with Ti metal powders (~5 g) under a vacuum of ~ 10^{-3} torr. Then the sealed tube was thermally annealed at temperatures between 900−1100°C for 24−72 hour. The Ti treatment replaces all or a part of the extra-framework O^{2-} ions with electrons by reductive reaction, and electron concentration of the sample was adjusted by changing temperature and duration of the treatment. The TiO_x layer deposited on the surfaces of the Ti-treated samples was mechanically removed after the treatment.

The electron concentrations of samples were evaluated from the optical reflection spectra of the single crystals [15]. The electrical conductivity was measured by the four-probe method using Pt electrodes. Synchrotron pattern XRD measurement and MEM/Rietveld analysis of a fully-electron-doped C12A7 were carried out in the same manner as described in the chapter 2.

VIENNA *ab initio* simulation package (VASP) [16] was used to know quantum-mechanically stable structures and electronic structures for three compositions, (i) insulating $[Ca_{24}Al_{28}O_{64}]^{4+}\cdot(2O^{2-})$, (ii) intermediate $[Ca_{24}Al_{28}O_{64}]^{4+}\cdot(O^{2-})\cdot(2e^{-})$ and (iii) metallic $[Ca_{24}Al_{28}O_{64}]^{4+}\cdot(4e^{-})$, using the projector-augmented wave method and the Pedrew-Burke-Ernzerhof (PBE) form of the generalized gradient approximation functional. A plane-wave energy cutoff of 500 eV and a 2 × 2 × 2 *k*-mesh were used. Isosurfaces of the wave functions ($|\Psi|^2$) are drawn by the code VESTA [17].

3.3. Results and Discussion

Figure 3-3(a) shows the Arrhenius plot of the electrical conductivities (σ) for the Ti-treated single crystals with different electron concentrations (N_e). The Arrhenius plot has a negative slope when the electron concentration is low, indicating that a thermally activated mechanism such as hopping controls the migration of the electrons. On the other hand, the

temperature dependence vanishes in the sample with N_e ~9.7 × 10^{20} cm^{-3} (N_{th}), demonstrating that the electron conduction is degenerated, and finally, the slope becomes positive around room temperature at larger N_e values. The conductivity extrapolated to 0 K (σ_{0K}) as a function of N_e (Fig. 3-3(b)) shows this systematic change more clearly: σ_{0K} starts to increase from zero to a finite value at $N_e = N_{th}$, confirming an metal-insulator (MI) transition, and σ_{0K} superlinearly increases with N_e, showing a sharp increase in the drift mobility (from ~0.1 to 4 $cm^2 \cdot V^{-1} \cdot s^{-1}$) for $N_e > N_{th}$ (inset of Fig. 3-3(b)). These observations demonstrate that the insulating C12A7 is converted to a metal by replacing more than half of the extra-framework oxide ions by electrons. This MI transition accompanies a sharp increase in the drift mobility ($\acute{\imath}_e$) from ~0.1 to 4 $cm^2 \cdot V^{-1} \cdot s^{-1}$ as N_e increases. It should be noted that the doping and conduction mechanisms in C12A7 are much different from those in conventional semiconductors [18] due to the unique crystal and electronic structures of C12A7.

In typical semiconductors such as phosphorus-doped Si [19], the MI transition occurs due to the percolative overlap of the donor wave functions, as explained by Mott in terms of the critical donor concentration N_c [20], which follows the empirical relation $N_c^{1/3} \cdot R_c$ ~0.25 (R_c denotes the radius of the electron orbital) [21]. When the N_{th} value of ~1 × 10^{21} cm^{-3} is put into this relation, the obtained R_c value is 0.26 nm, which is close to the radius of the crystallographic cage embedded in C12A7 (0.25 nm). Thus, it is feasible that the MI transition in C12A7 occurs via the percolation of the"donor" orbitals. However, this view is not directly applicable to C12A7 because even an "undoped" stoichiometric C12A7 crystal has a "donor wave function" in each empty cage as a component of the CCB. Although the "donor wave function" intrinsically exists, the electrons doped to the CCB do not contribute to the band conduction at $N_e < N_{th}$ at low temperatures because the electron is localized in a cage forming an F^+-like center [2] due to the lattice relaxation as described above.

To clarify the origin of the metal-insulator transition, the MEM/Rietveld analysis of C12A7 electride (C12A7:e^-) with N_e ~2.3 × 10^{21} cm^{-3} (theoretical the maximum concentration) was conducted. The framework-only model (see chapter 2) was used for an initial Rietveld structure model. The results of the Rietveld analysis gave reasonably low R factors, R_I ~2.6% and R_{WP} ~2.8% (Fig. 3-4), which is comparable to the final fitting results of other anion-encaged C12A7 in the previous chapter even though the Ca splitting or addition of O3 ion was not modeled in the analysis. The following MEM analysis was carried out using the obtained structure factor. The resultant electron density distribution (Fig. 3-5(c)) shows that the density distribution of Ca site is isotropic in contrast to the oval distribution for anion-encaged C12A7 (Fig. 2-1 in the chapter 2), which suggests that the C12A7:e^- essentially has single-site Ca distribution. The density distribution in the cage is very flat and below 50 e·nm^{-3}. These MEM results indicate that the assumed framework-only model well agrees with the actual structure of C12A7:e^-. The Ca split model did not improve the fitting results significantly in contrast to the case of other anion-encaged C12A7 crystals. In addition, when an O3 site was added to the model for residual extra-framework O^{2-} ions, the refined occupancy converged to zero, suggesting the complete elimination of the O^{2-} ions was achieved as supported by the optical reflection measurement. The final structure parameters and crystal information of the fully-electron-doped C12A7 electride are shown in Table 3-1 and 3-2.

The MEM electron density maps of stoichiometric C12A7 (C12A7:O^{2-} in the chapter 2) and fully-electron doped C12A7 electride (C12A7:e^-) are compared in Fig. 3-5. The distribution of the Ca ions of C12A7:O^{2-} is elongated to the cage center, indicating that partial Ca^{2+} ions are displaced by the coordinating encaged O^{2-} ions due to the Coulomb interaction. The distance of the Ca displacement is 0.069 nm according to the Rietveld analysis result. In contrast, the map of C12A7:e^- (Fig. 3-5(c)) shows spherical density distribution for each atom, indicating that Ca

displacement and other lattice deformation are released in the fully-electron-doped C12A7. That is, the shapes of all cages are homogenized and becomes close to that of the empty cage of C12A7:O^{2-}, suggesting the electrons are distributed uniformly over all the cages within an accuracy of the MEM/Rietveld analysis.

Figure 3-6 shows relaxed lattice structures calculated by DFT with the isosurfaces of the wave function ($|\Psi|^2$) of the 2p level of the extra-framework O^{2-} ions (Fig. 3-6(a)) and those of CCB bottom (isosurface state density) (Fig. 3-6(b)) for (i) stoichiometric C12A7, (ii) $[Ca_{24}Al_{28}O_{64}]^{4+}\cdot(O^{2-})\cdot(2e^-)$, and (iii) fully-electron-doped C12A7 ($[Ca_{24}Al_{28}O_{64}]^{4+}\cdot(4e^-)$). The DFT results are summarized in Fig. 3-6(c) as a schematic energy level diagram. Figure 3-6(a-i) demonstrates that two extra-framework O^{2-} ions respectively occupy the cages at the center and the corners of the unit cell and the other cages are empty in the stoichiometric C12A7. The Ca ions are displaced toward the incorporated O^{2-} ion by ~0.075 nm, approximately agreed with the observed value (0.069 nm) although the Ca ions are displaced symmetrically in contrast to the asymmetric displacement in the analysis result (see chapter 2). Further, each empty cage has an s-like state, and the connection of these states forms the CCB even in the stoichiometric C12A7 (Fig. 3-6(b-i)). On the other hand, the O^{2-}-incorporating cage has no such CCB state because of the entrapping of O^{2-}, whose 2p energy level is located slightly above the valence band maximum of the cage framework (Fig. 3-6(c-i)). Thus, stoichiometric C12A7 has no electron in the CCB and is a band insulator. The DFT result for $[Ca_{24}Al_{28}O_{64}]^{4+}\cdot(O^{2-})\cdot(2e^-)$, where a extra-framework O^{2-} ion is extracted from a cage and two electrons occupy two of the other cages in the unit cell, demonstrates that $D_{Ca\text{-}Ca}$ (0.557 nm) of the electron-incorporating cage becomes larger compared to that of the O^{2-}-incorporating cage (0.427 nm), but it is still smaller than that of the empty cage (0.577 nm). The wave function at the CCB minimum (Fig. 3-6(b-ii)) implies that the electron is still localized in a specific cage, forming an F^+-like center (Fig.

3-6(c-ii)). Figure 3-6(b-iii) is the relaxed lattice structure with the isosurface state density at the CCB minimum of $[Ca_{24}Al_{28}O_{64}]^{4+}\cdot(4e^-)$, revealing that $D_{Ca\text{-}Ca}$ (0.563 nm) of the electron-incorporating cage further expands from that of $[Ca_{24}Al_{28}O_{64}]^{4+}\cdot(O^{2-})\cdot(2e^-)$ and it becomes very close to that of the empty cage. It also indicates the isosurface state density in each cage is equivalent, indicating that the electrons are delocalized over the cages and consequently the cage conduction band has a rather large dispersion of 2 eV (Fig. 3-6(c-iii)).

Figure 3-7 summarizes the relation between crystal structure and the conduction mechanism of C12A7 electride at low and high electron concentration. At low electron concentration, the introduced electrons are trapped in the cage, inducing the Ca displacements, which cause the hopping conduction with low electron mobility below 0.5 $cm^2\cdot V^{-1}\cdot s^{-1}$ (Fig. 3-7(a-i,ii)). In addition, larger lattice deformation induced by residual extra-framework O^{2-} ions modifies and inhomogenizes energy states of each cage, which further prevents it from metallization and helps the electron localization. On the other hand, the lattice deformation are released in the fully-electron-doped C12A7, and the doped electrons are delocalized over all the cages, leading to the metallic conduction with ~4 $cm^2\cdot V^{-1}\cdot s^{-1}$ (Fig. 3-7(b-i,ii)). Release of the cage deformation uniforms the cage structures and the energy levels of each cage, thus, the high symmetric structure would contribute the high mobility of highly-electron-doped C12A7.

The above results explain why the C12A7 electride shows the MI transition with the drastic mobility increase upon the electron doping. The drastic change of the gradient in the inset of Fig.3-3(b) at the critical electron concentration indicates the drastic electronic and structural changes; below the N_{th}, the doped electrons occupy the localized F^+-like state accompanied by the Ca displacements, while, above the N_{th}, the electrons become delocalized and occupy the CCB state, releasing the lattice deformation. The electron delocalization and removal of the extra-framework O^{2-} ions further accelerate the release of cage deformation,

causing to the MI transition accompanied by the sharp drastic mobility increase. Therefore, the lattice relaxation of C12A7 critically affects the conduction mechanism.

It is noteworthy that simple ionic oxides such as Li-doped MgO have not exhibited such a high conductive state, although the F/F^+-like centers can be incorporated at high concentrations similar to the present case [23]. Thus, the three-dimensionally connected high symmetric cage structure in C12A7 plays an essential role in the appearance of the metallic state.

3.4. Conclusion

The fully electron-doped C12A7 electride was fabricated by Ti treatment and the crystal structure was examined by the MEM/Rietveld analysis to discuss the relation with the MI transition. The resultant electron density map indicated the cage deformation dose not occurred in the prepared sample, which is contrast to the anion-incorporated C12A7 shown in the previous chapter. This fact indicates the doped electrons are delocalized and distribute each cage equivalently. Little electron density inner the cage also supports the extra-framework oxide ions are almost perfectly extracted by the reduction process. According to the theoretical embedded cluster calculation [3,4], which corresponds to the low doping concentration, the doped electrons are localized in the cage accompanied by the Ca displacements. However, above the critical electron concentration ($\sim 1 \times 10^{21}$ cm^{-3}), the doped electron would be delocalized with the release of the Ca displacements. Such the structural shift contributes the metal-insulator transition with a sharp enhancement of the mobility. The less structure deformation (i.e. high symmetry) in the highly electron-doped C12A7 also contributes the high conductive state.

References

[1] K. Hayashi, S. Matsuishi, T. Kamiya, M. Hirano, H. Hosono, Nature **419**, 462 (2002).

[2] S. Matsuishi, Y. Toda, M. Miyakawa, K. Hayashi, T. Kamiya, M. Hirano, I. Tanaka, H. Hosono, Science **301**, 626 **(**2003).

[3] P. V. Sushko, A. L. Shluger, K. Hayashi, M. Hirano, H. Hosono, Phys. Rev. Lett. **91**, 126401 (2003).

[4] P. V.Sushko, A. L. Shluger, K. Hayashi, M. Hirano, H. Hosono, Mater. Sci. Eng. C **25**, 722 (2005).

[5] Y. Toda, S. Matsuishi, K. Hayashi, K. Ueda, T. Kamiya, M. Hirano, H. Hosono, Adv. Mater. **16**, 685 (2004).

[6] Z. Li. J. Yang, J. G. Hou, Q. Zhu, Angew. Chem. Int. Ed. **43**, 6479 (2004).

[7] J. L. Dye, Inorg. Chem. **36**, 3816 (1997).

[8] M. I. Bertoni, T. O. Mason, J. E. Medvedeva, A. J. Freeman, K. R. Poeppelmeier, B. Delley, J. Appl. Phys. **97**, 103713 (2005).

[9] J. E. Medvedeva, A. Freeman, J. Appl. Phys. Lett. **85**, 955 (2004).

[10] S. W. Kim, M. Miyakawa, K. Hayashi, T. Sakai, M. Hirano, H. Hosono, J. Am. Chem. Soc. **127**, 1370 (2005).

[11] M. Miyakawa, Y. Toda, K. Hayashi, M. Hirano, T. Kamiya, N. Matsunami, H. Hosono, J. Appl. Phys. **97**, 023510 (2005).

[12] M. Lacerda, J. T. S. Irvine, F. P. Glasser, A. R. West, Nature **332**, 525 (1988).

[13] M. Lacerda, A. R. West, J. T. S. Irvine, Solid State Ionics **59**, 257 (1993).

[14] K. Kurashige, Y. Toda, S. Matuishi, K. Hayashi, K. Ueda, T. Kamiya, M. Hirano, H. Hosono. Cryst. Growth Des. **6**, 1602 (2006).

[15] S. Matsuishi, S. W. Kim, T. Kamiya, M. Hirano and H. Hosono, J. Phys. Chem. C **112**, 4753 (2008).

[16] G. Kresse, J. Furthmuller. Phys. Rev. B **54**, 11169 (1996).

[17] K. Momma F. Izumi, IUCr Newslett. **7**, 106 (2006).

[18] M. Imada, A. Fujimori, Y. Tokura, Rev. Mod. Phys. **70**, 1039 (1998).

[19] H. v. Lohneysen, Curr. Opin. Solid State Mater. Sci. **3**, 5 (1998).

[20] N. F. Mott, Metal-Insulator Transitions; Taylor & Francis: London, (1990).

[21] P. P. Edwards, M. J. Sienko, J. Am. Chem. Soc. **103**, 2967 (1981).

[22] M. Tardio, R. Ramirez, R. Gonzalez, Y. Chen, E. Alves, Phys. Res. B **191**, 191 (2002).

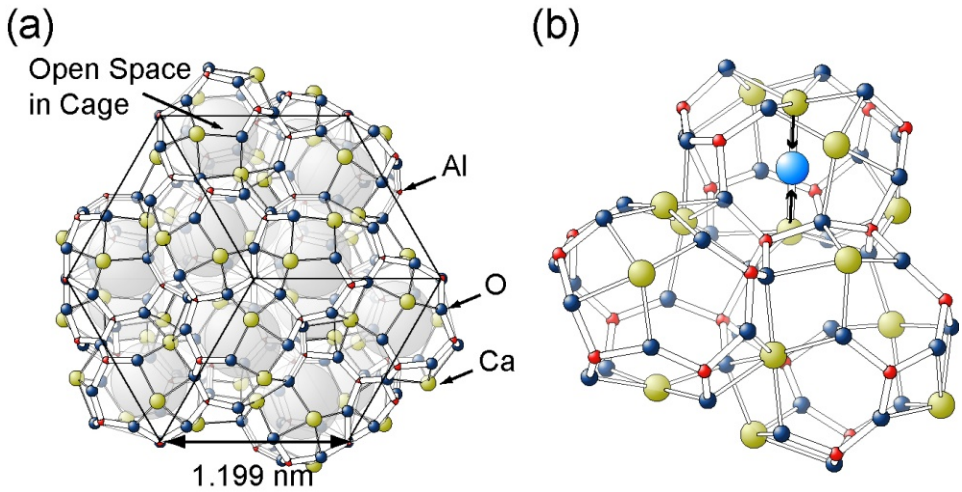

Figure 3-1. Crystal structure of stochiometric C12A7 ($[Ca_{24}Al_{28}O_{64}]^{4+}\cdot(2O^{2-})$). (a) Structure of the cage framework. Extra-framework O^{2-} ions are neglected for simplicity. The black box shows a cubic unit cell with twelve cages. Two of the 12 cages encage one O^{2-} ion in each cage in the stoichiometric state. When each O^{2-} ion is replaced by two electrons, electron occupancy in the cage is 4/12. The cage has a large free space with 0.4 nm inner diameter. If a cage does not contain an ion, the cage forms a free-electron-like s orbital, as illustrated by the large spheres. (b) Expanded image showing three cages extracted from (a). A cage has an extra-framework oxide ion (illustrated as a light blue sphere). Six Ca ions (green spheres) form a part of the cage wall and two Ca ions coordinate to the encaged O^{2-} ion or to an empty cage center. Upon incorporating an O^{2-} ion, lattice relaxation is induced as indicated by the arrows: i.e., the ion-encaging cage shrinks, while the empty cages slightly expand.

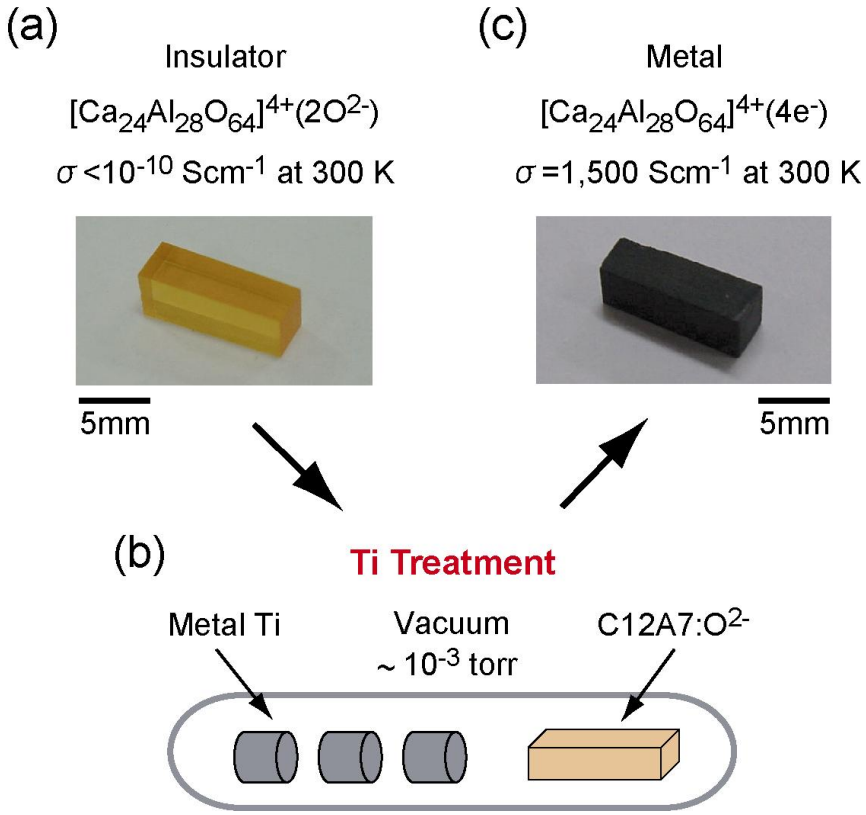

Figure 3-2. Conversion of insulating C12A7 to metallic C12A7. (a) Nominally undoped C12A7 is transparent with an orange tint due to the trace of Ir impurity incorporated from the Ir crucible during the CZ process. The sample is an insulator with a conductivity less than our detection limit (~10^{-10} S·cm^{-1}). (b) Extra-framework oxide ions in C12A7 are extracted by annealing with metal Ti powders at 900-1100 °C (Ti treatment). (c) Ti treatment turns the sample dark green and simultaneously increases electrical conductivity up to 1500 S·cm^{-1} at 300 K.

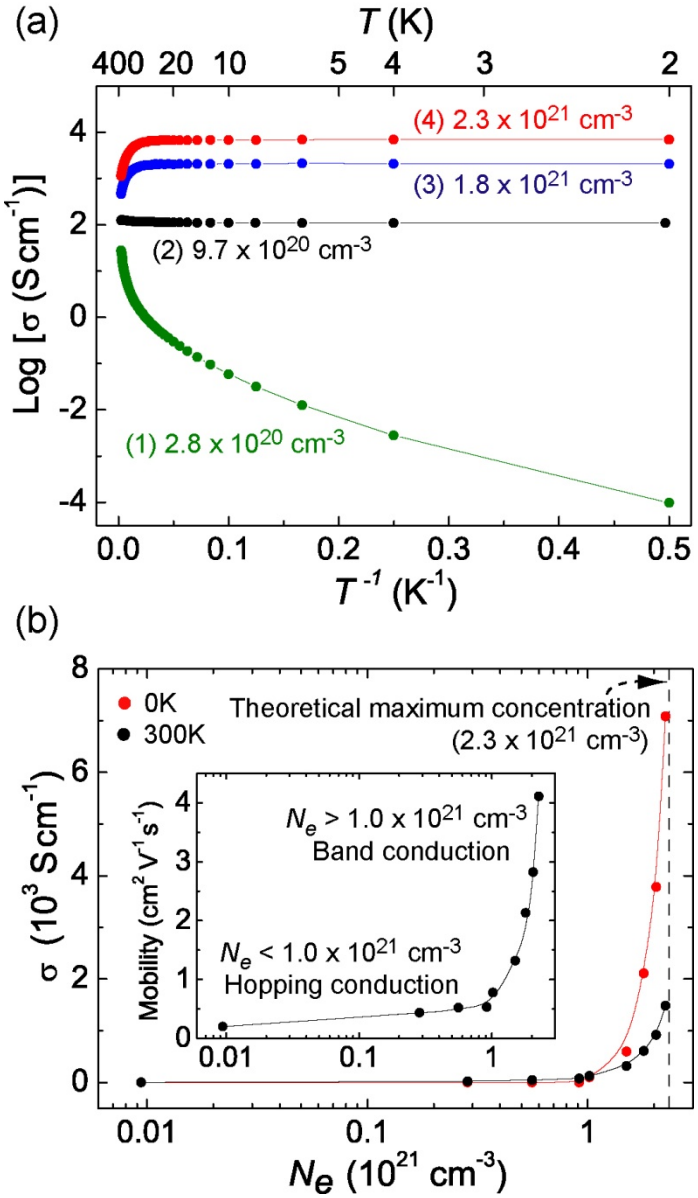

Figure 3-3. (a) Temperature dependence of conductivity (σ) for C12A7 single crystals treated for (1) 700°C, 24 h, (2) 900°C, 24 h, (3) 1000°C, 72 h, and (4) 1100°C, 24 h. The values in the figure denote electron concentrations. σ increases as the treatment temperature and duration increase. The most resistive sample (1) shows a thermally activated behavior, while the conduction type changes to degeneration at $N_e = N_{th} \sim 1 \times 10^{21}$ cm^{-3}, and finally to metallic at higher N_e. (b) The metal-insulator transition of C12A7. Electrical conductivities extrapolated to 0 K (σ_{0K}) are zero at $N_e < N_{th}$, but sharply increase as the carrier concentration increases at larger N_e. Electron mobilities at 300 K are low, 1 cm^2·V^{-1}·s^{-1} at $Ne < N_{th}$, but sharply increase at higher N_e.

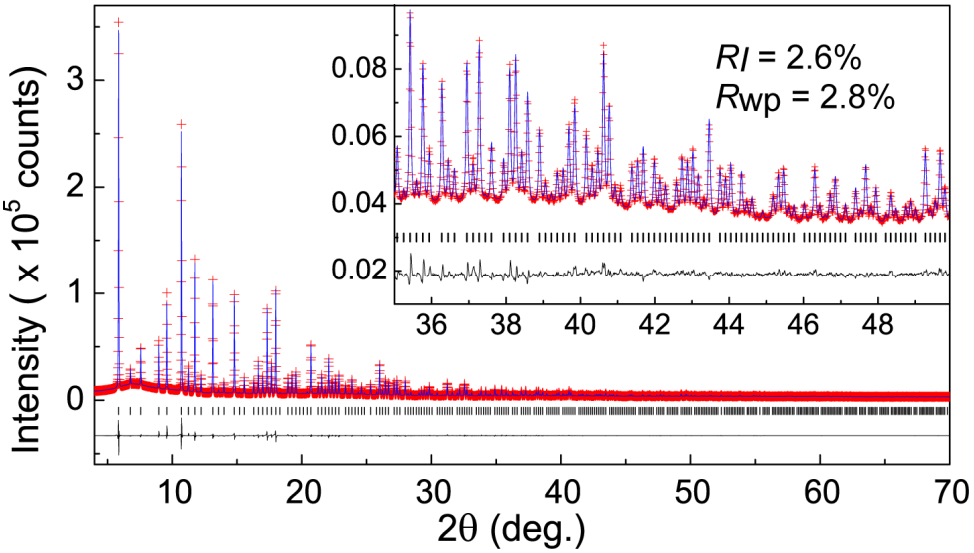

Figure 3-4. The final Rietveld fitting results for C12A7:e^-. Insets show magnified views from 35 to 50 degrees. The calculated reflection angles and the difference between the measured and calculated intensities are indicated on the lower side of graphs.

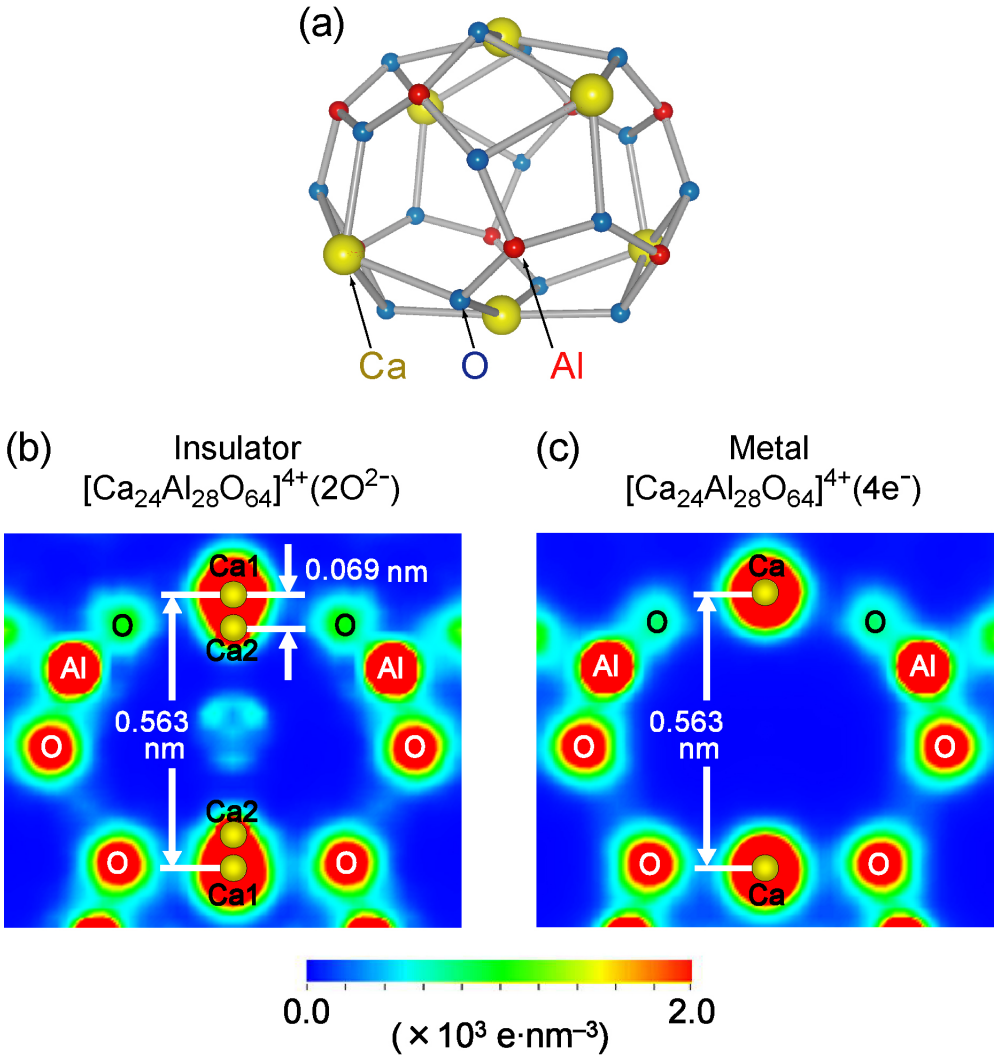

Figure 3-5. MEM electron density maps of C12A7. (a) An empty cage structure extracted from Fig. 3-1(a). The positions of the ions correspond to those in parts (b) and (c). (b) MEM electron density map at the (001) plane of insulating $[Ca_{24}Al_{28}O_{64}]^{4+}\cdot(2O^{2-})$ at 300 K (reproduced from the chapter 2). The electron densities of deformed (O^{2-}-incorporating) and undeformed (empty) cages are superimposed in the map, giving the teardrop-shaped densities of the Ca ions. (c) MEM electron density map of metallic $[Ca_{24}Al_{28}O_{64}]^{4+}\cdot(4e^{-})$ at 300 K. Ca–Ca distances are shown in the maps.

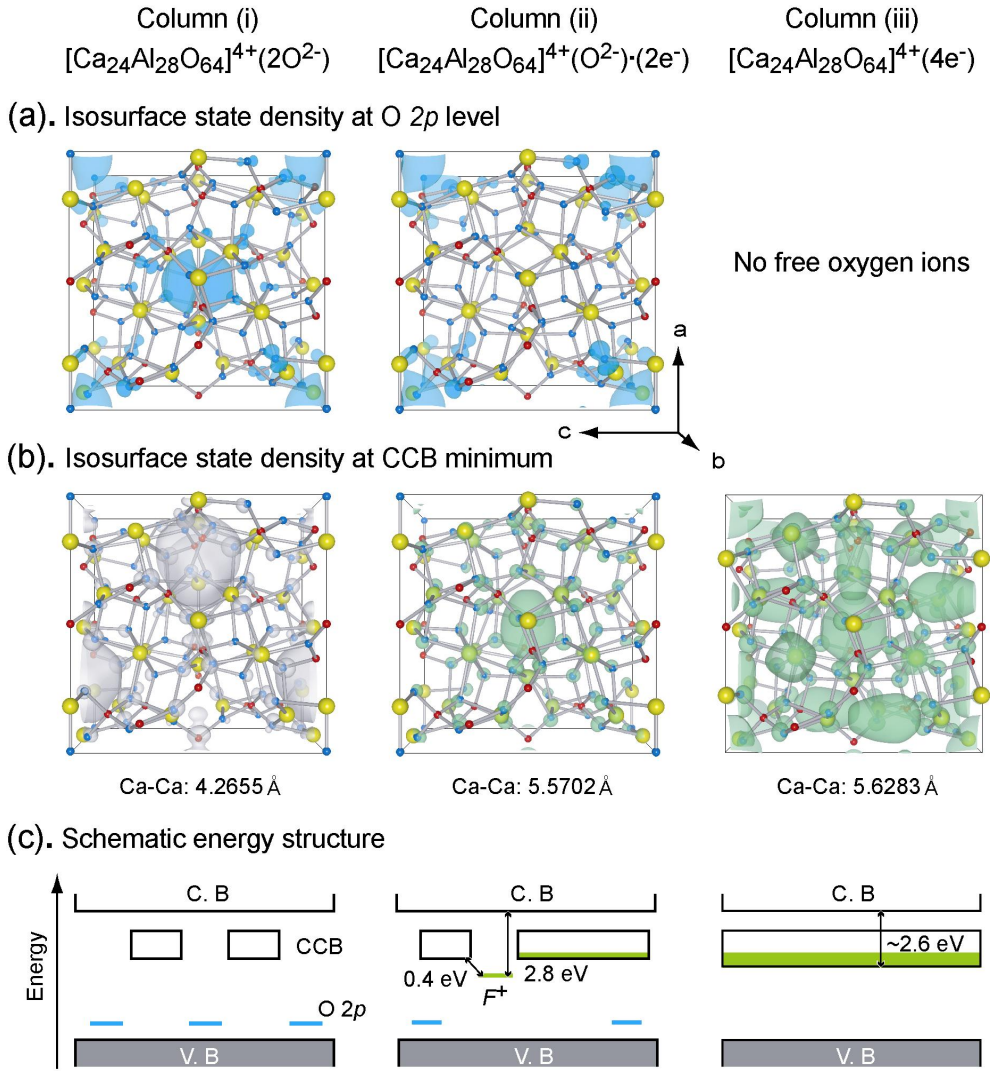

Figure 3-6. Relaxed lattice structures and electronic structures of C12A7 having three different electron concentrations: (i) stoichiometric $[Ca_{24}Al_{28}O_{64}]^{4+}\cdot(2O^{2-})$, (ii) $[Ca_{24}Al_{28}O_{64}]^{4+}\cdot(O^{2-})\cdot(2e^{-})$, and (iii) $[Ca_{24}Al_{28}O_{64}]^{4+}\cdot(4e^{-})$. (a,b) DFT isosurface state density of (a) the HOMO levels of the extra-framework O^{2-} ions and (b) the CCB bottom levels. Each box represents the unit cell. The blue and green color denotes the electron density maps for 2p electron of the extra-framework O^{2-} ions and the CCB electrons, respectively. The gray color denotes the s-like density of states in empty cages. The values of the isosurfaces are 5 e^{-}/nm^3 for (a(i)), (a(ii)), (b(i)), and (b(ii)), and 2.5 e^{-}/nm^3 for (b(iii)). (c) Schematic energy structures. Blue and green show the occupied levels of extra-framework O^{2-} ions and electrons in the cages, respectively.

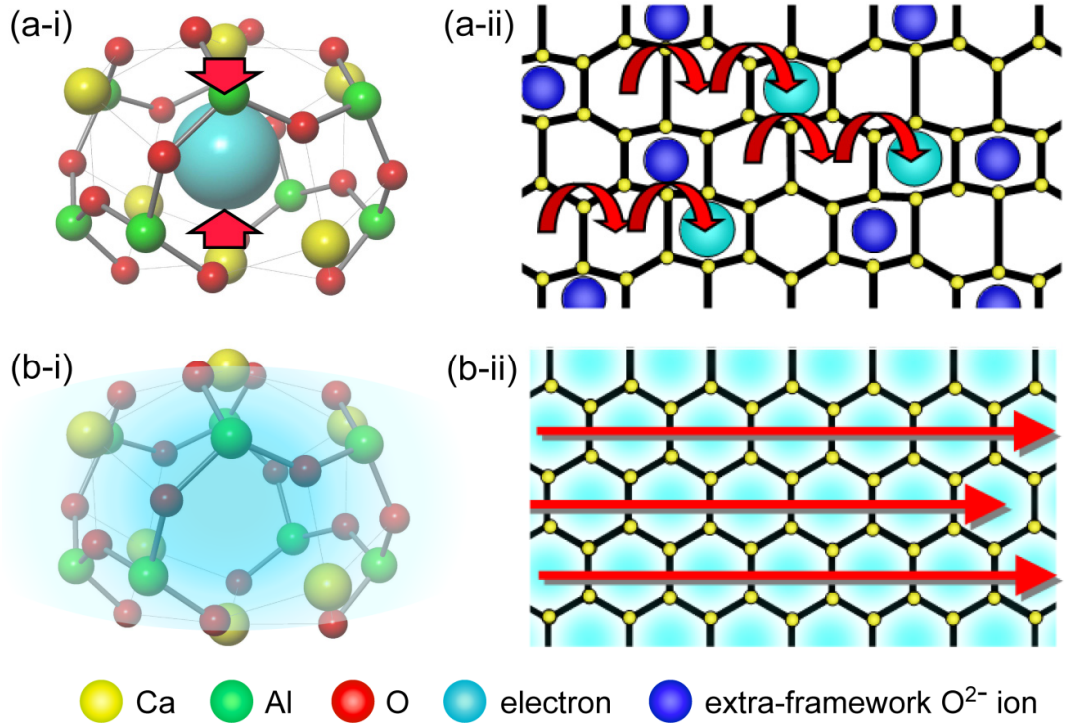

Figure 3-7. Schematics of the cage deformation and the conduction mechanism in C12A7 electride. (a-i) A localized electron and induced displacements of Ca ions. (a-ii) The hopping conduction in C12A7 electride at low electron concentration. Extra-framework O^{2-} ions and localized electrons induce the cage deformation, which modifies and inhomogenizes energy states of each cage. (b-i) Delocalized electron and deformation-released cage structure. (b-ii) The metallic (band) conduction in fully-electron-duped C12A7. The cage deformation was released and all the cages are homogenized into a same structure. Such the high symmetric structure would contribute the high mobility of fully-electron-doped C12A7.

Table 3-1. Comparison of crystal information for C12A7:O^{2-} and C12A7:e^- obtained from the final Rietveld analyses.

	C12A7:O^{2-}	C12A7:e^-
Composition formula	$C_{12}Al_{14}O_{33}$	$C_{12}Al_{14}O_{32}$
Structural formula	$[C_{24}Al_{28}O_{64}]^{4+}\cdot 2O^{2-}$	$[C_{24}Al_{28}O_{64}]^{4+}\cdot 4e^-$
Formula weight	2773.315	2741.317
Crystal system	cubic	cubic
Space group	$I\bar{4}3d$	$I\bar{4}3d$
Z	2	2
Lattice constant (nm)	1.198748(3)	1.200372(4)
Unit cell volume (nm^3)	1.7226	1.7165
Calculated density (g/cm)	2.673	2.632
Number of reflections	976	976
R_I	2.9	2.6
R_{wp}	2.9	2.8
Anion-induced Ca displacement (nm)	0.069	–

Table 3-2. Structural parameters of C12A7:e^- refined by the final Rietveld analysis.

	site	g	x	y	z	B (Å^2)
Ca1	24*d*	1	0.1404(1)	0	0.25	0.64(1)
Al1	16*c*	1	0.0176(1)	0.0176(1)	0.0176(1)	0.46(2)
Al2	12*b*	1	0.875	0	0.25	0.31(2)
O1	48*e*	1	0.1500(1)	0.9639(1)	0.0554(1)	0.76(3)
O2	16*c*	1	0.9359(1)	0.9359(1)	0.9359(1)	1.16(6)

Chapter 4: Crystallographic Phase Transition and High-T_c Superconductivity in LaFeAsO

4.1. Introduction

It is noteworthy that the stoichiometric (parent) materials of these Fe-based high-T_c superconductors do not exhibit any superconductivity, however, their resistivities and magnetic susceptibilities show anomalies at low temperature: In LaFeAsO, the temperature-dependent resistivity and magnetic susceptibility (ρ–T and χ–T) curves suddenly decrease at ~160 K (T_{anom}) (Fig. 4-2(a)) [1]. The anomaly can also observe in the specific heat measurements in this temperature range, although it looks contain two peaks at ~155 K and ~140 K [2]. They disappear by the carrier doping and coincidentally the superconducting states appear. On the other hand, no such anomalies have been observed in isostructural low-T_c superconductors including LaFePO (T_c ~4 K) [3], LaNiPO (T_c ~3 K) [4] and LaNiAsO (T_c ~2.4 K) [5], suggesting the phenomena are closely related to the high-T_c superconductivity. Therefore, to search the origins of the anomalies would be expected to clarify the appearance mechanism of the high-Tc superconductivity.

In this chapter, the low-temperature crystal structures, magnetic and conductive properties of parent and 14 at.% F-substituted LaFeAsO (T_c ~20 K) are examined by Rietveld refinements of synchrotron X-ray diffraction (XRD) data, DC magnetic measurements, and density functional theory (DFT) calculations. It is demonstrated that the parent LaFeAsO undergoes a crystallographic phase transition from the tetragonal (*P*4/*nmm*) phase to the orthorhombic (*Cmma*) phase at ~160 K. On the other hand, the F-substituted sample keeps the tetragonal symmetry down to 25 K, which suggests that the superconductivity occurs in the tetragonal phase. The results of the *ab initio* calculation suggest that the tetragonal-orthorhombic phase

transition stabilizes the stripe-type antiferromagnetic order on the Fe plane, which is consistent with the results of magnetic measurements such as neutron diffraction [6], nuclear magnetic resonance (NMR) [7], Mossbauer spectroscopy [8]. This transition can be attributable to the "Cooperative Jahn-Teller effect", and such the magnetic interaction would induce spin fluctuation as observed in the magnetic measurement of the F-substituted LaFeAsO, leading the high-T_c superconductivity.

4.2. Experimental and Calculation

4.2.1. Sample Preparation

The target compounds were synthesized by solid state reactions using a powder of dehydrated La_2O_3 (i) and a mixture powder of LaAs, Fe_2As, and FeAs (ii) as starting materials in a sealed silica tube. The dehydrated La_2O_3 power (i) was obtained by heating commercial La_2O_3 powders at 600°C for 10 h in air for removal of adsorbed water. To prepare the mixture powder of (ii), metal La, metal Fe, and metallic As were mixed in a ratio of 1 : 3 : 3 and put it into a silica tube in a glove box filled with a dry Ar gas. They were sealed under pumping and subsequently heated at 850°C for 10 h. Since the vapor pressure of elementary As is rather high above 600°C, the synthesis of the As-compounds as the precursor is required to avoid the possible explosion of the sealed silica ample during the main reactions. A selection of the silica tube material durable for the high temperatures and water free environment were important factors to avoid the explosion. Then, a 1 : 1 mixture of the powder of (i) and (ii) was pressed by ~10 MPa pressure to prepare pellets with 7 mm diameter × 5 mm thick or 7 mm × 10 mm × 10 mm. The pellet was placed in a silica tube, and sealed with 0.02 MPa Ar gas at room temperature. The sealed silica tube was heated at 1250°C for 40 h to synthesize parent LaFeAsO. The Ar gas filling was effective to prevent collapse of the silica tube during this heating process.

For F-substitution, a part of La_2O_3 was replaced with a 1 : 1 mixture of LaF_3 and La metal in the starting materials for parent LaFeAsO. The F concentration of the F-substituted sample was estimated as ~14% from the lattice constants of samples, which decreases systematically obeying the volume Vegard's rule [1,9].

4.2.2. Erectrical and Magnetic Measurements

Electrical resistivity measurements with a DC four-probe technique were conducted at 1.9–300 K using a Quantum Design physical properties measurement system (PPMS). The sintered samples were cut into cuboids with ~2 mm × ~2 mm × ~10 mm and an array of four platinum or gold band electrodes was deposited on each sample with equal interval by using an ion sputtering device. The sample was mounted on a sample holder for the resistivity measurement and the electrodes were connected to measurement proves by platinum paste. For the temperature-dependent resistivity measurements (ρ-*T*), the measurement interval was every 0.5 K step and the heating and cooling rates were 5 K per minute.

The magnetization was measured using the PPMS with a vibrating sample magnetometer (VSM) option under an external magnetic field up to 2 T at 1.9–300 K. The sintered samples were cut into ~a few ten mg of cubic peaces and adhered to a cylindrical sample holder for VSM by using insulating varnish. For the measurements of temperature-dependent magnetic susceptibility (χ-*T*), the measurement interval was every 0.5 K step and the heating and cooling rates were 5 K per minute. For the magnetization measurements as a function of magnetic field (χ-*H*), the change rate of magnetic field was 100 Oe per second.

4.2.3. XRD Measurements and Rietveld Analysis

Optical microscope observations clarified that the sintered samples were composed of

multi-grains with a maximum size of ~10 μm and some of the grains were seemingly single crystals, with an apparently orientation of the *c*-plane parallel to the sample surface. Routine X-ray diffraction measurements were performed using Bruker D8 Advance TXS with Cu Kα radiation from a rotary cathode, where the crushed powder with a particle size of ~10 μm was employed. The obtained XRD spectra prefer to orient along c-axis direction, which would originate from the layered character of LaFeAsO.

The high-resolution synchrotron XRD measurements at various temperatures were conducted at the BL02B2 beamline in the SPring-8 Japan. The sintered samples were ground, then packed and sealed in Lindemann glass capillaries with an inside diameter of 0.3 mm. The capillary was set at a sample stage of a large Debye-Scherrer camera with a 286.48 mm camera radius [10]. The monochromatic X-ray wavelength was ~0.05 nm and two-dimensional Debye-Scherrer images were detected by Imaging Plates. For measurements at low temperatures, the capillaries were cooled using a dry N_2 or He gas-flow cooling device. Temperatures of the gases were measured and calibrated them to the sample temperature. Diffraction data were collected at 300, 270, 200, 175, 145, 120 and 93 K for 25 minutes (N_2 gas cooling) and at 25 K for 75 minutes (He gas cooling) in each sample. In addition, the low temperature measurements ranging from 185 K to 135 K by 5 K for 5 minutes were conducted for parent LaFeAsO to examine the detailed crystallographic changes at around T_{anom}.

To perform Rietveld analysis, the diffraction data ranging from 4 to 73° (N_2 gas cooling) or to 53° (He gas cooling) with a 0.01° step in 2θ were employed, which corresponds to 0.042 nm and 0.056 nm resolution, respectively. The reason why the high-angle range was restricted in the He gas cooling is that the diffracted X-ray is interrupted by the cooling devises. The weak extrinsic peaks, identified as FeAs, La_2O_3, and $La(OH)_3$ for the parent sample, FeAs, LaAs, and LaOF for the F-substituted sample, were also fitted as impurity phases in the analyses.

4.2.4. Ab Initio Calculations

The Density functional theory (DFT) was implemented in the computer code VASP [11], where the generalized gradient approximation (GGA) suggested by Perdew *et al.* (PW91) [12] and the projected augmented waves (PAW) method [13] were used. The cutoff energy of plane-wave basis set was 600 eV. Supercells containing 8, 16, and 32 atoms were considered and the tested meshes containing 252, 132, and 36 *k*-points, respectively, were used for Brillouin zone integrations. The total energy was minimized with respect to the coordinates of all atoms. For the analysis of the electronic structure, the charge density was decomposed over the atom-centered spherical harmonics. To investigate the stabilities of the magnetic structures in parent LaFeAsO, the total energy was minimized with respect to internal coordinates and lattice cell parameters for two spin configurations, stripe and checker board ones.

4.3. Results and discussion

4.3.1. Electrical and Magnetic Measurements

As reported previously [1], parent samples exhibit an abrupt decrease in the resistivity at around 160 K (T_{anom}) as shown in Fig. 4-2(a), but do not exhibit the superconducting transition down to 1.8 K. The magnetization (M) at a fixed magnetic field (H) of 1 T decreased gradually with lowering temperature from room temperature; the temperature dependence exhibited opposite behavior to that of conventional Pauli paramagnetism, typically observed in transition-metal elements and FeSi [14–16]. With lowering of the temperature, an additional stepwise decrease was observed at 160 to 140 K. With further decreasing temperature below 140 K, the M value grows gradually and then sharply increases below ~25 K. As shown in Fig. 4-2(b), the M–H curves above 25 K are almost straight whereas nonlinearity starts to appear at

10 K and becomes prominent at 1.9 K (Fig. 4-2(b)). The magnetic moment at $H = 0$ can be estimated to be ~4 emu/LaFeAsO or ~7×10^{-5} μB/Fe if one assumes the linear dependence of M on H in the H region of 1.5–2 T, but its origin remains unclear. The presence of magnetic impurity phases, such as FeAs, is a possible origin. The contents of impurity phases estimated from the Rietveld analysis are shown in caption of Fig. 4-5.

The anomaly at ~160 K in ρ-T and M-T curves disappears in the 14% F-substituted LaFeAsO (Fig. 4-2(c)), which undergoes a superconducting transition at ~20 K. The M value becomes negative in the superconducting state due to the Meissner effect. With increasing temperature it jumps to a fairly large value at a temperature just above T_c, and then decreases monotonically with further increase of T although it weakly increases again above 150 K. The M–H curves in the normal conducting state exhibit a straight line in the high-H region and they deviate a little down side from the line in the low-H region (Fig. 4-2(d)). Figure 4-2(e) summarizes the temperature-dependent magnetic susceptibilities of $LaFeAsO_{1-x}F_x$ with several x values. The comparison of the curves enables us to separate the temperature-sensitive Curie–Weiss-like (CW-like) component from the temperature-insensitive baseline in each sample. It is noteworthy that the CW-like component increases with the F content up to 5% and then decreases with further increase in the F content. This tendency is more clearly demonstrated in Fig. 4-2(f), where the χ values at 50, 100 and 300 K are plotted against the value of x. It is, however, unlikely that this tendency is totally due to the magnetic impurity phases, such as FeAs, because the content of the dominant magnetic impurity phase of FeAs was observed to vary slightly with the F content. This tendency is not consistent with the almost constant value of T_c ~26 K over the F content of 5–11% [1]. In other words, the χ value does not correlate with the generation of the superconductivity, provided that the contribution of the impurity phases to the observed χ value is small.

4.3.2. Crystallographic Analysis

All the diffraction peaks of the parent sample at temperatures above T_{anom} were consistently assigned to the conventional ZrCuSiAs-type tetragonal phase (*P*4/*nmm*) [17], except for the additional weak peaks assigned to impurity phases (see below). However, at low temperature, several peaks including the 110, 111, 112, 211 and 322 reflections of the tetragonal phase start to broaden at around 170 K, and they clearly split into two peaks below 160 K (Fig. 4-3). On the other hand, such splitting was never observed in the diffraction peaks for the 14% F-substituted sample down to 25 K.

These XRD patterns were analyzed by Rietveld analysis to refine the crystal structures of these samples. The fitting results and the refined structure parameters are shown in Fig. 4-4 and tables 4-1 and 4-2. The XRD patterns of F-substituted sample were well fit with the tetragonal *P*4/*nmm* space group over the temperature range. For the parent LaFeAsO, the patterns measured above 165 K were also fit with the tetragonal symmetry; however, the symmetry should be lowered for the patterns measured below 160 K to fit the doublet peaks consistently. The analysis led us to the conclusion that the anomaly is associated with the crystallographic phase transition from the tetragonal to orthorhombic phase. The orthorhombic *Cmma* space group provided the smallest R_I and R_{wp} value of ~2.0% and ~4.6% for the data of 120 K. Figure 4-5 shows ~20 times magnified XRD patterns of the parent and 14% F-substituted LaFeAsO. There were several weak peaks which are assigned as those of impurity phases including FeAs, La_2O_3, and $La(OH)_3$ for the parent sample, and FeAs, LaAs and LaOF for the F-substituted sample. (Each estimated content of impurities was below 5 wt.% as described in the figure caption). These impurities would not affect any significant effects on the analysis results.

As a result of the transition, the *a*- and *b*-axes were rotated by 45° along *c*-direction

relative to those of tetragonal phase and the lattice constants expand by a multiple of √2 although the axis lengths are no longer unequal (Fig. 4-1(b)). The number of the formula units (Z) increases from 2 to 4 by the change of the unit cell. The symmetry of *Cmma* space group is obtained only by removing the confinement of "$a = b$" from the symmetry of *P*4/*nmm* with keeping the other symmetry elements, therefore, the number of each atomic sites does not change before and after the transition. Cruz *et al.* have reported the structure phase transition of parent LaFeAsO from the result of the neutron diffraction measurement, but they assigned the monoclinic *P*112/*n* space group to the low-temperature phase [6]. I checked the fitting results with the orthorhombic *Cmma* space group, but any peaks violating the extinction rule have not been found in the diffraction patterns down to 25 K. The structural studies of other *Ln*FeAsO structures, such as CeFeAsO, NdFeAsO and SmFeAsO [18–21], have also reported that the crystal symmetry of the low-temperature phase can be successfully assigned to the *Cmma* space group, citing our report. These results support my determination of the space group for the low-temperature phase.

The lattice constants of the parent and the F-substituted LaFeAsO obtained by the Rietveld analysis are shown as a function of temperature in Fig. 4-6. In the parent sample, the *a*-axis length starts to split at ~160 K which corresponds to the temperature the resistivity anomaly occurs (T_{anom}) and is higher than the magnetic transition temperature (ca. 140 K) observed by other measurements [6–8]. The difference between *a*- and *b*-axis lengths gradually increases at lower temperatures, reaching to ~0.5% at 120 K. Additionally, the *a*- and *c*-axis lengths show hysteretic behavior in the heating and the cooling processes above T_{anom}, which may implies the remnants of the structural distortion of the low-*T* phase. In contrast, the F-substituted sample maintains the tetragonal symmetry down to 25 K. The *a*- and *c*-axis lengths shrink by ~0.2 and ~0.5% with cooling the sample from 300 to 25 K. Such anisotropic

compressibility would be caused by the layered structure of the material. On the other hand, the F substitution reduces the *a*- and *c*-axis lengths by ~0.25 and ~0.45% at room temperature. The reduction of *a*-axis length indicates the decrease of the Fe–Fe distance, which enhances the interaction among 3d electrons.

The La–O, La–As and Fe–As bond lengths are shown in Fig. 4-7 for parent and 14% F-substituted samples as a function of *T*. All the bond lengths decrease as temperature decreases, but the bond lengths of parent samples undergo abrupt changes due to the phase transition at around T_{anom}. Further, it is noteworthy that, with the F substitution, the Fe–As bond length changes only slightly (less than 0.1%), whereas, the La–O distance comparatively increases by ~0.8%. These results indicate that the F substitution does not affect the geometry of the FeAs layer, in contrast to the significant monition for the LaO layer. On the other hand, the La–As bond distance exhibited a large reduction of ~1.3%, which corresponds to a decrease in the distance between the LaO and FeAs layers. The decrease would be attributed to the enhancement of charge polarizations between the layers due to the electron transfer from the LaO to FeAs layers by the F substitution.

Figure 4-8 shows the temperature dependency of the O–La–O and As–Fe–As bond angles for the parent and F-substituted samples. The results demonstrated that both angles are essentially insensitive to temperature. The bond angle of the La_4O tetrahedron in the parent LaFeAsO (~117°) was deviated from the regular tetrahedron angle (i.e. 109.5°), however, the distortion was significantly relaxed in the F-substituted sample (~115°). On the other hand, the $FeAs_4$ tetrahedron hardly changes the shape before and after the F substitution (~113.5°), which suggests that elemental substitution for the blocking layer could introduce conductive carriers to FeAs layer without structural change of the FeAs layer. Lee *et al.* have suggested that the magnitude of the distortion of the $FeAs_4$ tetrahedron is a good measure of T_c [22]. Thus, our and

their results lead to a conclusion that parent compounds with a highly symmetric $FeAs_4$ tetrahedron have the potential to be higher-T_c superconductors by the substitution for the blocking layer.

4.3.3. Ab Initio Calculations

To achieve further insight into the relation between the chemical composition, structure, magnetic properties and the superconductivity mechanism, *ab initio* calculations of both parent and F-substituted LaFeAsO were carried out using DFT and the PW91 density functional. The calculation results suggest that the charge density distribution across the layers has $(LaO)^{+\delta}(FeAs)^{-\delta}$ character with $\delta = 0.15|e|$ per molecule. The density of states (DOS) near the Fermi energy is dominated by Fe3d states with about 10% contribution of As4p states. The total energy of the system depends on the configuration of the spins associated with Fe 3d electrons, therefore, the total energies for four non-equivalent spin configurations within the 16-atom $\sqrt{2}\times\sqrt{2}$ supercell was calculated: ferromagnetic (FM), and three antiferromagnetic (AF1, AF2a, AF2b) ones, where AF2a and AF2b are equivalent (see Fig. 4-9). For the lattice parameters and internal coordinates of the orthorhombic (**O**) phase determined both experimentally and theoretically using the PW91 density functional, it was found that EFM > EAF1 > EAF2a = EAF2b and that the relative energies of these configurations with respect to AF2a are 0.15 eV for AF1 and 0.40 eV for FM.

By minimizing the total energies with respect to the atomic positions as well as the lattice parameters, the **O** structure has lattice parameter values a, b and c of 0.567, 0.573 and 0.869 nm, respectively, so $a > b$ for AF2a and $a < b$ for AF2b. In the AF2 configuration, the Fe 3d spins along the short Fe–Fe bonds have parallel orientation and those along the long Fe–Fe bond have antiparallel orientation. In contrast, the AF1 configuration relaxes to the tetragonal (**T**) structure

with $a = b = 0.569$ nm and $c = 0.862$ nm and remains by 0.15 eV less stable than AF2. The FM configuration becomes unstable and converges to AF1.

I note that the relative energies of the spin configurations are expected to depend on the accuracy of the exchange–correlation functional, which needs to be investigated separately. The effect of the **T**–**O** transition on the electronic structure of LaFeAsO was analyzed. Figure 4-10 shows the DOSs calculated using the PW91 functional near the Fermi level for the AF1 (**T**-phase) and AF2 (**O**-phase) configurations. It is clearly seen that the magnitude of the DOS near the Fermi energy is large in the AF1 configuration (**T**-phase). However, it transforms into a wide depression in the AF2 configuration (**O**-phase). It should be noted that the DOS structure is mostly determined by the spin configuration rather than by the details of the atomic structure.

Integrating the PW91 spin density within the sphere near each Fe atom suggests that the magnetic moment per Fe in the AF2 configuration is ~1.6 μB. The densities of spin-up and spin-down electrons are almost equivalent, so the total magnetic moment per 16-atom supercell is about 4×10^{-3} μB and $\sim 10^{-3}$ μB for the **T** and **O** structures, respectively. Although these numbers are too small to be determined accurately with DFT, they indicate that: (i) the total magnetization of FeAs layers is small, and (ii) the total magnetic moment reduces during the **T**–**O** transition.

4.3.4. Phenomenological Model for Phase Transitions

Figure 4-11 shows a schematic representation of the potential energy surfaces (PESs) calculated for parent LaFeAsO and plotted with respect to the lattice parameters of the *Cmma* space group. The PES curves are calculated for two types of antiferromagnetic configuration, the checkerboard (AF1) and spin stripe type (AF2), and the latter is the more stable one, in agreement with the experimental observation [18]. The AF2 PES is represented by two

equivalent parabolic curves with the minima at **O**1 ($a < b$ region) and **O**2 ($a > b$ region). The two curves split at the crossing point into upper (AF2U) and lower (AF2L) branches due to anharmonic electron–phonon interaction (tunneling interaction). The lower branch has a double minimum structure and, at low temperature (the $T1$ region in Fig. 4-11(b)), the system is stabilized at one of the minima. This indicates that the orthorhombic phase is stable at low temperatures. The spins on Fe atoms along short Fe–Fe bonds couple ferromagnetically in the AF2L branch and antiferromagnetically in the AF2U branch, suggesting that the magnetostrictive interaction plays a major role in stabilizing the orthorhombic structure. On increasing the temperature (the $T2$ region in Fig. 4-11(b)), the system migrates dynamically between the two minima due to the thermal energy, inducing the transition from the **O** to **T** phase. The calculated double minima most likely arise from both the existence of degenerate states at the Fermi level (the energy band structure indicates that the two branches of the Fe 3d orbital are quasi-degenerate at the Γ points) and the magnetostrictive interaction between the Fe spins, which can be interpreted as the occurrence of a cooperative Jahn-Teller effect [23,24].

In the reductively F-substituted $LaFeAsO_{1-x}F_x$, F^- ions substitute lattice O^{2-} ions. This induces three main effects. First, the substitution provides additional electrons to the FeAs layer and changes the calculated charge density distribution to $(LaO)^{+\delta+x}(FeAs)^{-\delta-x}$ in all considered cases (x = 0.5, 0.25, 0.125). The increased interlayer ionic bonding manifests itself in the shortening of the lattice vector along the c-axis, observed experimentally, and in the opening of a narrow gap at ~2.5 eV below the Fermi energy separating predominantly p and d states of the FeAs layers.

Second, the Fe magnetic moments decrease to ~1.3 μB for x = 0.125 and to below ~0.1 μB for x = 0.25. Interestingly, it was found that F substitution induces strong perturbation in the spin density distribution. In particular, in the x = 0.25 case, the spin-down 3d density is localized

on a single Fe atom closest to the F-based impurity, while the remaining three Fe atoms share the spin-up density. However, at a more realistic doping level (x = 0.125), the character of the spin distribution is much more complex: the spin density is predominantly antiferromagnetic but the local magnetic moments associated with Fe atoms become essentially disordered. Thus, it was suggested that the F substitution induces a strong perturbation and may destroy the antiferromagnetic spin ordering.

Finally, relaxing the lattice parameters for the F-substituted systems, it was found that they have tetragonal structures. For example, the relaxed 16-atom supercell (x = 0.25) has tetragonal lattice structure with $a = b$ = 0.569 nm, and c = 0.849 nm. This indicates that the F substitution reduces the strength of magnetostrictive interaction and suppresses the transition into the orthorhombic phase.

The calculated DOS for the AF1 state shows a pronounced depression in the DOS of both tetragonal and orthorhombic LaFeAsO at the Fermi energy. However, the F substitution shifts the Fermi energy so that it is at the local DOS peak for x = 0.125, which agrees well with the optimal doping level of x = 0.11 found experimentally for this material. This DOS peak is formed predominantly by d(xz) and d(yz) states, which couple the interaction between the Fe atoms in the Fe sheet with the Fe–As interaction across the FeAs layer. As the doping level increases to x = 0.25, the value of the DOS at the Fermi energy decreases again.

Finally, it should be noted that the AF1 DOS in the parent tetragonal and orthorhombic phases of LaFeAsO are virtually undistinguishable from each other, but they are very different from those found for AF2. This suggests that the effect of the structural change due to the phase transition alone is much smaller than the effects induced by the reorientation of Fe 3d spins. The latter are strongly affected by doping, which includes interrelated geometric, electronic and spin structure changes. In particular, the interaction between the LaO and FeAs layers increases, the

Fermi level shifts to higher energies, and the DOS increases at the Fermi level.

F substitution increases the electron density within the FeAs layers and the magnetic moments associated with the Fe atoms decrease as the doping level increases, thus further decreasing the propensity of forming the orthorhombic structure.

4.4. Conclusion

The crystal structures of the parent (unsubsituted) and 14% F-substituted LaFeAsO at low temperature were investigated. Some diffraction peaks of the parent samples were split into doublet below ~160 K. The Rietveld analysis demonstrated that the parent LaFeAsO, belonging to tetragonal (*P*4/*nmm*) symmetry at room temperature, transforms to orthorhombic (*Cmma*) phases below 160 K. The transition temperature agrees with the temperature where the resistivity suddenly decreases (T_{anom}), which indicates the structure transition is the origin of the resistivity anomaly. On the other hand, F-substituted sample keeps the tetragonal symmetry down to at least 25 K, which suggests that carrier doping suppresses the structural transition and induces the superconductivity. The spin configurations in the orthorhombic LaFeAsO were calculated by DFT methods. The results demonstrate that stripe-type antiferromagnetic order of Fe is energetically stable at orthorhombic structure. The deduced double minimum potential arranged with the *a*- and *b*-axis length can elucidate the mechanism of the structure and magnetic phase transitions. The calculation results indicate that the antiferromagnetic order is strongly related with the orthorhombic structure, therefore, the magnetic fluctuation inducing the superconductivity would also accompany the structural deformation.

References

[1] Y. Kamihara, T. Watanabe, M. Hirano and H. Hosono, J. Am. Chem. Soc. **130**, 3296 (2008).

[2] Y. Kohama, Y. Kamihara, M. Hirano, H. Kawaji, T. Atake and H. Hosono, Phys. Rev. B 78, 020512(R) (2008).

[3] Y. Kamihara, T. Watanabe, M. Hirano and H. Hosono, J. Am. Chem. Soc., **130**, 3296 (2008).

[4] T. Watanabe, H. Yanagi, T. Kamiya, Y. Kamihara, H. Hiramatsu, M. Hirano and H. Hosono, Inorg. Chem. **46**, 7719 (2007).

[5] T. Watanabe, H. Yanagi, Y. Kamihara, T. Kamiya, M. Hirano, H. Hosono, J. Sol. State Chem. **181** 2117 (2008).

[6] C. de la Cruz, Q. Huang, J. W. Lynn, J. Li, W. Ratcliff, j. L. Zarestky, H. A. Mook, G. F. Chen, J. L. Luo, N. L. Wang and P. Dai, Nature, **453**, 899 (2008).

[7] Y. Nakai, K. Ishida, Y. Kamihara, M. Hirano and H. Hosono, J. Phys. Soc. Jpn. **77**, 073701 (2008).

[8] S. Kitao, Y. Kobayashi, S. Higashitaniguchi, M. Saito, Y. Kamihara, M. Hirano, T. Mitsui, H. Hosono and M. Seto, J. Phys. Soc. Jpn. **77**, 103706 (2008).

[9] S. W. Kim, Y. Kamihara, S. G. Yoon, H. S. Han, T. Nomura, S. Matsuishi, K. Nakao, K. Tanabe, M. Hirano and H. Hosono, J. Phys. Soc. Jpn. Suppl. C **77**, 23 (2008).

[10] E. Nishibori, M. Takata, K. Kato, M. Sakata, Y. Kubota, S. Aoyagi, Y. Kuroiwa, M. Yamakata and N. Ikeda; Nucl. Instrum. Methods A **467/468**, 1045 (2001).

[11] G. Kresse and J. Furthmuller; Phys. Rev. B **54**, 11169 (1996).

[12] J. P. Perdew and Y. Wang, Phys. Rev. B **46**, 12947 (1992).

[13] P. E. Blochl, Phys. Rev. B **50**, 17953 (1994).

[14] C. J. Kriessman and H. B. Callen, Phys. Rev. **94**, 837 (1954).

[15] V. Jaccarino, G. K. Werthein, J. H. Wernick, L. R. Walker and S. Arajs; Phys. Rev. **160**, 476 (1967).

[16] Y. Takahashi, J. Phys. Soc. Jpn. **55**, 3553 (1986).

[17] B. I. Zimmer, W. Jeitschko, J. H. Albering, R. Glaum and M. Reehuis, J. Alloys Compounds **229**, 238 (1995).

[18] J. Zhao, Q. Huang, C. de la Cruz, S. Li, J. W. Lynn, Y. Chen, M. A. Green, G. F. Chen, G. Li, Z. Li, J. L. Luo, N. L. Wang and P. Dai, Nature Mater. **7**, 953 (2008).

[19] M. Fratini, R. Caivano, A. Puri, A. Ricci, Z.-A. Ren, X. L. Dong, J. Yang, W. Lu, Z. X. Zhao, L. Barba, G. Arrighetti, M. Polentarutti and A. Bianconi, Supercond. Sci. Technol. **21**, 092002 (2008).

[20] S. Margadonna, Y. Takabayashi, M. T. McDonald, M. Brunelli, G. Wu, R. H. Liu, X. H.

Chen and K. Prassides, Phys. Rev. B **79**, 014503 (2009).
[21] A. Martinelli, A. Palenzona, C. Ferdeghini, M. Putti and E. Emerich; arXiv:0808.1024.
[22] C. H. Lee, A. Iyo, H. Eisaki, H. Kito, M. T. Fernandez-Diaz, T. Ito, K. Kihou, H. Matsuhata, M. Braden and K. Yamada; J. Phys. Soc. Jpn. 77, 083704 (2008).
[23] G. A. Gehring and K. A. Gehring, Rep. Prog. Phys. **38**, 189 (1975).
[24] J. A. Krumhansl and J. R. Schieffer, Phys. Rev. B **11** 3535 (1975).

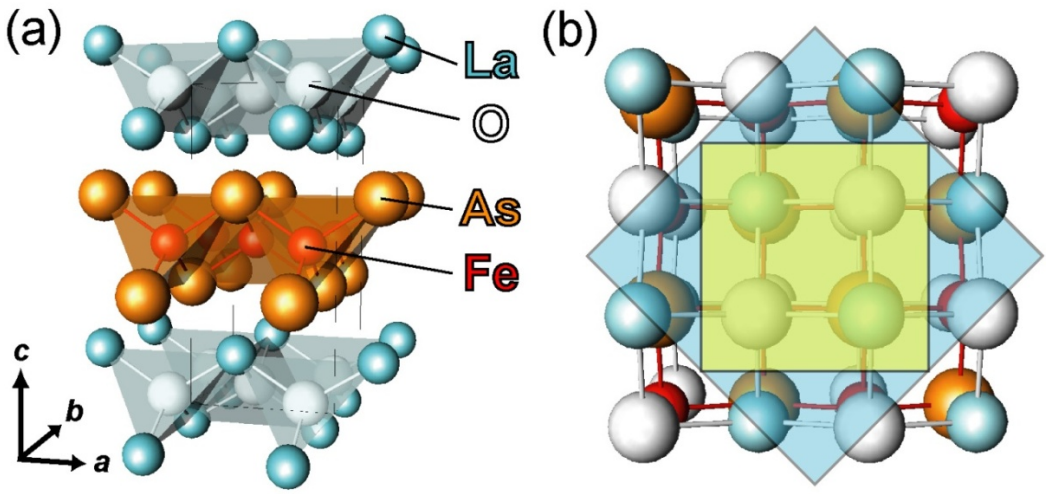

Figure 4-1. Crystal structure of LaFeAsO. (a) Schematic view of the crystal structure, demonstrating the layered structure. Distorted tetrahedrons of $FeAs_4$ are connected in an edge-sharing manner to form the FeAs layer. (b) Top view of the crystal structure from the *c*-direction. The inner square represents the unit cell in the tetragonal phase (*P*4/*nmm*). The outer square is that in the orthorhombic phase (*Cmma*). The unit cell of the orthorhombic phase rotates by 45° from that of the tetragonal phase and the lattice constants expands by $\sqrt{2}$, resulting in an increase in the number of chemical formula units in a unit cell from 2 to 4.

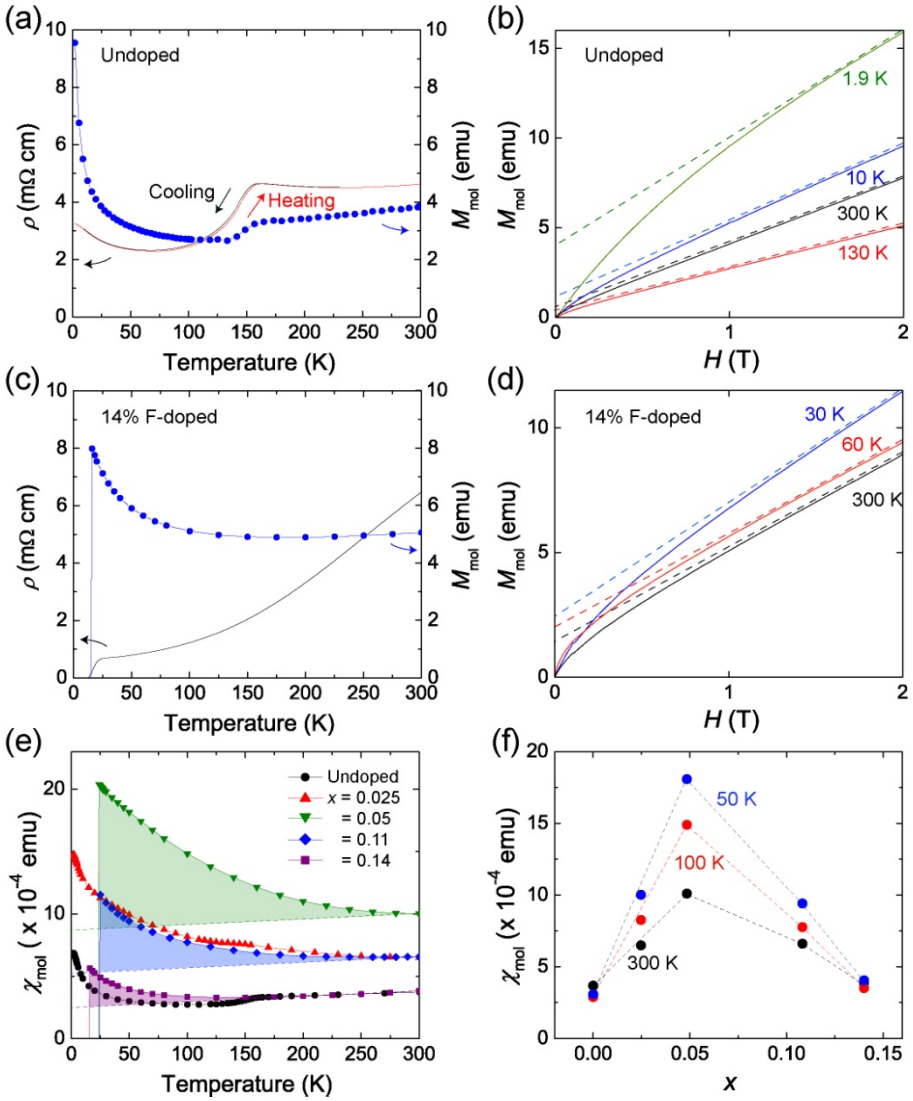

Figure 4-2. Electrical and magnetic properties of parent and F-substituted LaFeAsO. (a) Electrical resistivity (ρ) and magnetization per mol (M_{mol}) at a fixed magnetic field of 1 T as a function of temperature (T) for parent LaFeAsO. (b) M_{mol} as a function of magnetic field (H) for parent LaFeAsO. (c) ρ and M_{mol} at a fixed H of 1 T as a function of T for 14% F-substituted LaFeAsO. (d) M_{mol} as a function of H for 14% F-substituted LaFeAsO. (e) Magnetic susceptibility (χ_{mol}) as a function of T in various F-substituted LaFeAsO samples. Dotted lines represent estimated Pauli paramagnetic components, whereas dashed areas correspond to Curie–Weiss-like components. (f) Magnetic susceptibility (χ_{mol}) as a function of F content (x) in LaFeAsO for several temperatures.

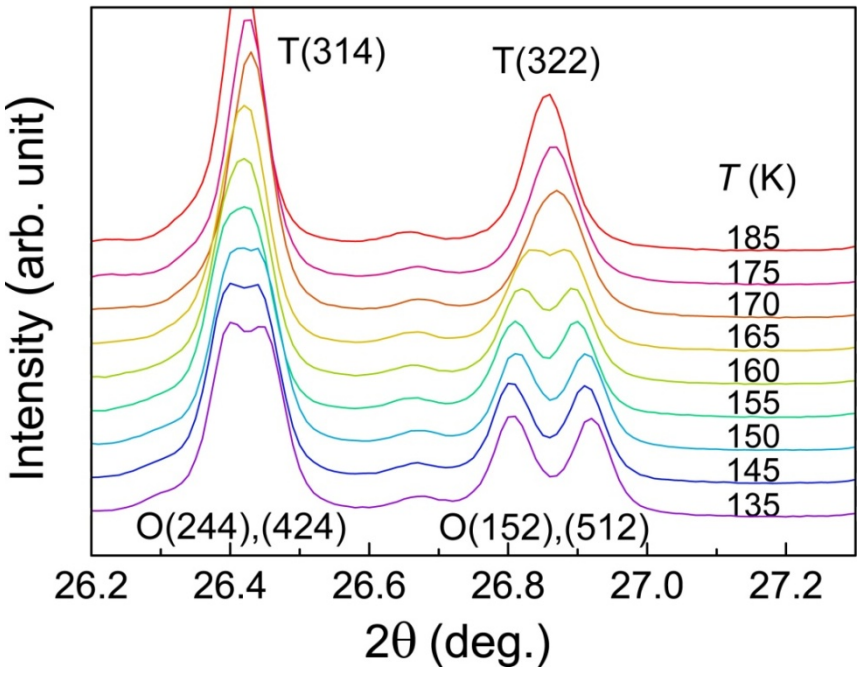

Figure 4-3. Diffraction profiles of tetragonal 314 and 322 reflections of undpoed LaFeAsO for several temperatures from 135 K to 185 K. The split peaks below 165 K are indexed as 244, 424 and 152, 512 in the orthorhombic symmetry, respectively

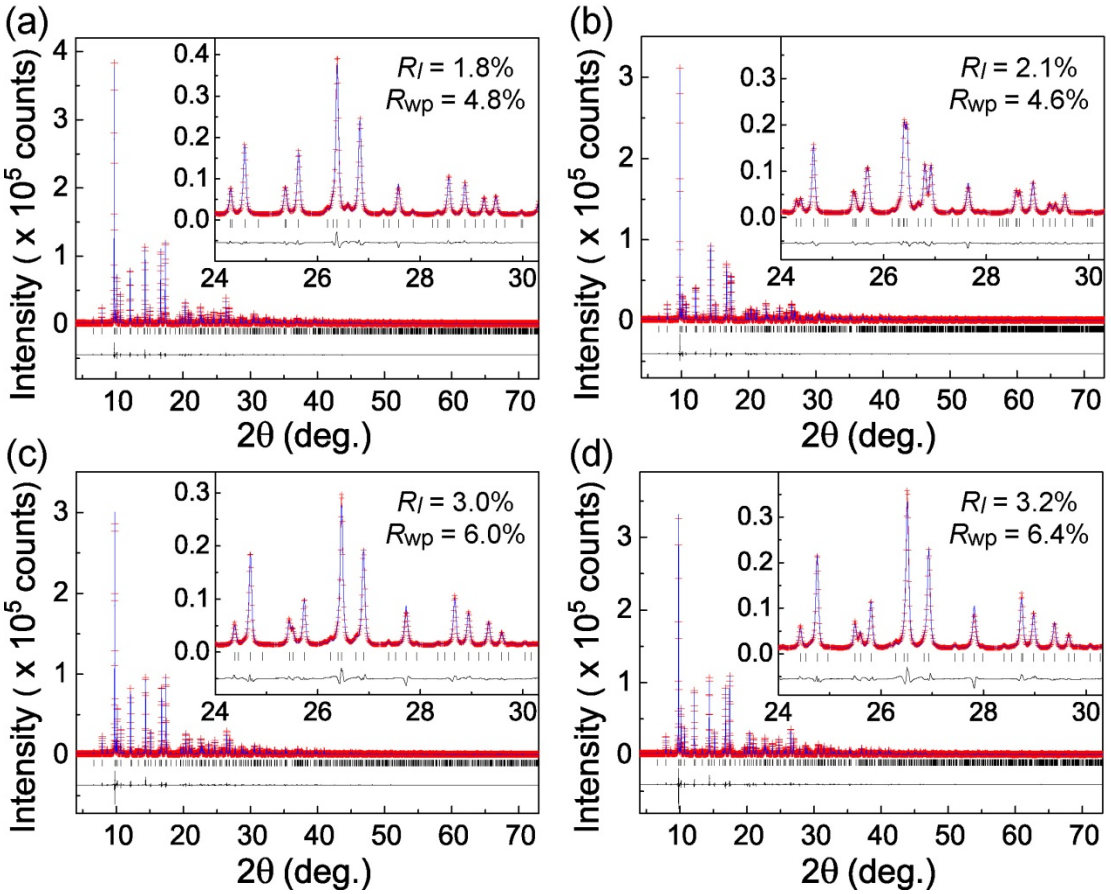

Figure 4-4. Fitting results of diffraction profiles of the parent LaFeAsO at (a) 300 K and (b) 120 K and those of the 14% F-substituted LaFeAsO at (c) 300 K and (d) 120 K. Insets show magnifies graphs between 24 and 30°.

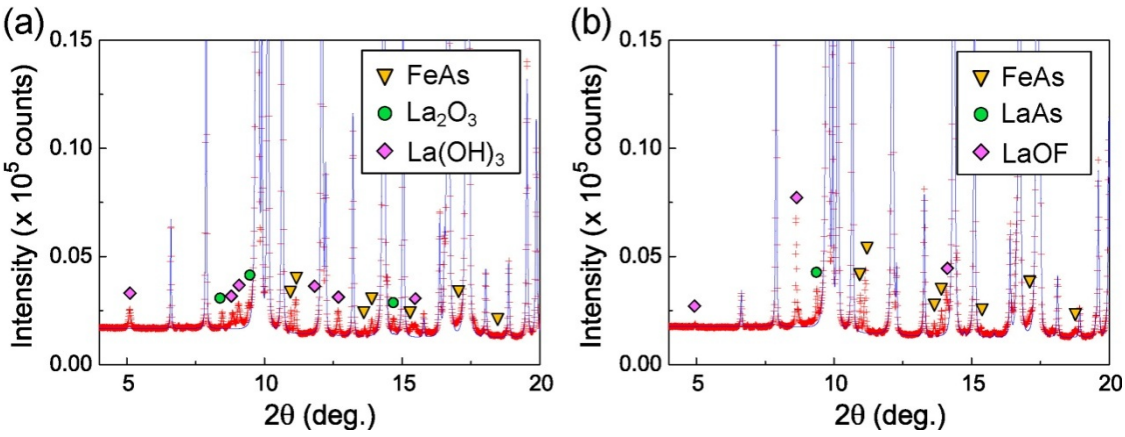

Figure 4-5. About 20 times Magnified XRD patterns of the parent and the 14% F-substituted LaFeAsO. The amounts of impurities estimated by Rietveld analysis are ~4.7, ~0.5, ~1.6 wt% for FeAs, La_2O_3, $La(OH)_3$ in the parent sample, and ~3.8%, ~1.5%, ~0.9 wt% for FeAs, LaAs, LaOF in the F-substituted sample, respectively.

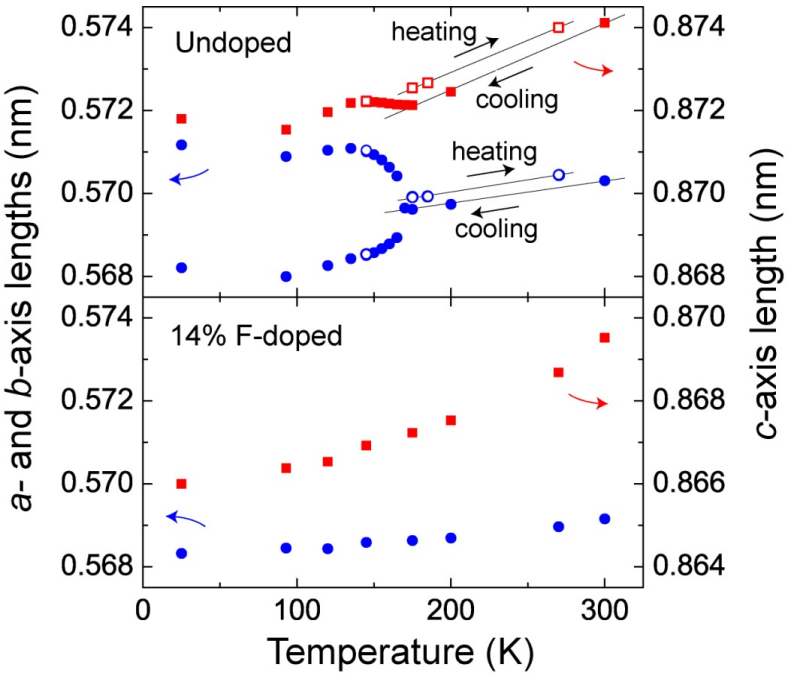

Figure 4-6. Lattice constants of *a*-, *b*- and *c*-axes of parent and 14% F-substituted LaFeAsO as a function of temperature. The *a*-axis lengths of tetragonal phases are multiplied by √2 for comparison with the orthorhombic phases. Closed and open symbols represent heating and cooling processes, respectively.

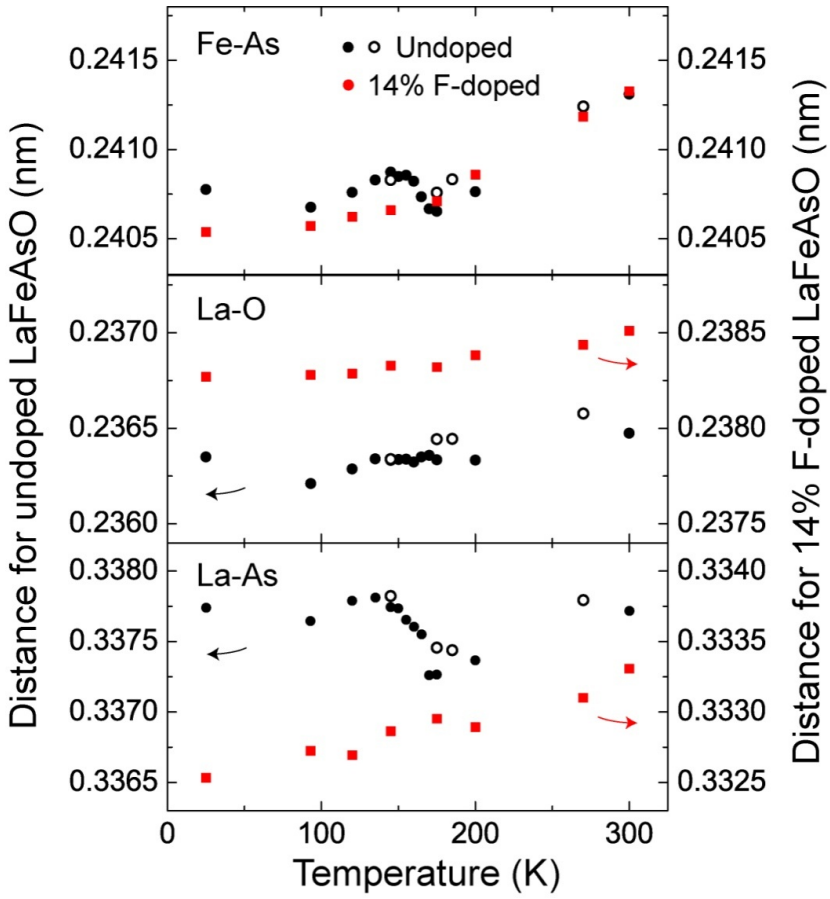

Figure 4-7. Temperature dependency of the Fe–As, La–O, and La–As bond lengths for parent and 14% F-substituted samples. Closed and open symbols represent heating and cooling processes, respectively.

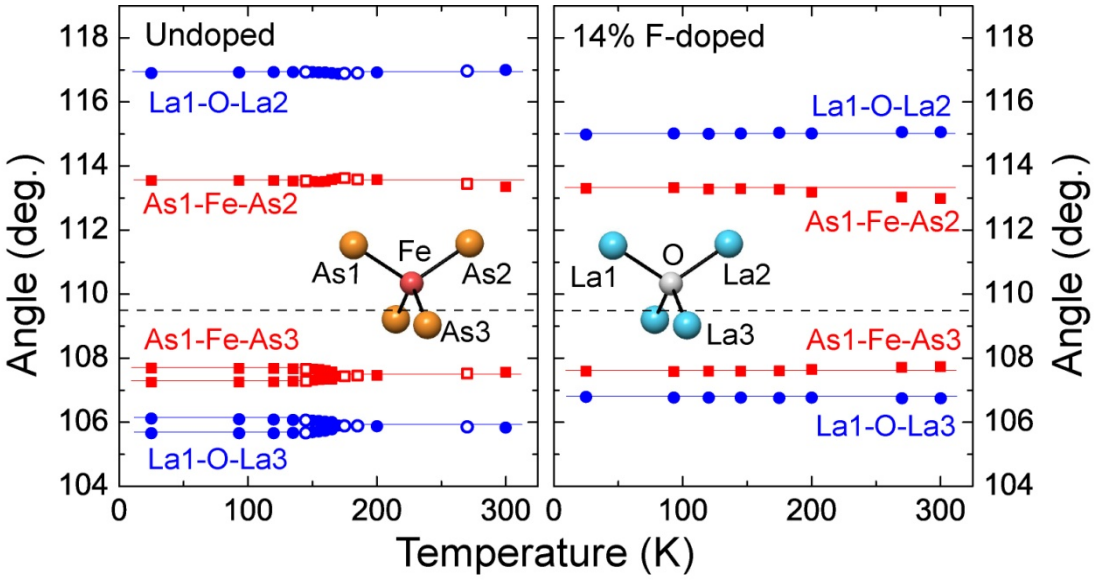

Fig. 4-8. Temperature dependence of the bond angles of the FeAs and LaO tetrahedrons for parent and 14% F-substituted LaFeAsO. The broken line corresponds to the regular tetrahedron angle (i.e. 109.47°). Closed and open symbols represent heating and cooling processes, respectively.

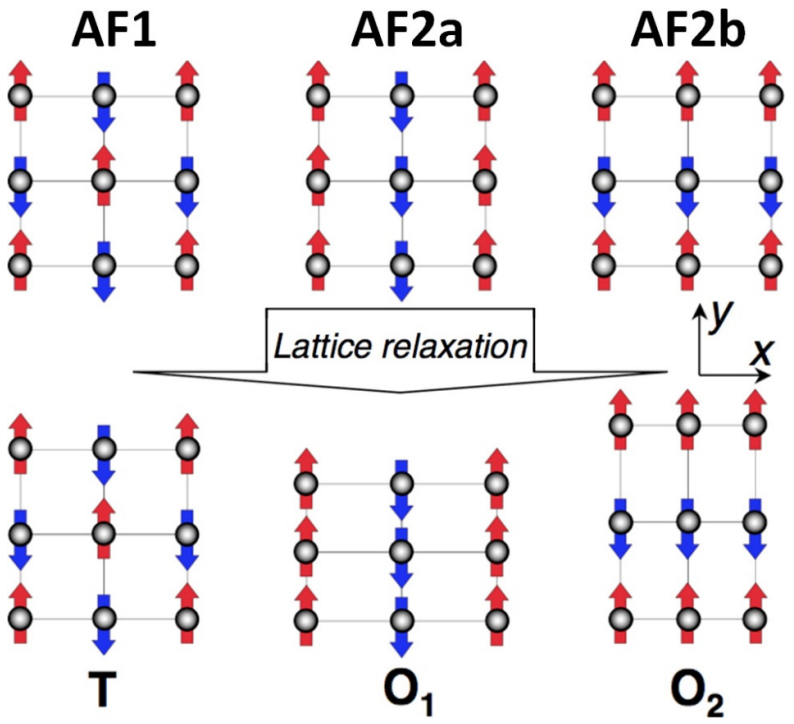

Figure 4-9. Schematic representations of Fe spin configurations in the FeAs layer of stoichiometric LaFeAsO. The arrows indicate the spin states of the Fe3d electrons. The upper images represent AF1 (checkerboard type) and AF2a and AF2b (spin stripe type) spin configurations in the tetragonal (**T**) phase, whereas the lower images represent the spin configurations of AF1, AF2a and AF2b in the orthorhombic (**O**) phase. The a-axis (x-direction) is longer than the b-axis (y-direction) in **O**1 and vice versa in **O**2.

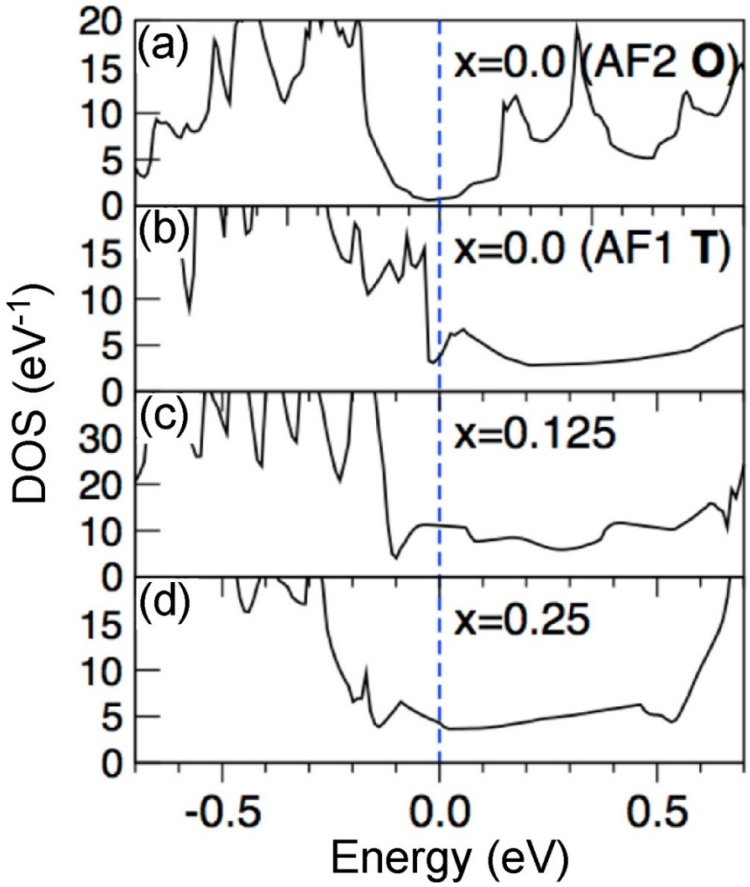

Figure 4-10. Densities of states (DOSs) calculated for $LaFeAsO_{1-x}F_x$ (a) AF2 spin configurations in the orthorhombic (**O**) phase of parent LaFeAsO (x = 0), (b) AF1 spin configuration in the tetragonal (**T**) phase of parent LaFeAsO (x = 0), (c) paramagnetic state in the **T** phase for x = 0.125, (d) paramagnetic state in the **T** phase for x = 0.25.

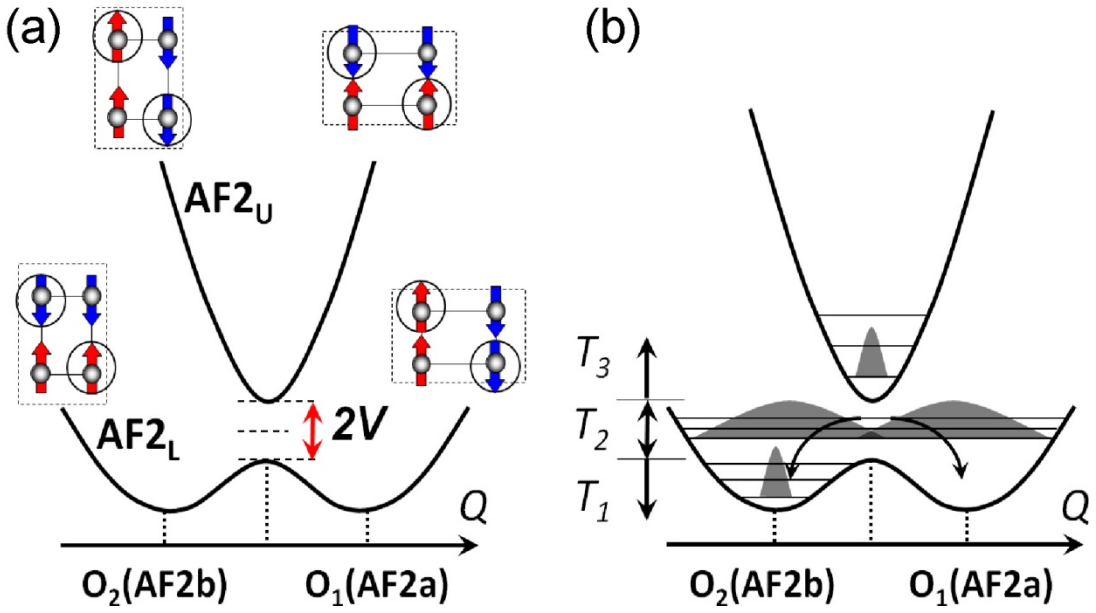

Figure 4-11. (a) Schematics of the potential energy surface calculated for AF2a and AF2b spin configurations. Their respective energy minima are in orthorhombic structures **O**1 and **O**2. The arrows indicate the spin states of Fe 3d electrons for each branch of the potential energy surface. (b) Mechanism of the structural phase transition in stoichiometric LaFeAsO. The magnetic order appears only at temperatures below *T*1 region.

Table 4-1. The structure parameters determined by Rietveld analysis for parent LaFeAsO at (a) 300 K and (b) 120 K. *B* represents the isotropic atomic displacement parameter of each site.

Atom	Site	Occ.	*x*	*y*	*z*	*B* (Å^2)
(a) Undoped LaOFeAs at 300 K (P4/*nmm*, *Z* = 2)						
a = 4.03268(1) Å		*c* = 8.74111(4) Å		*V* = 142.1524(8) Å^3		
La	2*c*	1.000	0.25	0.25	0.14134(4)	0.476(4)
Fe	2*b*	1.000	0.75	0.25	0.5	0.725(15)
As	2*c*	1.000	0.25	0.25	0.65166(7)	0.713(8)
O	2a	1.000	0.75	0.25	0	0.67(7)
(b) Undoped LaOFeAs at 120 K (C*mma*, *Z* = 4)						
a = 5.68262(3) Å		*b* = 5.71043(3) Å		*c* = 8.71964(4) Å		*V* = 282.954(2) Å^3
La	4*g*	1.000	0	0.25	0.14171(4)	0.275(3)
Fe	4*b*	1.000	0.25	0	0.5	0.415(14)
As	4*g*	1.000	0	0.25	0.65129(7)	0.386(8)
O	4*a*	1.000	0.25	0	0	0.39(6)

Table 4-2. The structure parameters determined by Rietveld analysis for 14% F-substituted LaFeAsO at (a) 300 K and (b) 120 K. The occupancy of the F atom was fixed to 14% and the isotropic atomic displacement parameter (*B*) is constrained to be that of the O atom.

Atom	Site	Occ.	*x*	*y*	*z*	*B* (Å^2)
(a) 14% F-doped LaOFeAs at 300 K (P4/*nmm*, *Z* = 2)						
a = 4.02460(2) Å		*c* = 8.69525(5) Å		*V* = 140.8405(12) Å^3		
La	2*c*	1.000	0.25	0.25	0.14725(6)	0.672(4)
Fe	2*b*	1.000	0.75	0.25	0.5	0.72(2)
As	2*c*	1.000	0.25	0.25	0.65319(10)	0.71(1)
O	2a	0.860	0.75	0.25	0	0.91(10)
F	2a	0.140	0.75	0.25	0	0.91(10)
(b) 14% F-doped LaOFeAs at 120 K (P4/*nmm*, *Z* = 2)						
a = 4.01950(2) Å		*c* = 8.66533(5) Å		*V* = 140.0004(13) Å^3		
La	2*c*	1.000	0.25	0.25	0.14774(6)	0.422(6)
Fe	2*b*	1.000	0.75	0.25	0.5	0.41(2)
As	2*c*	1.000	0.25	0.25	0.65270(10)	0.38(1)
O	2*a*	0.860	0.75	0.25	0	0.71(10)
F	2a	0.140	0.75	0.25	0	0.71(10)

Chapter 5: Structural Differences in Co- and F-substituted LaFeAsO Superconductors: Effects of Direct and Indirect Doping on Structure and Superconductivity

5.1. Introduction

Fe-based superconductors have been often compared with high-T_c cuprates due to the common features, for example, 3d metal-based superconductivity, two-dimensional layered structure, antiferromagnetic ordering in the parent compounds, doping-induced superconductivity and so on. On the other hand, resent many measurements and analyses have revealed the differences between them in electronic structure, paring symmetries, presence of nodes and so on. In addition, one of the most interesting differences between Cu-based and Fe-based superconductors is the effects of atomic substitution for the transition-metal site on the superconductivity. Substitution of the other transition-metal elements for Cu sites of cuprates does not induce the superconductivity and only reduces the T_c [1], whereas, Co and Ni substitution for Fe site of Fe-based superconductors introduces electron carriers to the Fe square lattice and induces the superconductivity although the T_c is half or less than that of F-substituted ones. Hereafter, we call carrier doping by substitution for the Fe site as “direct doping”, while for the other site as “indirect doping”. The direct doping is a unique doping technique to Fe-based superconductors and makes possible the superconductivities of *Ae*FeAsF (*Ae* = Ca, Sr) and thin film of $SrFe_2As_2$ [2,3].

Some reports have suggested the relation between the crystal structure and the superconductivity. Lee *et al.* have suggested that the T_c of *Ln*FeAsO increase as the shape of the FeAs tetrahedron reaches to regular one from experimental results [4], although the reason remains unclear. Whereas, Arita *et al.* suggested that As height from the Fe plane is critical for

the superconductive property from theoretical calculation [5]. Anyway, to examine the crystal structural changes in substitutions is important for further developments.

Rietveld anlaysis combined with Maximum entropy method (Rietveld/MEM analysis) [6] was effective methods to reveal detailed structural changes which cannot be obtained by conventional Rietveld analysis. The MEM analysis deduces electron density distribution (EDD) based on the structure factor of the preceding Rietveld analysis. As for the advantages of the analysis, distribution of valence electrons (e.g. bonding electrons) which is not taken into account by the spherical atomic model of Rietveld analysis is often observed in the resultant EDD. In addition, MEM analysis sometimes reveals unexpected information, for instance, disordered atomic distribution and/or unconsidered atom in the initial Rietveld structure model [7,8].

In this chapter, the structural differences in the direct and indirect doping were examined by Rietveld and MEM analyses of the Co- and F-substituted LaFeAsO using the synchrotron powder X-ray diffraction (XRD) patterns. Co substitution reduces the *c*-axis length with slight change of *a*-axis length, while, F substitution reduces both *a*- and *c*-axis lengths significantly. The Co substitution for Fe site only decreases the distance between Fe plane and As plane without the structural change in the LaO layer. Whereas the substitution of monovalent F^- ion for divalent O^{2-} ion weaken the Coulomb interaction with coordinating La^{3+} ions, which leads to enhance the interaction between the La ions and neighboring As ions. Co substitution (direct doping) only induces the structural change in FeAs layer, on the other hand, F substitution induce the displacement of neighboring La ion to FeAs layer, leading to the enhancement of interaction between the La ion and the coordinating As ion. Such the local structural change or lowering of the two-dimension nature possibly relate with the high-T_c of the indirectly-doped *Ln*FeAsO.

5.2. Experimental and Analysis

5.2.1. Sample Preparation and Electrical Measurements

Parent LaFeAsO sample was prepared by a solid state reaction of a 1 : 1 mixture of dehydrated La_2O_3 and a pre-sintered powder of $LaFe_3As_3$ composition in an evacuated silica tube at 1250ºC for 40 h. For Co-substituted samples, 6% and 12% of the $LaFe_3As_3$ powder were replaced by $LaCo_3As_3$ compound. Similarly, 6% and 12% of the La_2O_3 were replaced by in a 1 : 1 ratio of LaF_3 and metal La for the F substitution. Electrical resistivity of each sample was measured at 1.9–300 K by a DC four-probe technique using a Physical Properties Measurement System (Quantum Design Inc.).

5.2.2. XRD Measurements and Rietveld/MEM Analysis

High-resolution synchrotron XRD measurements were performed at the BL02B2 beamline in the SPring-8. The prepared samples were ground into a fine powder with few tens of micrometers in size, and then each of them were packed and sealed in a Lindemann glass capillary with 0.3 mm inner diameter. The capillary was set at a sample stage of a large Debye-Scherrer camera with a 286.48 mm camera radius. The monochromatic X-ray with wavelength of ~0.05 nm was irradiated, and diffracted Debye-Scherrer images were detected by Imaging Plates for 5 minutes per each sample. The diffraction data ranging from 2 to 73° with a 0.01° step in 2θ, which corresponds to 0.042 nm resolution, were employed for Rietveld analyses. Several weak extrinsic peaks attributed to Fe_2As, FeAs, La_2O_3 and LaOF were fitted as impurity phases in each analysis. A computer program, ENIGMA [9] was used for MEM analysis. The Rietveld analysis results of parent and 14% F-substituted LaFeAsO in the chapter 4 were adopted for MEM/Rietveld analyasis, where diffraction patterns measured at 120 K for 30 minutes were employed to satisfy quality of data required for MEM analysis. In the MEM

analysis, the tetragonal unit cell of the substituted LaFeAsO was transformed to orthorhombic one for the comparison with the orthorhombic parent LaFeAsO. Each unit cell was cut into 64 × 64 × 128 mesh, and then structure factors of each mesh points obtained by the Rietveld analysis were input for the initial parameter for the MEM analysis.

5.3. Results and Discussion

Figure 5-1 shows temperature-dependent electrical resistivity of $LaFe_{1-x}Co_xAsO$ and $LaFeAsO_{1-x}F_x$ for x = 0, 0.06, 0.12, respectively. Parent samples (x = 0) exhibit large decreases of resistivity in the ρ-T curves at 160 K (T_{anom}). Above the T_{anom}, the resistivity decreases with x value at a fixed temperature in both Co and F substitution, which suggests the conductive careers increase as results of the substitution. Co-substituted LaFeAsO exhibited the T_c of onset at ~16 K for x = 0.06 and ~8 K for x = 0.12. Whereas, the T_c of F-substituted samples are ~31 K for x = 0.06 and ~25 K for x = 0.12, which are twice or higher than those of Co-substituted LaFeAsO at the same x value. The resistivities of F-substituted LaFeAsO samples greatly decrease with temperature compared with those of Co-substituted samples, which may suggest that the introduced Co ions to the Fe site would be scattering centers for conductive carriers.

The dopant concentration-dependency of lattice constants, bond lengths and bond angles of $LaFe_{1-x}Co_xAsO$ and $LaFeAsO_{1-x}F_x$ are shown in Fig. 5-2, 5-3 and 5-4, respectively. In Fig. 5-2, the c-axis lengths are linearly decreases with both Co and F substitution, and the reduction magnitudes are a little higher in F-substituted system than Co-substituted one (−0.61% at 12% F substitution and −0.46% at 12% Co-substitution). The a-axis length is also decreased by 0.32% at 12% F substitution, in contrast, the length is hardly changed by Co substitution. In F-substituted system, La–As and Fe–As distances linearly decrease by 1.27% and 0.33% at 12% substitution, while La–O distance increases by 0.63% at the same doping level (Fig. 5-3). On

the other hand, Co substitution only decrease the Fe–As distance by 0.54% at 12% substitution but not affect on the La–As and La–O distances. Figure 5-4 shows that F substitution largely changes the La_4O tetrahedron to regular shape but slightly affects on the $FeAs_4$ bond angles. In contrast, Co substitution makes $FeAs_4$ tetrahedron more flattened shapes along *a–b* planes but hardly affects on the La_4O bond angles. This tendency is very similar in Co substituted SrFeAsF system (see chapter 6).

Figure 5-5 shows isosurface of an electron density level at ~0.65 $e \cdot nm^{-3}$ for parent and 14% F-substituted LaFeAsO deduced by the Rietveld/MEM analysis (Fig. 5-5(a) and (b)). At the electron density level, substantial electron distribution between La and O, and between Fe and As can be seen in both samples, which indicates the contribution of covalency for the atomic bonds. The most prominent difference between two samples is electron density distribution (EDD) at La site. The EDD of La site in parent LaFeAsO (Fig. 5-5(a)) shows rounded shape, on the other hand, that of F-substituted one (Fig. 5-5(b)) shows abnormal distribution elongating to FeAs layer. The origin of such the abnormal EDD of La site is discussed later.

The above results were summarized as schematic structural models in Fig. 5-6. In the case of Co substitution, the *c*-axis length shrinks in proportion to Co contents, accompanied by structural changes in the FeAs layer (i.e. Fe–As distance and As–Fe–As angles). Whereas, no substantial changes occur in the a-axis length, structure in LaO blocking layer (i.e. La–O distance and La–O–La angles) and interlayer distance (i.e. La–As distance). These results indicate that Co substitution in LaFeAsO decreases only the distance between Fe plane and As plane without structural changes in LaO layer and interlayer distance (Fig. 5-5(a)). It would be emphasized that the decrease of *c*-axis length is attributed to the decrease of distance between Fe plane and As plane in the case of Co substitution.

The reason why the *c*-axis lengths of Fe-based superconductors are decreased by electron doping is explained by enhancement of Coulomb interaction between $[LnO]^{\delta+}$ and $[FeAs]^{\delta-}$ layers so far [10]. However, the results of this study clearly demonstrate that electron doping by Co substitution only decreases the distance between Fe plane and As plane without changes in interlayer distance or structure of LaO layer. Therefore, the effect cannot be explained by the enhancement of Coulomb interaction between the layers. It also cannot be elucidated by different ionic radii between Fe and Co ions; because the change of *a*- and *c*-lattice constants is anisotropic, in addition, the decrease of *c*-axis lengths is too large to be explained by the difference of ionic radii. A probable reason to elucidate this effect is that the doped electrons are introduced to "bonding" orbital of covalent Fe–As bond, which decreases the distance between Fe and As plane. The increase of *c*-axis length in the case of hole doping, such like K substitution for $AeFe_2As_2$, can be accounted for the opposite reason.

On the other hand, the structural changes induced by F substitution are more complex than the case of Co substitution. F substitution monotonically decreases both *c*- and *a*-axis lengths as well as La–As and Fe–As distances, however, La–O distance inversely increase. Such structural changes can be explained as follows; the La ions which tetrahedrally coordinate to substituted F^- ion distribute farther position from the central F^- ion than the case of O^{2-} ion due to the weaker Coulomb force of the monovalent F^- ion than divalent O^{2-} ion. Instead, the La ions enhance interaction with the neighboring As ions on the other side, which make the La ion displace to the FeAs layer side (Fig. 5-5(b)). The increase of La–O distance and the decrease of La–As distances of the analysis results are consistent with above discussion. Decrease of *a*-axis length may caused by the Coulomb repulsion between neighboring divalent O ions is weakened by substitution of monovalent F^- ions.

The abnormal EDD of La site in the MEM analysis further supports the disordered

distribution of La ion due to the F substitution. The isotropic atomic distribution had been supposed in the preceding Rietveld analysis, nevertheless, the MEM analysis deduces the tear drop-shaped EDD of La site in F-substituted LaFeAsO (Fig. 5-6(b)) in contrast to the normal isotropic EDD in parent LaFeAsO (Fig. 5-6(a)). Such the abnormal EDD of La site well agreed with the above-described assumption model; The La atom neighboring the F ion distribute the farther position from the O plane comparing with La ion which coordinating to O ion. The distribution of such the displaced La ion is random because the F ions randomly substitute the O site (No superlattice reflections have been observed in the diffraction pattern of F-substituted LaFeAsO). X-ray diffraction technique observes spatially- and temporary-mean structure, therefore, overlapped multiple positions of La site are observed as tear drop-shape in the results of MEM electron density map, although the X-ray diffraction measurements can't completely distinguish that such the results caused by static or dynamic (i.e. anharmonic vibration) process.

Such the predominant local structural changes would not occur in Co-substituted LaFeAsO, because the doped electrons by Co substitution are likely to be delocalized and the charge states would be close to that of Fe ions contrary to the case of substituted F^- ions for O^{2-} ions. Carrier doping to the Fermi energy surface can be achieved by direct doping in the Fe-based superconductors in contrast to high-T_c cuprates, however, the T_c of directly-doped Fe-based superconductor is less than half of that for indirectly-doped one. The most feasible reason for it is that dopant introduced superconducting FeAs layer would be scattering centers for the Cooper pair. But as for other reasons, the structural differences observed in this study would also participate the high-T_c, such like the local strain induced by the indirectly-substituted F ion would effectively suppress the antiferromagnetic transition or proximity of La ion to FeAs layer decrease the two-dimensional nature the observed in this study.

5.4. Conclusion

The crystal structures of the Co- and F-substituted LaFeAsO were refined by Rietveld analysis using the synchrotron powder X-ray diffraction patterns, and the different effects on the crystal structure between the direct and indirect doping were examined. Co substitution reduces the *c*-axis length with slight change of *a*-axis length, while, F-substitution reduces both *a*- and *c*-axis lengths. The Co substitution for Fe site only decreases the distance between Fe plane and As plane without the structural change in the LaO layer. Whereas the substitution of monovalent F^- ion for divalent O^{2-} ion weaken the Coulomb interaction with coordinating La ions, which leads to enhance the interaction between the La ions and neighboring As ions. Co substitution (direct doping) only induces the structural change in FeAs layer, on the other hand, F substitution induce the displacement of neighboring La ion to FeAs layer, leading to the enhancement of interaction between the La ion and the coordinating As ion. Such the local structural change or lowering of the two-dimension nature possibly relate with the high-T_c of the indirectly-doped *Ln*FeAsO.

References

[1] J. M. Tarascon, L. H. Greene, P. Barboux, W. R. McKinnon, G. W. Hull, T. P. Orlando, K. A. Delin, S. Foner and E. J. McNiff, Jr. Phys. Rev. B **36**, 8393 (1987).

[2] S. Matsuishi, Y. Inoue, T. Nomura, H. Yanagi, M. Hirano and H. Hosono, J. Am. Chem. Soc. **130**, 14428 (2008).

[3] H. Hiramatsu, T. Katase, T. Kamiya, M. Hirano and H. Hosono, Appl. Phys. Express, **1** 101702 (2008).

[4] C. H. Lee, A. Iyo, H. Eisaki, H. Kito, M. T. Fernandez-Diaz, T. Ito, K. Kihou, H. Matsuhata, M. Braden and K. Yamada, J. Phys. Soc. Jpn. **77**, 083704 (2008).

[5] K. Kuroki, H. Usui, S. Onari, R. Arita and H. Aoki, Phys. Rev. B **79**, 224511 (2009).

[6] M. Takata, E. Nishibori, M. Sakata, Z. Kristallogr. 216, 71 (2001).

[7] M. Takata, B. Umeda, E. Nishibori, M. Sakata, Y. Saito, M. Ohno, H. Shinohara, Nature, **377**, 46 (1995).

[8] M. Takata, N. Machida, E. Nishibori, B. Umeda, M. Sakata, K. Tanigaki, M. Kosaka, I. Hirosawa, J. Mizuki, Jpn. J. Appl. Phys. Suppl. 38-1, 122 (1999).

[9] H. Tanaka, M. Takata, E. Nishibori, K. Kato, T. Ishii, M. Sakata, J. Appl. Cryst. **35**, 282 (2002).

[10] J. Zhao, Q. Huang, C. de la Cruz, S. Li, J. W. Lynn, Y. Chen, M. A. Green, G. F. Chen, G. Li, Z. Li, J. L. Luo, N. L. Wang and P. Dai, Nature Mater. **7**, 953 (2008).

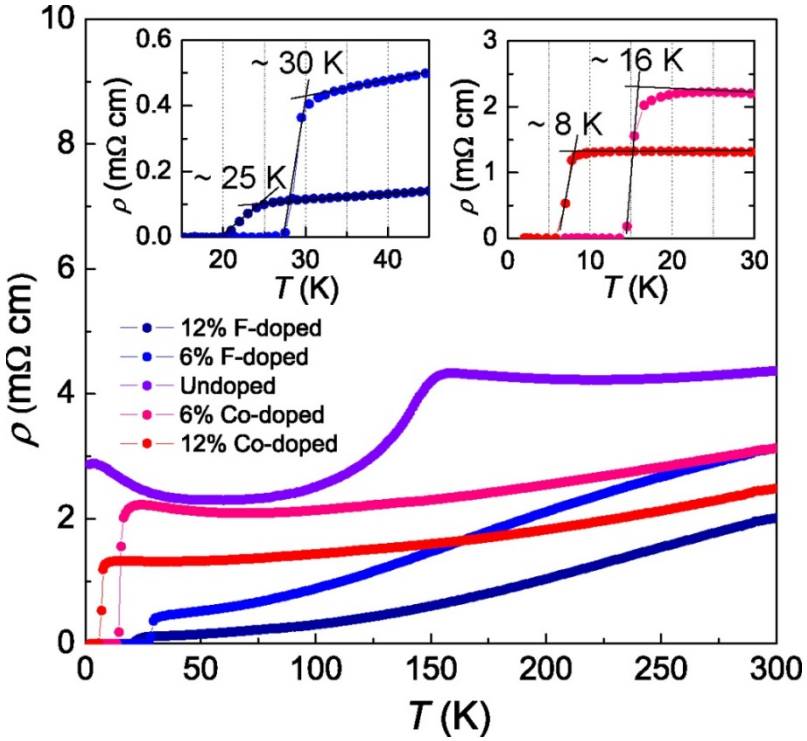

Figure 5-1. Temperature-dependent electrical resistivity of $LaFe_{1-x}Co_xAsO$ and $LaFeAsO_{1-x}F_x$ with x = 0, 0.06, 0.12. Insets show the magnified views of low temperature ranges for F-substituted and Co-substituted samples.

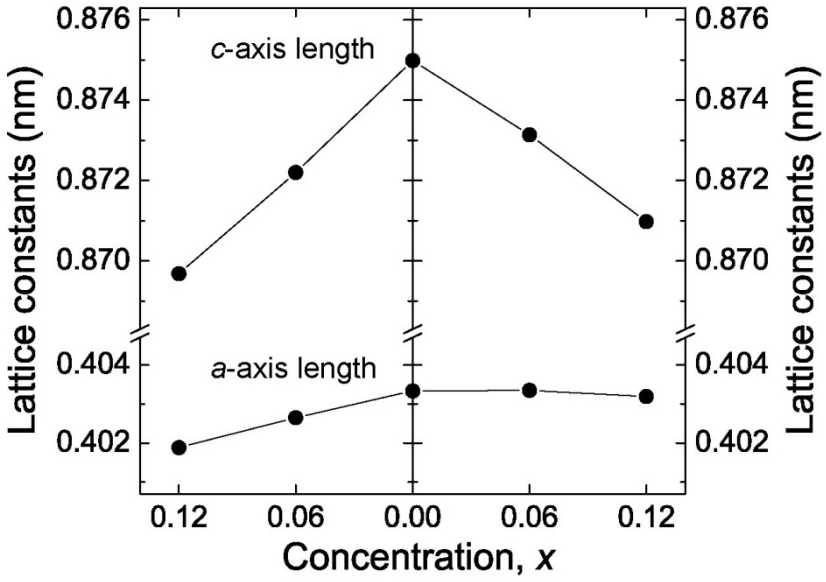

Figure 5-2. Dependence of a-axis and c-axis lengths on dopant concentration (x) for $LaFeAsO_{1-x}F_x$ (left) and $LaFe_{1-x}Co_xAsO$ (right) with x = 0, 0.06, 0.12.

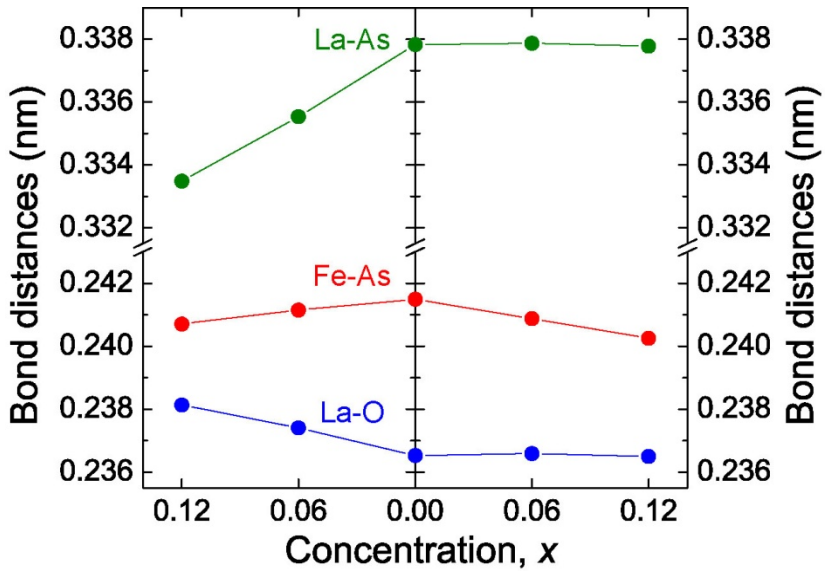

Figure 5-3. Dependence of La–As Fe–As and La–O bond lengths on dopant concentration (x) for $LaFeAsO_{1-x}F_x$ (left) and $LaFe_{1-x}Co_xAsO$ (right) with x = 0, 0.06, 0.12.

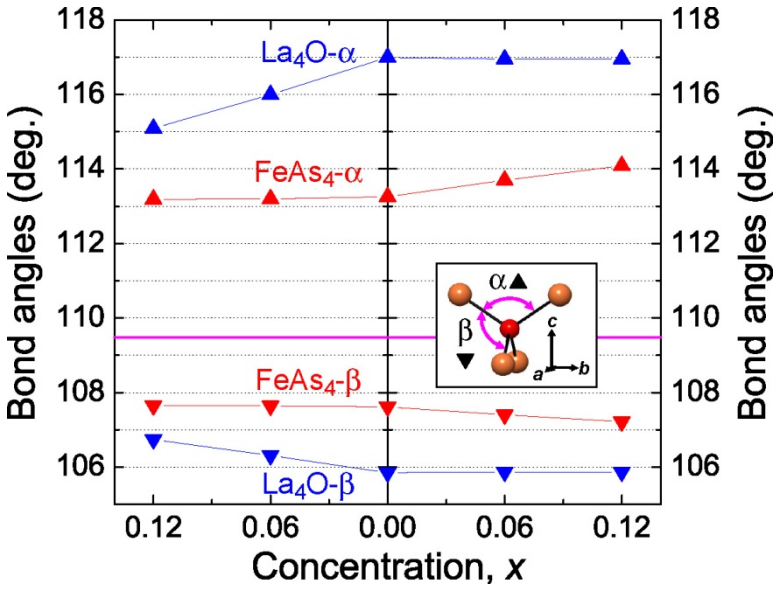

Figure 5-4. Dependence of La–O–La and As–Fe–As bond angles on dopant concentration (x) for $LaFeAsO_{1-x}F_x$ (left) and $LaFe_{1-x}Co_xAsO$ (right) with x = 0, 0.06, 0.12. The inset shows the illustration for bond angle, α and β.

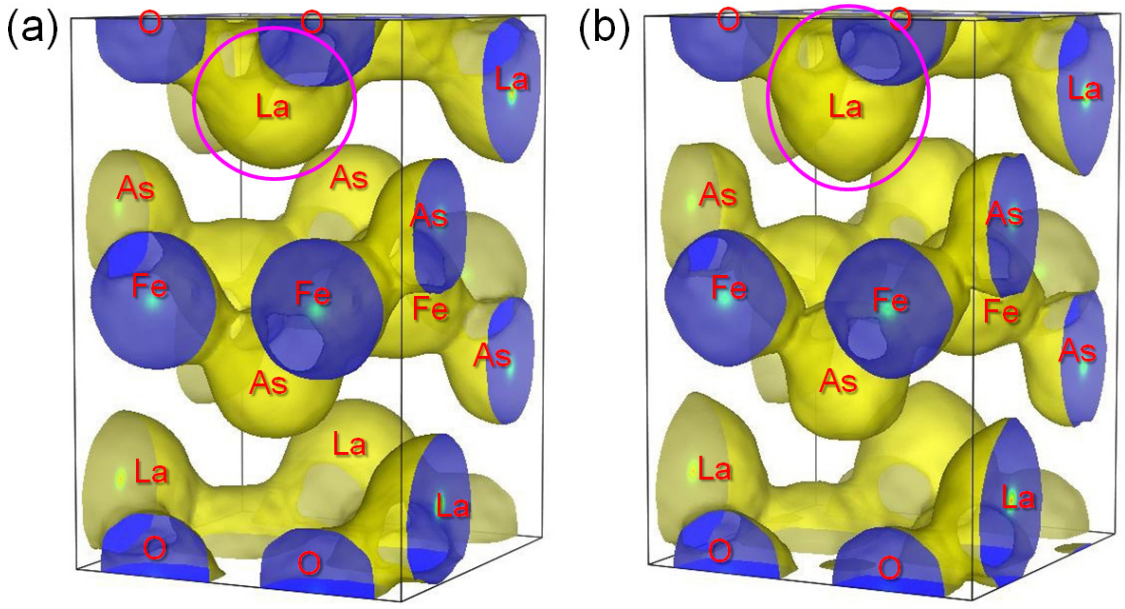

Figure 5-5. Isosurfaces of an electron density level at ~0.65 e·Å^{-3} for parent (a) and 14% F-substituted (b) LaFeAsO obtained by the MEM/Rietveld analysis. The pink circles indicate the abnormal distribution of La in the F-substituted sample compared with the parent one.

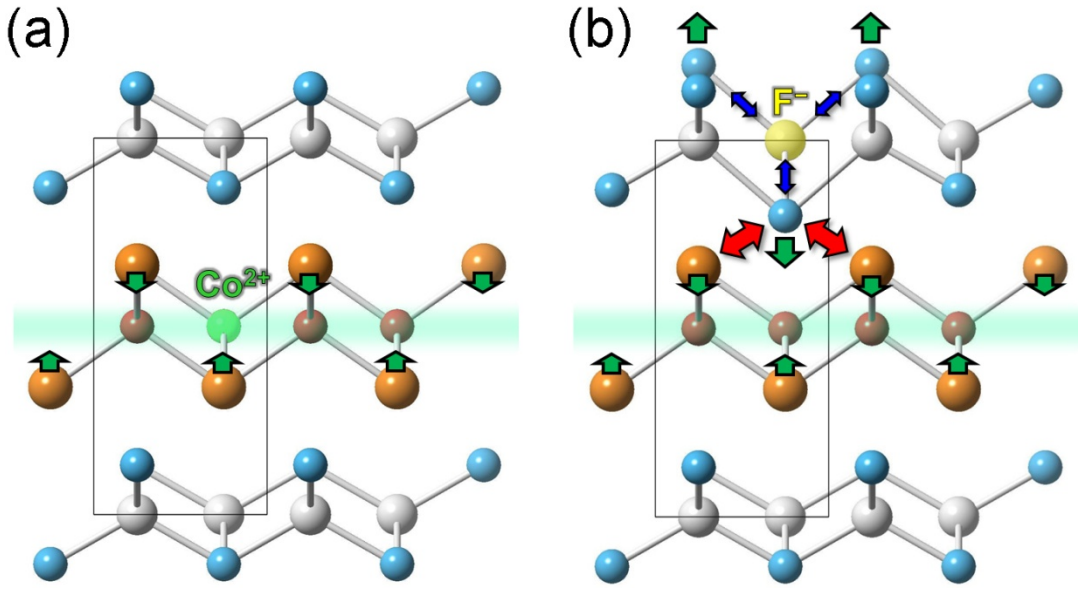

Figure 5-6. Schematic models for structural changes by Co substitution (a) and F substitution (b) viewed from the [100] direction. The green arrows represent the prominent atomic displacement; the As atoms are displaced to the Fe plane caused by electron doping. F^- ion substitution for O^{2-} site lowers the Coulomb interaction with La^{3+} ion (blue arrows), which enhances the interaction between the La ion and As ion (red arrows) and results in the displacement of La ion to the Fe plane.

Chapter 6: Crystal Structures and the Effects of Co Substitution in a *Ae*FeAsF (*Ae* = Ca and Sr): A Promising Superconductor for the Highest T_c

6.1. Introduction

Matsuishi *et al.* have recently demonstrated a new family member of the Fe-1111 compound, *Ae*FeAsF (*Ae* = Ca or Sr), with *Ae*F in place of *Ln*O as the blocking layer, which exhibits superconductivity as a result of the partial replacement of Fe with Co [1,2]. $CaFe_{1-x}Co_xAsF$ undergoes a superconducting transition for a wide range of Co concentration (x) from 0.06 to 0.30 with the maximum T_c of ~22 K at x = 0.10, whereas $SrFe_{1-x}Co_xAsF$ becomes a superconductor only in a narrow x range and relatively low T_c with ~4 K at x = 0.125. The structural and magnetic phase transitions have been also confirmed in parent SrFeAsF, whose features are quite similar to those of *Ln*FeAsO [3].

In this chapter, synchrotron XRD measurements on $CaFe_{1-x}Co_xAsF$ and $SrFe_{1-x}Co_xAsF$ (x = 0, 0.06, 0.12) from 30 to 300 K were examined, and it was demonstrate that the structural phase transitions take place at ~120 K for parent CaFeAsF and ~180 K for parent SrFeAsF. It is noteworthy that $CaFe_{1-x}Co_xAsF$, whose T_{anom} is lower than that of $SrFe_{1-x}Co_xAsF$, exhibits much higher T_c. Furthermore, the crystal structures of CaFeAsF and SrFeAsF are refined by Rietveld analyses on the XRD data and the differences in them are discussed in relation to their T_c values. Effects of the Co substitution on the structures are also evaluated, including chemical bond lengths, layer distance and magnitude of distortions of the $FeAs_4$ and Ae_4F tetrahedra from the regular tetrahedron.

6.2. Experimental and Analysis

6.2.1. Sample Preparation and Electrical Measurements

Unsubstituted (parent) *Ae*FeAsF samples were prepared by a solid state reaction of an 1:1:1 mixture of Fe_2As, Ca(Sr)As and $Ca(Sr)F_2$ powders. For Co-substituted samples, 6% and 12% of the Fe_2As ingredient was replaced by Co_2As. The mixture of ~1 g was pressed into a cubic pellet, and then sintered at 900°C for 20 h in an evacuated silica tube. Electrical resistivity measurements were conducted at 1.9–300 K for each samples by a DC four-probe technique using a Physical Properties Measurement System (Quantum Design Inc.) with the same manner described in chapter 4.

6.2.2 Sample Preparation and Electrical Measurements

High-resolution synchrotron XRD measurements at temperatures from 30 to 300 K were performed at the BL02B2 beamline in the SPring-8 Japan [4]. Polycrystalline *Ae*$Fe_{1-x}Co_xAsF$ samples were ground to a fine powder with grains of a few tens of micrometres in size, and then each was packed and sealed in a Lindemann glass capillary tube with 0.3 mm inner diameter. The capillary was set on a sample stage of a large Debye–Scherrer camera with a 286.48 mm radius. The monochromatic X-ray with wavelength of ~0.05 nm was irradiated, and two-dimensional Debye–Scherrer images were detected by imaging plates. For low temperature measurements, the capillaries were cooled by gas flow methods using N_2 gas for above 93 K or He gas for below 93 K. Diffraction patterns were measured at 300, 200, 100 and 30 K. Smaller temperature step measurements were conducted around T_{anom} for parent samples to examine their structural phase transitions.

The diffraction data ranging from 2º to 73º (N_2 gas cooling) or to 53º (He gas cooling) with a 0.01º step in 2θ, which corresponds to 0.042 nm and 0.056 nm resolution, respectively,

were employed for Le-Bail and Rietveld analyses. The lattice constants of AeFe$_{1-x}$Co$_x$AsF at various temperatures were refined by the Le-Bail method to evaluate their temperature dependence. Several weak extrinsic peaks attributed to FeAs, Fe2As and CaF2 (or SrF2) were fitted as impurity phases in each analysis. Next, the diffraction patterns measured at room temperature were subjected to Rietveld analysis to examine the structural differences between CaFeAsF and SrFeAsF and the effects of Co substitution on their structures. In the analyses, the simulated patterns of CaFeAsF were not fitted sufficiently well to the observed diffraction patterns, presumably due to the *c*-axis preferred orientations, especially in the 12% Co-substituted sample. The fitting results and their *R* values were substantially improved by using Sasa-Uda function [5] for the preferred orientation correction. On the other hand, such preferredorientation was not observed in the SrFe$_{1-x}$Co$_x$AsF samples and their diffraction patterns were well analyzed without any corrections.

6.3. Results and discussion

6.3.1. Temperature-dependent Resistivity

Figure 6-1 shows the temperature-dependent electrical resistivity of CaFe$_{1-x}$Co$_x$AsF (Fig. 6-1(a)) and SrFe$_{1-x}$Co$_x$AsF (Fig. 6-1(b)) for x = 0, 0.06, and 0.12. Parent samples (x = 0) exhibit large decreases in the ρ–T curves at T_{anom} of ~120 K for CaFeAsF and ~180 K for SrFeAsF. Above T_{anom}, the resistivity decreases with x value at a fixed temperature in both compounds, suggesting that the conductive careers are enhanced as a result of the substitution. The reduction in the resistivity in the CaFeAsF system was smaller than that of SrFeAsF at the same x value. It is noteworthy that CaFe$_{1-x}$Co$_x$AsF exhibits superconductivity at T_c ~7 K for x = 0.06 and ~24 K for x = 0.12. On the other hand, the 6% and 12% Co-substituted SrFeAsF samples do not show any clear superconductivity down to 2 K, although small decreases in the resistivity were

observed in both samples below 10 K. In addition, 6% Co-substituted CaFeAsF exhibits a small shoulder at ~55 K in the ρ–T curve, suggesting that the superconductivity appears in the orthorhombic phase. A similar resistivity shoulder is seen at ~70 K in the 6% Co-substituted SrFeAsF, although its shape is not clear.

6.3.2. Structural Phase Transition in Parent and 6% Co-substituted AeFeAsF

XRD peak profiles of the tetragonal 220 and 214 reflections of parent samples at temperatures around T_{anom} are shown in Fig. 6-2(a) for CaFeAsF and in Fig. 6-2(b) for SrFeAsF as typical examples. Both the 220 reflections split into doublet peaks, below 120 K for CaFeAsF and 185 K for SrFeAsF, which are assigned as the orthorhombic 400 and 040 reflections. All the diffraction peaks in the XRD patterns of the parent CaFeAsF and SrFeAsF samples at the higher temperatures are fitted to the tetragonal *P*4/*nmm* space group with the ZrCuSiAs-type structure, whereas those at the lower temperatures are fitted to the orthorhombic *Cmma* space group, the space groups being the same as those of the parent LaFeAsO in both temperature regions.

Figure 6-3 shows the peak profiles of the tetragonal 220 and 214 reflections of Co-substituted CaFeAsF (Fig 6-3(a) and (c)) and SrFeAsF (Fig. 6-3(b) and (d)) at several temperatures. It is noteworthy that the 220 reflection of the 6% Co-substituted CaFeAsF exhibits a single peak down to 65 K, but splits into doublet peaks at 30 K (Fig. 6-3(a)). The 220 reflection of 6% Co-substituted SrFeAsF also exhibits remarkable broadening at 30 K (Fig. 6-3(b)) although it does not clearly split into two peaks. The Rietveld fitting results of both 6%Co-substituted samples at 30 K are not sufficient when using the *P*4/*nmm* space group but are substantially improved by using the *Cmma* space group. On the other hand, both 12% Co-substituted CaFeAsF and SrFeAsF samples (Fig. 6-3(c) and (d)) show neither splitting nor broadening down to 30 K, and the patterns are consistently fitted with the *P*4/*nmm* space group

in the whole temperature region examined.

The lattice constants of $CaFe_{1-x}Co_xAsF$ and $SrFe_{1-x}Co_xAsF$, as a function of temperature, are summarized in Fig. 6-5(a) and (b), confirming the existence of the phase transition in parent and 6% Co-substituted samples, and the suppression of the transition by the 12% substitution. In the parent samples, the temperatures where the splitting starts to occur (120 K for CaFeAsF and 185 K for SrFeAsF) agree with T_{anom} observed in their ρ–T curves. Similarly, the temperatures where the splitting occurs in the 6% Co-substituted samples are consistent with the shoulder appearing temperature (~55 K for CaFeAsF and ~70 K for SrFeAsF). These results suggest that the superconductivity in the 6% Co-substituted CaFeAsF occurs in the orthorhombic phase. They also indicate that the 6% Co-substituted SrFeAsF undergoes the structural phase transition at 30 K although the superconductivity is absent.

It is further observed in the figures that the Co-substitution largely reduces the *c*-axis length in both CaFeAsF and SrFeAsF, whereas the *a*-axis length slightly changes above T_{anom}. For instance, the 12% Co substitution reduces the *c*-axis by ~0.5% and the *a*-axis by ~0.1% in both CaFeAsF and SrFeAsF. The difference between the *a*- and *b*-axes, as a result of the phase transition, reaches to ~0.7% for CaFeAsF and ~0.8% for SrFeAsF at 30 K, which are much larger than that in the LnFeAsO (~0.5% both for LaFeAsO and SmFeAsO [6,7]). It is also noted that all the lattice constants of parent CaFeAsF in both the tetragonal and orthorhombic phases monotonically decrease with lowering temperature down to 30 K, whereas those of parent SrFeAsF decrease down to 70 K, but they increase from 70 to 30 K in the orthorhombic phase. Such negative thermal expansion of SrFeAsF has been demonstrated [3] and also reported in parent PrFeAsO [8], although the physical mechanism for it remains unclear.

6.3.3. Comparison of Crystal Structure between CaFeAsF and SrFeAsF

Next, Rietveld analyses on the XRD patterns of $CaFe_{1-x}Co_xAsF$ and $SrFe_{1-x}Co_xAsF$ at room temperature were performed to obtain the refined structural parameters. The Rietveld fitting results and the refined structural parameters are shown in Fig. 6-4, Table 6-1 and 6-2, respectively. Variations in the bond lengths of Ca–As, Ca–F and Fe–As with Co concentration in the $CaFe_{1-x}Co_xAsF$ and those of Sr–As, Sr–F and Fe–As in the $SrFe_{1-x}Co_xAsF$ are shown in Fig. 6-6(a) and (b). The differences in the bond lengths of Ca–F from Sr–F and Ca–As from Sr–As (~0.013 nm) are in a good agreement with that in the ionic radius between Ca^{2+} ion (0.112 nm) and Sr^{2+} ion (0.125 nm) in the tetrahedral coordination. Furthermore, the Ca–F (~0.234 nm) and Sr–F (~0.247 nm) distances, respectively, are a little smaller than those of CaF_2 (~0.237 nm) and SrF_2 (~0.251 nm) [9]. The Fe–As distance in parent CaFeAsF (~0.239 nm) differs from that in parent SrFeAsF (~0.241 nm) by ~1%. Whereas the Fe–Fe distance, which is equal to the half of the orthorhombic *a*-axis length, is ~0.274 nm for CaFeAsF and ~0.283 nm for SrFeAsF, corresponding to ~3% difference, resulting in the different magnitude of the distortion in the $FeAs_4$ tetrahedron from the regular shape between the two compounds as discussed below.

Figure 6-7 shows the Co concentration dependence of the As–Fe–As, *Ae*–F–*Ae* bond angles of $FeAs_4$ and Ae_4F tetrahedra in CaFeAsF and SrFeAsF. The resultant distorted tetrahedra were schematically illustrated in Fig. 6-8. The $FeAs_4$ tetrahedron in parent CaFeAsF is close to the regular tetrahedron (i.e. 109.47°) with a little elongation along the *c*-axis, whereas the Ca_4F tetrahedron has a large distortion, compressed along the *c*-axis. On the other hand, the $FeAs_4$ tetrahedron in parent SrFeAsF is significantly compressed, while the Sr_4F tetrahedron exhibits a little elongated regular shape along the *c*-axis. That is, the $FeAs_4$ and Ca_4F tetrahedra in CaFeAsF are distorted oppositely to the corresponding ones in SrFeAsF, this may be caused by the difference in ionic radii between Ca and Sr. Provided that all the tetrahedra are regular and

the bond lengths are determined only by the ionic radii, the edge length of the Ca_4F tetrahedron is ~2.3% shorter than that of the $FeAs_4$ tetrahedron in CaFeAsF, whereas that of the Sr_4F tetrahedron is ~2.4% longer than that of the $FeAs_4$ tetrahedron in SrFeAsF. Therefore, to adjust these mismatches, the Ca_4F tetrahedron is flattened by the tension along the *a*–*b* plane and the $FeAs_4$ tetrahedron is elongated in the *c*-direction by the compression along the *a*–*b* plane in CaFeAsF. On the other hand, the distortion directions and the shapes of tetrahedra are opposite in SrFeAsF because of the large Sr_4F tetrahedron. Such structural mismatches can be relaxed mainly by modification of the bond angles (i.e. tetrahedron shape) rather than the bond length because of the ionic bond nature in each layer.

The geometric discrepancy between the layers is released by the structural relaxation in the tetrahedra, nevertheless, the different magnitudes of the distortion in the $FeAs_4$ tetrahedron result in ~3% difference in Fe–Fe distance between CaFeAsF and SrFeAsF as mentioned above. The Fe–Fe distance in the square lattice is an important parameter which influences the spin and charge interactions between Fe elements, most likely leading to a change in their T_c. For instance, the Fe–Fe distances of LaFeAsO (T_c ~26 K) and SmFeAsO (T_c ~55 K) are ~0.285 nm and ~0.278 nm, respectively, which are close to those of SrFeAsF and CaFeAsF. This difference may result in the reported higher T_c of the Co-substituted CaFeAsF (22 K) than that of the Co-substituted SrFeAsF (7 K) [1,2]. It is also considered that the distortion of the $FeAs_4$ tetrahedron from the regular one is smaller in CaFeAsF than in SrFeAsF, which may lead to higher T_c in CaFeAsF than that in SrFeAsF, as suggested by Lee *et al* [10], that is, the parent compounds of *Ae*FeAsF with the less distorted $FeAs_4$ tetrahedron tend to exhibit higher T_c in the Co-substituted superconductors.

6.3.4. Co-substitution Effects on Crystal Structure of AeFeAsF

The substitution of a Co ion at the Fe site monotonically reduces the Fe–As bond length in the FeAs layer of $SrFe_{1-x}Co_xAsF$ (Fig 6-6(b)), and the reduction reaches ~0.6% by the 12% Co-substitution. Furthermore, it enhances the deviation of the As–Fe–As angle from that of the regular tetrahedron of 109.47° (Fig 6-7(b)). In contrast, the Co substitution slightly modifies the Sr–F bond length (~0.1% decrease by the 12% Co-substitution) and the Sr–F–Sr bond angles in the SrF layer. In addition, the interlayer (Sr–As bond length) distance hardly changes by the Co-substitution. Such structural changes are very different from those in F-substituted LaFeAsO [6,11], where the F-substitution relaxes the distortion of the La_4O tetrahedron structure and decreases the distance between the layers (La–As bond length), but slightly affects the FeAs4 tetrahedron. The differences may firstly originate from the fact that the substituted layer suffers from structural modification more prominently than the other layer. Secondly, the Co substitution in the FeAs layer only increases the carrier density of the layer, while the indirect doping enhances not only the carrier density, but also the charge polarization of the layers. It enhances Coulomb interaction between the layers, leading to the larger reduction in the layer distance and the *c*-axis length.

In the case of CaFeAsF, the bond lengths and angles (Fig. 6-6(a) and 6-7(a)) does not likely to change systematically with the Co-concentration compared with the case of SrFeAsF. This may be due to the *c*-axis preferred-orientation of the $CaFe_{1-x}Co_xAsF$ powder samples as described in the experimental session. Nevertheless, the analysis results are still reliable enough for qualitative discussion. It is noteworthy that the Fe–As distances tend to decrease by Co substitution similar to $SrFe_{1-x}Co_xAsF$, whereas the substitution changes the As–Fe–As angle towards the regular angle, which is contrary to $SrFe_{1-x}Co_xAsF$. The Co substitution induces a modification of the FeAs tetrahedron to a more flattened one in both CaFeAsF and SrFeAsF,

leading to a change of the originally elongated tetrahedron towards a regular one in CaFeAsF, and the flattened tetrahedron towards a more distorted one in SrFeAsF. Since it is recognized that Fe-based superconductors, having the smaller distortion in the $FeAs_4$ tetrahedron, tend to exhibit higher T_c, the structural analyses suggest that CaFeAsF is a possible candidate for a higher-T_c superconductor, provided that the indirect carrier doping techniques are realized. This suggestion is further supported by the fact that CaFeAsF exhibits the highest T_c amongst all the Co-substituted Fe-1111 compounds (Fig.6-9), including $LaFe_{1-x}Co_xAsO$ and $SmFe_{1-x}Co_xAsO$ [12–14].

6.4. Conclusion

Powder synchrotron XRD patterns of newly found members of the Fe-1111 superconductor family, $CaFe_{1-x}Co_xAsF$ and $SrFe_{1-x}Co_xAsF$ (x = 0, 0.06, 0.12) were measured in the range from 30 to 300 K. The refined crystal structures were evaluated with the aid of Le-Bail and Rietveld analyses. Obtained results are summarized as follows:

(1) The tetragonal to orthorhombic phase transitions were observed at ~120 K for parent CaFeAsF and at ~180 K for parent SrFeAsF and the transition temperatures were in good agreement with kinks observed in the temperature-dependent resistivity curves. The transition temperature decreases with x, but the transition is sustained with Co substitution to x = 0.06 in both systems.

(2) The layer spacing of SrFeAsF seems not to be altered much with the Co content, which is different from the case of F-substituted LaFeAsO, presumably due to a slight enhancement of charge polarization of the layers by direct doping.

(3) Distortion of the $FeAs_4$ tetrahedron from the regular tetrahedron most likely originates from mismatches in atomic radii among the constituent elements. For instance, the larger radius

value of Sr to that of Ca causes a flattened distortion of the $FeAs_4$ tetrahedron in SrFeAsF, which is further enhanced by substitution of Fe by Co. Whereas, Co substitution in CaFeAsF leads the slightly elongated $FeAs_4$ tetrahedron to a more regular shape, which may be the reason why CaFeAsF exhibits the higher T_c. I suggest that CaFeAsF is a possible candidate for a higher-T_c superconductor due to its regular shape of $FeAs_4$ tetrahedron and the highest T_c among the Co-substituted Fe-1111 compounds.

References

[1] S. Matsuishi, Y. Inoue, T. Nomura, H. Yanagi, M. Hirano and H. Hosono, J. Am. Chem. Soc. **130**, 14428 (2008).

[2] S. Matsuishi, Y. Inoue, T. Nomura, M. Hirano and H. Hosono, J. Phys. Soc. Jpn. **77**, 113709 (2008).

[3] M. Tegel, S. Johansson, V. Weiss, I. Schellenberg, W. Hermes, R. Poettgen and D. Johrendt, Europhys. Lett. **84**, 67007 (2008).

[4] E. Nishibori, M. Takata, K. Kato, M. Sakata, Y. Kubota, S. Aoyagi, Y. Kuroiwa, M. Yamakata and N. Ikeda, Nucl. Instrum. Methods A **467/468**, 1045 (2001).

[5] Y. Sasa and M. Uda, J. Solid State Chem. **18**, 63 (1976).

[6] T. Nomura, S. W. Kim, Y. Kamihara, M. Hirano, P. V. Sushko, K. Kato, M. Takata, A .L. Shluger and H. Hosono, Supercond. Sci. Technol. **21**, 125028 (2008).

[7] S. Margadonna, Y. Takabayashi, M. T. McDonald, M. Brunelli, G. Wu, R. H. Liu, X. H. Chen and K. Prassides, Phys. Rev. B **79**, 014503 (2009).

[8] S. A. J. Kimber, D. N. Argyriou, F. Yokaichiya, K. Habicht, S. Gerischer, T. Hansen, T. Chatterji, R. Klingeler, C. Hess, G. Behr, A. Kondrat, and B. Büchner, Phys. Rev. B **78**, 140503 (2008).

[9] J. B. Forsyth, C. C. Wilson and T. M. Sabine Acta Crystallogr. A **45**, 244 (1989).

[10] C. H. Lee, A. Iyo, H. Eisaki, H. Kito, M. T. Fernandez-Diaz, T. Ito, K. Kihou, H. Matsuhata, M. Braden and K. Yamada, J. Phys. Soc. Jpn. **77**, 083704 (2008).

[11] T. Nomura, S. W. Kim, Y. Kamihara, M. Hirano, P. V. Sushko, K. Kato, M. Takata, A. L. Shluger and H. Hosono, J. Phys. Soc. Jpn. Suppl. C **77**, 32 (2008).

[12] A. S. Sefat, A. Huq, M. A. McGuire, R. Jin, B. C. Sales, D. Mandrus, L. M. D. Cranswick, P. W. Stephens and K. H. Stone, Phys. Rev. B **78**, 104505 (2008).

[13] C. Wang, Y. K. Li, Z. W. Zhu, S. Jiang, X. Lin, Y. K. Luo, S. Chi, L. J. Li, Z. Ren, M. He, H. Chen, Y. T. Wang, Q. Tao, G. H. Cao, and Z. A. Xu, Phys. Rev. B **79**, 054521 (2009).

[14] Y. Qi, Z. Gao, L. Wang, D. Wang, X. Zhang and Y. Ma, Supercond. Sci. Technol. **21**, 115016 (2008).

[15] A. Leithe-Jasper, W. Schnelle, C. Geibel and H. Rosner, Phys. Rev. Lett. **101**, 207004 (2008).

[16] G. F. Chen, Z. Li, G. Li, W. Z. Hu, J. Dong, J. Zhou, X. D. Zhang, P. Zheng, N. L. Wang and J. L. Luo, Chin. Phys. Lett. **25**, 3403 (2008).

[17] A. S. Sefat, R. Jin, M. A. McGuire, B. C. Sales, D. J. Singh and D. Mandrus, Phys. Rev. Lett. **101**, 117004 (2008)

[18] M. Rotter, M. Tegel and D. Johrendt, Phys. Rev. Lett. **101**, 107006 (2008).

[19] Y. Kamihara, T. Watanabe, M. Hirano and H. Hosono, J. Am. Chem. Soc. **130**, 3296 (2008).

[20] Z. A. Ren, W. Lu, J. Yang, W. Yi, X. L. Shen, C. Zheng, G. C. Che, X. L. Dong, L. L. Sun, F. Zhou and Z. X. Zhao, Chinese Phys. Lett. **25**, 2215 (2008).

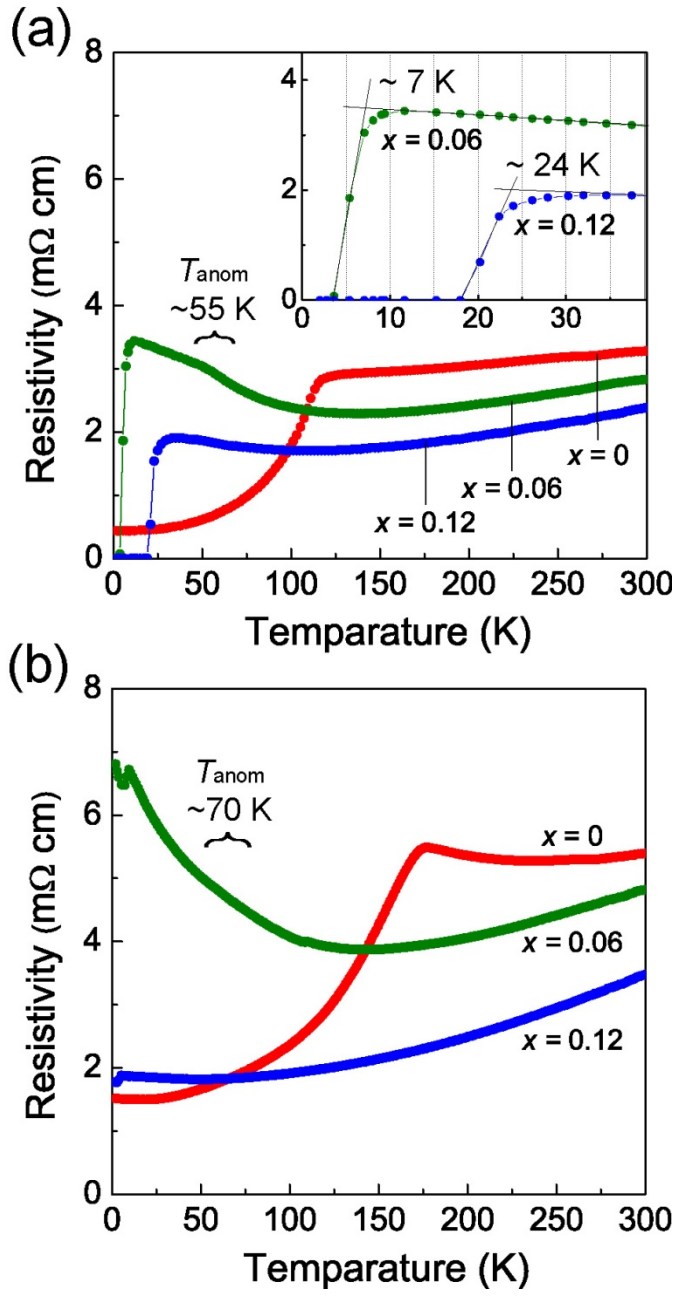

Figure 6-1. Temperature-dependent resistivity of $CaFe_{1-x}Co_xAsF$ (a) and $SrFe_{1-x}Co_xAsF$ (b) with the Co concentration, x = 0, 0.06, 0.12. The insert (a) is a magnified view of 0–40 K.

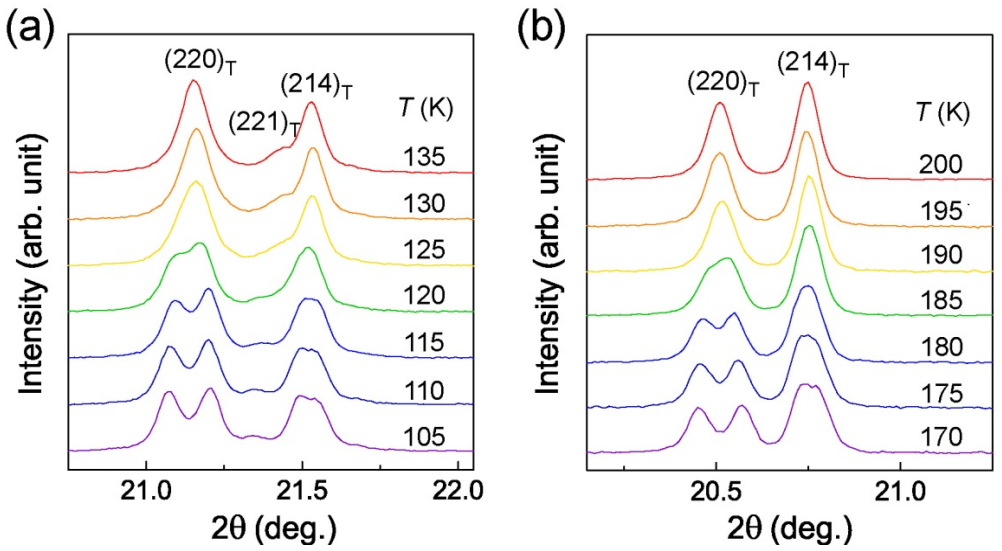

Figure 6-2. Temperature-dependent XRD peak profiles of parent CaFeAsF (a) and SrFeAsF (b) at around Tanom. The tetragonal 220 and 214 reflections in both compounds split into the orthorhombic 400, 040 and 134, 314 reflections below Tanom.

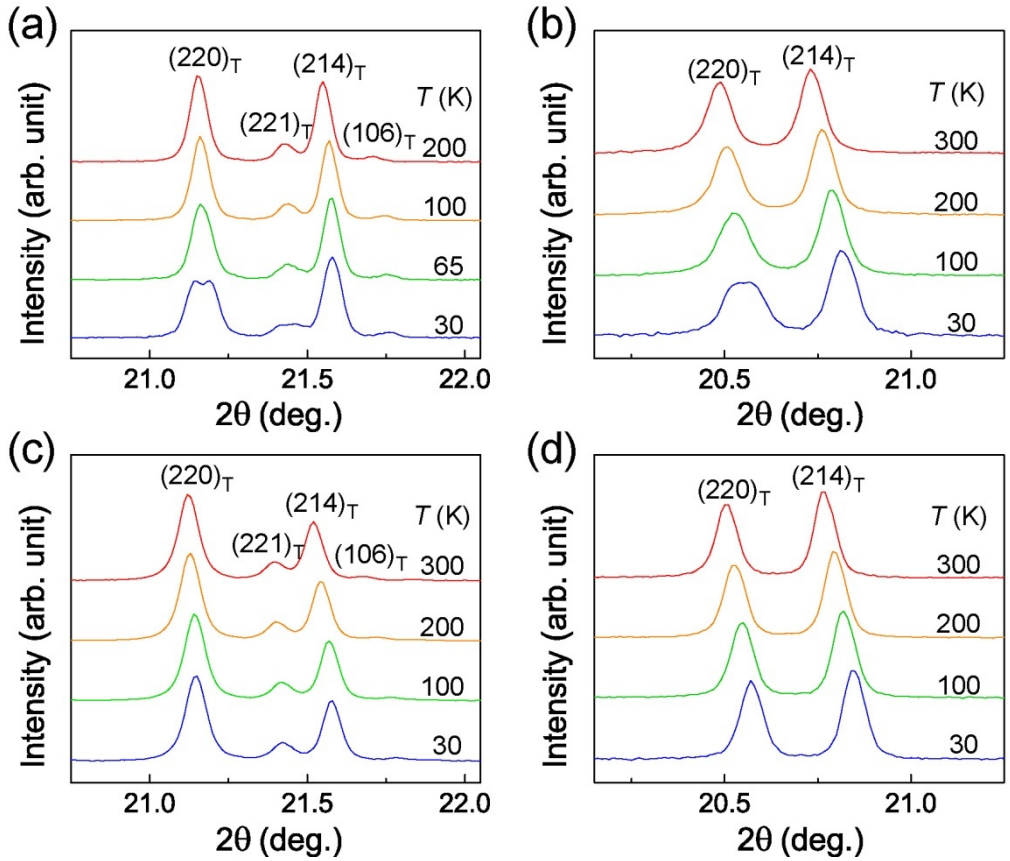

Figure 6-3. Temperature-dependent XRD peak profiles of $CaFe_{1-x}Co_xAsF$ (x = 0.06 (a) and 0.12 (c)) and $SrFe_{1-x}Co_xAsF$ (x = 0.06 (b) and 0.12 (d)) at several temperatures.

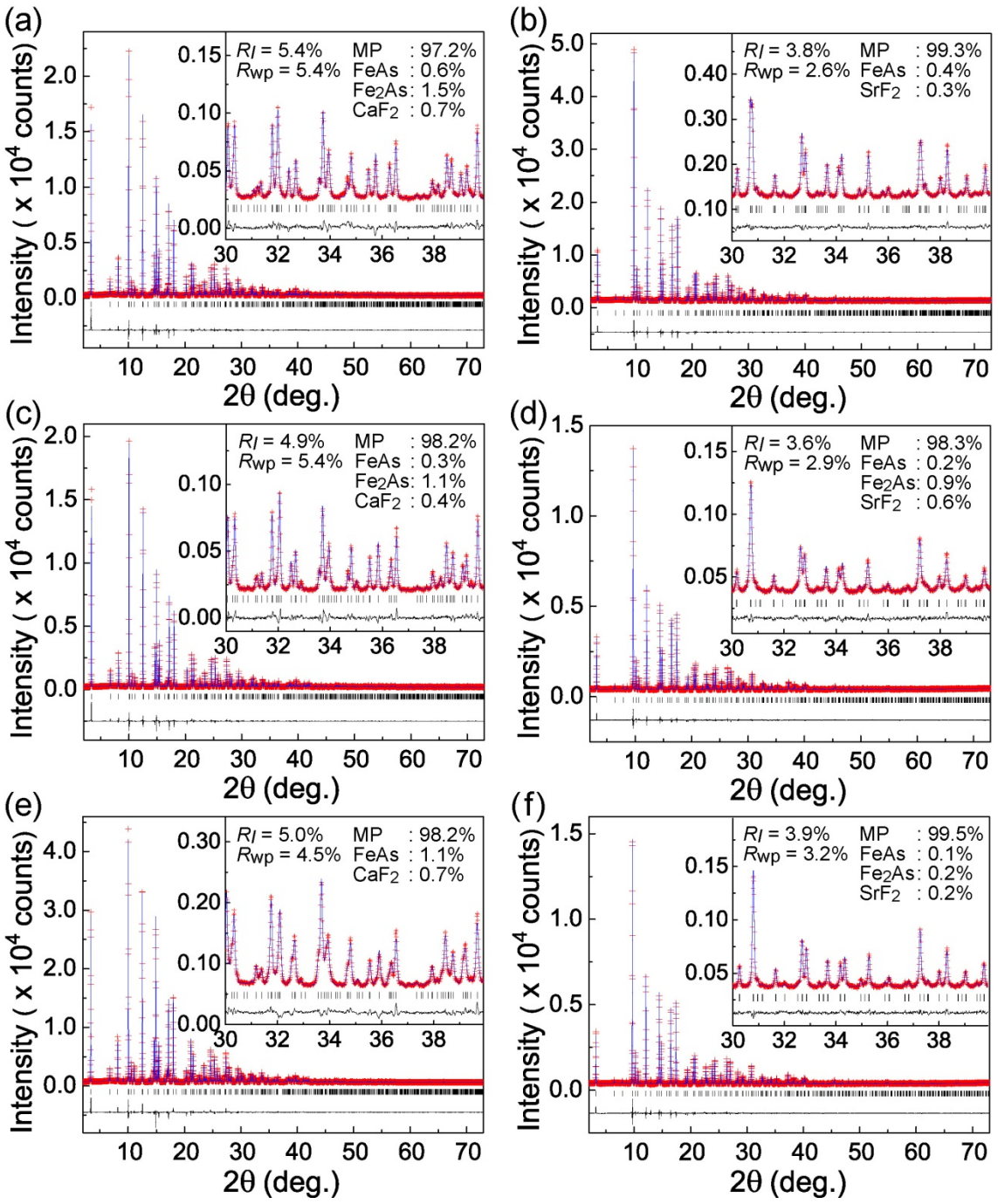

Figure 6-4. Rietveld fitting results of $CaFe_{1-x}Co_xAsF$ (x = 0 (a), 0.06 (b) and 0.12 (c)) and $SrFe_{1-x}Co_xAsF$ (x = 0 (d), 0.06 (e) and 0.12 (f)) at 300 K.

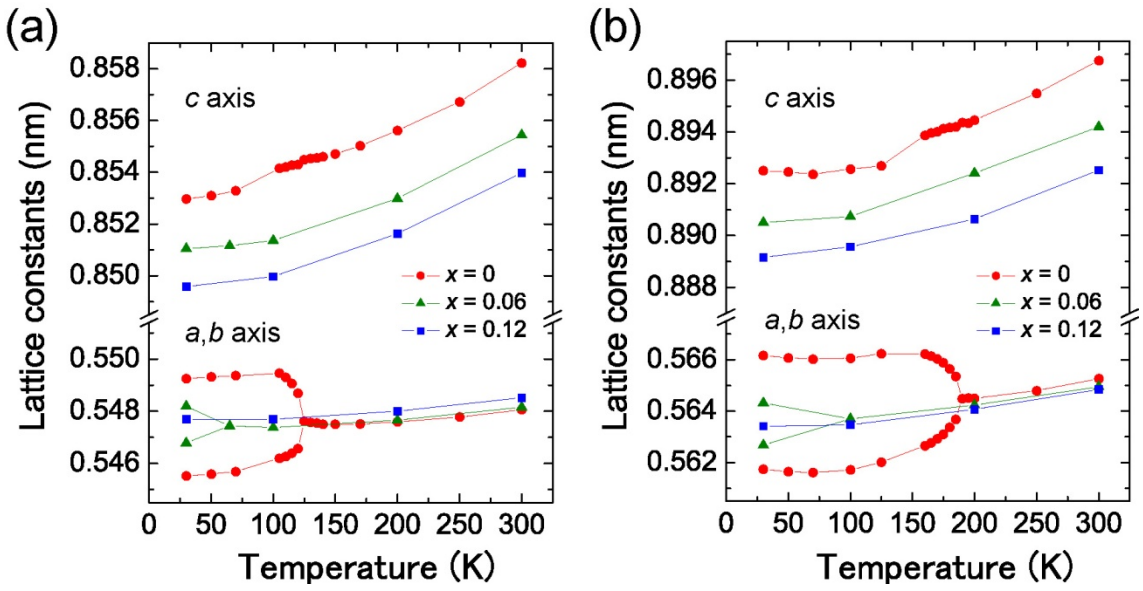

Figure 6-5. Temperature-dependent lattice constants of $CaFe_{1-x}Co_xAsF$ (a) and $SrFe_{1-x}Co_xAsF$ (b). The *a*- and *b*-axis lengths in the tetragonal phases above T_{anom} are multiplied by $\sqrt{2}$.

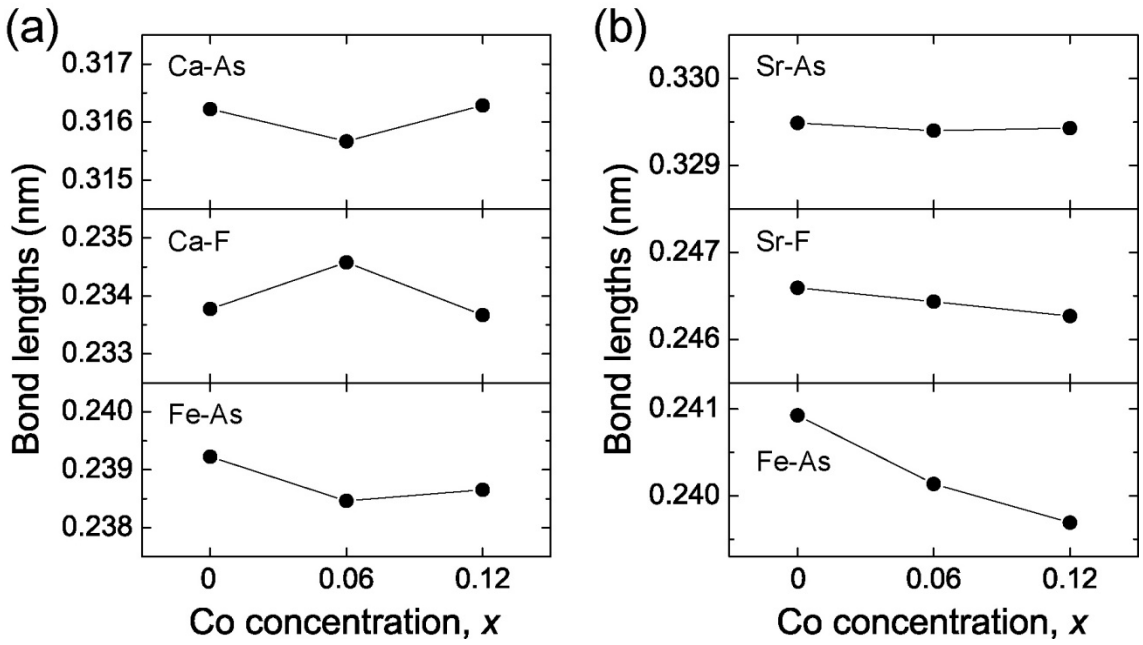

Figure 6-6. Bond lengths of $CaFe_{1-x}Co_xAsF$ (a) and $SrFe_{1-x}Co_xAsF$ (b) as a function of Co-concentration (*x*). The error bars are comparable to or smaller than the size of plotting symbols.

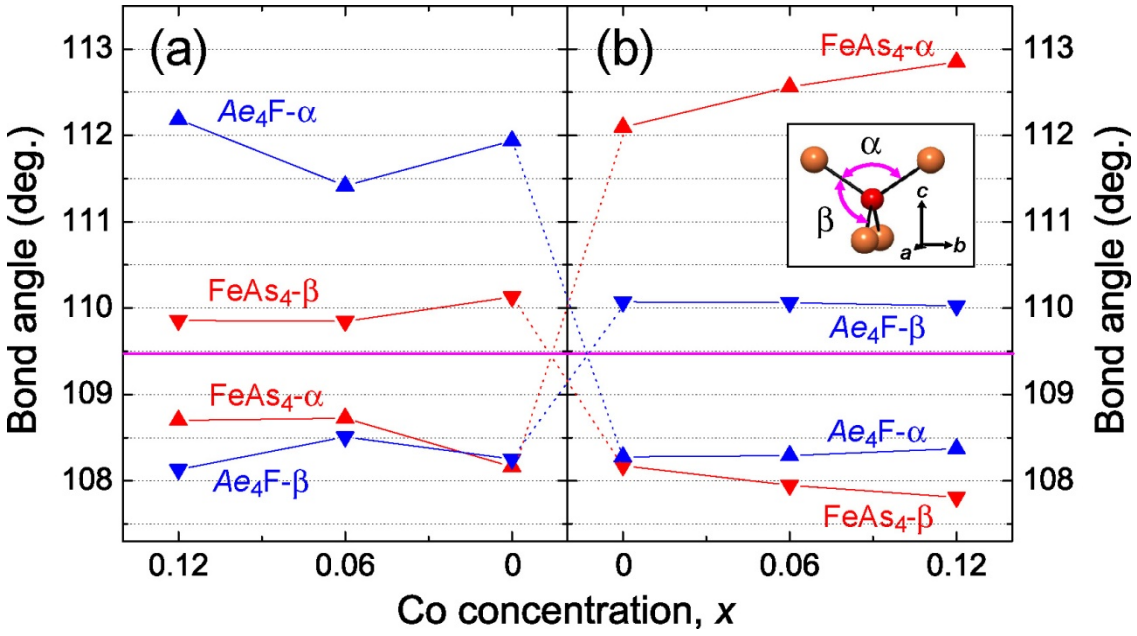

Figure 6-7. Bond angles of the FeAs4 and Ae4F tetrahedrons as a function of Co concentration (x) for $CaFe_{1-x}Co_xAsF$ (a) and $SrFe_{1-x}Co_xAsF$ (b). Open and closed symbols correspond to As–Fe–As and Ae–F–Ae bond angles, and the line on 109.47° indicates the angle of regular tetrahedron. Inset represents the tetrahedron angles, α and β, which are represented by up- and down-pointing triangles, respectively. The error bars are comparable to, or smaller than, the size of plotting symbols. Notice that Co concentration increases toward the left in (a), toward the right in (b) for comparison of each tetrahedron angle of parent samples.

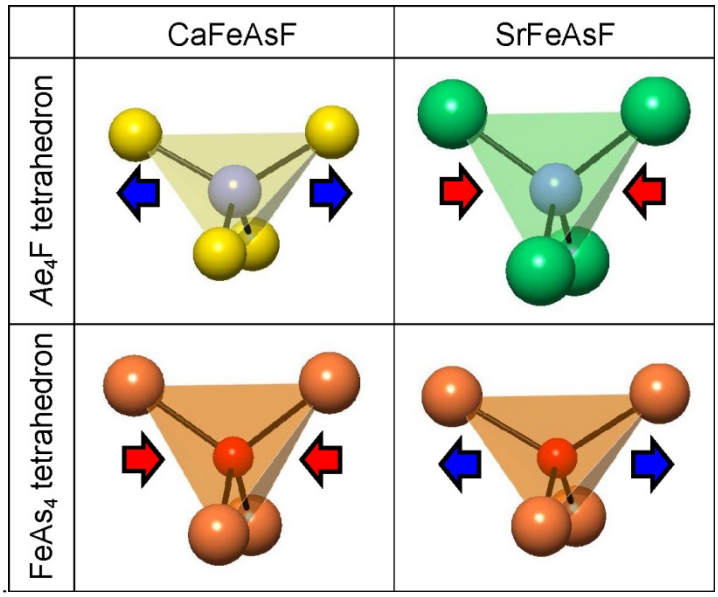

Figure 6-8. A schematic figure for comparison of the Ae_4F and $FeAs_4$ tetrahedron shape in CaFeAsF and SrFeAsF. The each tetrahedron shape is more deformed than actual ones for lucidity. Arrows indicate the directions where the tetrahedra are distorted due to the difference in size of the tetrahedron and that of the other layer.

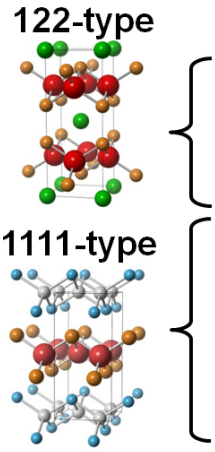

	Co substitution for Fe site	F / K substitution for blocking layer
$SrFe_2As_2$	19 K	38 K
$BaFe_2As_2$	22 K	38 K
LaFeAsO	13 K	26 K
SmFeAsO	15 K	55 K
CaFeAsF	24 K	–

Figure 6-9. Comparison of T_cs between substitution for the Fe site and for the other sites. The T_cs referred in this table is in Ref. 12–20.

Table 6-1. Refined structural parameters of $CaFe_{1-x}Co_xAsF$ with x = 0 (a), 0.06 (b) and 0.12 (c) at 300 K.

Atom	site	Occ.	x	y	z	B(Å^2)
(a) CaFeAsF at 300 K ($P4/nmm$, Z = 2)						
a = 0.387471(2) nm, c = 0.858118(6) nm, V = 0.128833(2) nm^3						
Ca	2c	1.000	0.25	0.25	0.15220(15)	0.82(2)
Fe	2b	1.000	0.75	0.25	0.5	0.503(14)
As	2c	1.000	0.25	0.25	0.66369(8)	0.610(11)
F	2a	1.000	0.75	0.25	0	1.22(6)
(b) $CaFe_{0.94}Co_{0.06}AsF$ at 300 K ($P4/nmm$, Z = 2)						
a = 0.387605(2) nm, c = 0.855441(6) nm, V = 0.128519(2) nm^3						
Ca	2c	1.000	0.25	0.25	0.15413(14)	0.86(2)
Fe	2b	0.940	0.75	0.25	0.5	0.593(14)
Co	2b	0.060	0.75	0.25	0.5	0.593(14)
As	2c	1.000	0.25	0.25	0.66243(7)	0.657(10)
F	2a	1.000	0.75	0.25	0	1.20(7)
(c) $CaFe_{0.88}Co_{0.12}AsF$ at 300 K ($P4/nmm$, Z = 2)						
a = 0.387861(2) Å, c = 0.853974(7) Å, V = 0.128469(2) Å^3						
Ca	2c	1.000	0.25	0.25	0.15264(14)	0.73(2)
Fe	2b	0.880	0.75	0.25	0.5	0.520(14)
Co	2b	0.120	0.75	0.25	0.5	0.520(14)
As	2c	1.000	0.25	0.25	0.66288(7)	0.576(10)
F	2a	1.000	0.75	0.25	0	1.42(7)

Table 6-2. Refined structural parameters of $SrFe_{1-x}Co_xAsF$ with x = 0 (a), 0.06 (b) and 0.12 (c) at 300 K.

Atom	site	Occ.	x	y	z	B(Å^2)
(a) SrFeAsF at 300 K ($P4/nmm$, Z = 2)						
a = 0.399697(2) nm, c = 0.896769(7) nm, V = 0.143266(3) nm^3						
Sr	2c	1.000	0.25	0.25	0.16109(8)	0.85(2)
Fe	2b	1.000	0.75	0.25	0.5	0.74(2)
As	2c	1.000	0.25	0.25	0.65005(10)	0.50(2)
F	2a	1.000	0.75	0.25	0	1.15(9)
(b) $SrFe_{0.94}Co_{0.06}AsF$ at 300 K ($P4/nmm$, Z = 2)						
a = 0.399477(2) nm, c = 0.894197(8) nm, V = 0.142698(3) nm^3						
Sr	2c	1.000	0.25	0.25	0.16142(9)	0.84(2)
Fe	2b	0.940	0.75	0.25	0.5	0.62(3)
Co	2b	0.060	0.75	0.25	0.5	0.62(3)
As	2c	1.000	0.25	0.25	0.64908(10)	0.44(2)
F	2a	1.000	0.75	0.25	0	1.00(9)
(c) $SrFe_{0.88}Co_{0.12}AsF$ at 300 K ($P4/nmm$, Z = 2)						
a = 0.399427(2) nm, c = 0.892577(7) nm, V = 0.142403(3) nm^3						
Sr	2c	1.000	0.25	0.25	0.16146(4)	0.75(2)
Fe	2b	0.880	0.75	0.25	0.5	0.68(3)
Co	2b	0.120	0.75	0.25	0.5	0.68(3)
As	2c	1.000	0.25	0.25	0.64851(10)	0.53(2)
F	2a	1.000	0.75	0.25	0	1.10(10)

Chapter 7: Synthesis and Characterization of a 21222-type Iron Arsenide, $Sr_2CrFe_2As_2O_2$: A New Candidate for a High-T_c Superconductor

7.1. Introduction

After the highest T_c in Fe-based superconductors was updated by the report of F-substituted SmFeAsO (T_c ~55 K) [1], some new Fe-based superconductors, including $Ae$$Fe_2As_2$ (122-type, Ae = Ca, Sr, Ba, Eu) [2–4], AFeAs (111-type, A = Li, Na) [5,6], β-FeSe (11-type) [7] have been discovered, however, their T_cs were not exceed 40 K. Compared their maximum T_c values at an ambient pressure (T_{cMAX}) with the Fe-Fe distances between FeAs layer (D_{Fe}), the T_cs tend to decrease as the D_{Fe} decreases (1111-type D_{Fe} = 0.83~0.89 nm, T_{cMAX} ~55 K: 122-type D_{Fe} = 0.58～0.67 nm, T_{cMAX} ~38 K: 111-type 0.63~0.70 nm, T_{cMAX} ~17 K: 11-type D_{Fe} = 0.54~0.55 nm, T_{cMAX} ~8 K), indicating that enhancement of the two-dimensional feature improves the superconductive property. Recently, Ogino *et al.* reported that $Sr_4Sc_2Fe_2P_2O_6$ [8] with Perovskite-like blocking layers exhibits superconductivity with T_c ~17 K which was higher than that of the other superconducting iron phosphides [9,10] by more than 10 K. This fact lets us expect that increase of D_{Fe} is effective way to rise up the T_c of Fe-based superconductors. However, the discovered isostructural iron arsenides, $Sr_4M_2Fe_2As_2O_6$ (21113-type, M = Cr, V, (Mg,Ti), D_{Fe} = 1.56~1.68 nm) [11,12] and the similar FeAs compounds with the other type of perovskite blocking layer, $Sr_3Sc_2Fe_2As_2O_5$ (32225-type, D_{Fe} ~1.32 nm) [13] have not exhibit over 40 K of T_c up to now. These results indicate that there may be the optimum interlayer distance exhibiting the best superconductive property.

Not only the interlayer distance, but also the structure of FeAs layer is important for the superconductive property of Fe-based superconductors. Lee *et al*. demonstrated that the closer

the bonding angle of FeAs tetrahedron (α) approaches to that of the regular tetrahedron (109.47°), the higher its T_c becomes in *Ln*FeAsO system by using reported experimental data [14]. This empirical rule was sustained by the other reports and has been regarded as one of the important parameter to evaluate the property of the Fe-based superconductors, although any theoretical supports have not published to my best knowledge. Recently, Kuroki et al suggested that the height of pnictogen atom from Fe-square plane (h_{Pn}) plays the important role for appearance of high-T_c superconductivity [15]. According the theory, the higher pnictogen position induces appearance of the Fermi surface (γ) around (π, π), which enhances the nesting effect improving the superconductive properties. Although above discussions are still controversial, the structure of FeAs layer seems to be important factor for the superconductive property. The structure of FeAs layer is strongly affected by structure-type and constituent elements of the blocking layer, therefore, to search FeAs compounds including new blocking layers is one of the keys to break the current stagnation of the T_c development and also for clarification of the mechanism of the high-T_c superconductivity.

One valid way to search new compounds containing FeAs layer is to refer the reported materials containing CuS layer in their structures [16,17], because these layers are substitutable due to their similar structures and charge states. I focused on one of CuS homologous compounds $[Sr_{n+1}M_nO_{3n-1}][Cu_2S_2]$ and noticed that the interlayer distance of $[Sr_2CrO_2][Co_2As_2]$ (n = 1) [17] is close to that of high-T_c *Ln*FeAsO system. In this chapter, a new FeAs compound, $Sr_2CrFe_2As_2O_2$ corresponding to the case of n = 1 of the homologous compound $[Sr_{n+1}M_nO_{3n-1}][Fe_2As_2]$ (Fig. 7-1(a)) was successfully synthesized. The X-ray diffraction (XRD) pattern was analyzed by Rietveld method, and the valence of Cr estimated from the refined structural parameters was compared with that of the other FeAs compounds including perovskite blocking layers. The electronic structure of $Sr_2CrFe_2As_2O_2$ including DOS and

charge state was calculated by *ab initio* calculation and the relations with conductive and magnetic properties were discussed.

7.2. Experimental and Calculation

The target material was prepared by solid state reaction using a SrO powder (99.99%) and some arsenide reagents. The arsenides reagent for starting materials, SrAs, CrAs, Cr_2As and Fe_2As were prepared from mixtures of elementary reagents in stoichiometric ratio using commercial products, Sr (99.99%, Cr (99.99%), Fe (99.99%) and As (99.9999%). The mixtures encapsulated in evacuated silica tubes were annealed at a 30°C/h heating rate and kept at 650°C for SrAs and 750°C for CrAs, Cr_2As and Fe_2As for 15 h. For the SrAs reagent, the treated compound was ground into a course powder and reannealed in an evacuated silica tube again for 15 h to eliminate the unreacted parts. The obtained reagents were confirmed as single phases by XRD measurements. The mixture of obtained reagents with $Sr_2CrFe_2As_2O_{2-x}$ composition (see below) are pressed into a cylindrical pellet and sintered at 900°C for 10 h in an evacuated silica tube. The pre-sintered sample was ground and pressed into a pellet again and reannealed at 1000°C for 30 h. The powder XRD patterns of samples were measured by using an X-ray diffractometer (Bruker D8 Advance) with Cu-Kα radiation (λ ~0.154 nm). The obtained XRD data was fitted by using a Rietveld analysis program, RIETAN-2000 [18]. The electrical resistivity measurements were conducted at 1.9–390 K by a DC four-probe technique using a Physical Properties Measurement System (PPMS, Quantum Design Inc.). The magnetic properties were measured at 1.9–390 K by using the PPMS equipped with vibration sample magnetometer (VSM) option. *Ab initio* calculations were carried out using density functional theory (DFT). The generalized gradient approximation (GGA) density functional of Perdew and Wang (PW91) and the projected augmented-wave method as implemented in the computer code

VASP [19] were used. The total energy was minimized with respect to the coordinates of all atoms. For the analysis of the electronic structure, the charge density was decomposed over the atom-centered spherical harmonics.

7.3. Results and Disscussion

7.3.1. Sample Preparation and Crystal Structure of $Sr_2CrFe_2As_2O_2$

For the synthesis of $Sr_2CrFe_2As_2O_2$, I firstly tried to fabricate the compound with stoichiometric composition by a following chemical reaction formula.

$$2\ SrO + CrAs + Fe_2As \rightarrow Sr_2CrFe_2As_2O_2$$

However, about 20 wt% of impurity phases, mainly $Sr_4Cr_2Fe_2As_2O_6$ (21113-compound), were observed from the powder XRD pattern of the sintered sample. The results were not changed with any heating temperatures and times, even using the other starting reagents. Then, the proper composition was searched by changing mixture ratio of the reagents and found that nearly single phase was obtained in the oxygen-poor composition. Amount of O was controlled by the following chemical reaction formula.

$$(2-x)\ SrO + (1-2x)\ CrAs + x\ SrAs + (1-x)\ Fe_2As + (1-x)\ Cr_2As \rightarrow Sr_2CrFe_2As_2O_{2-x}$$

The almost single phase of $Sr_2CrFe_2As_2O_2$ could be obtained in the condition of x ~0.1 although a few weight-percent of impurity compounds, $(Fe,Cr)_2As$ and $(Fe,Cr)_3O_4$ were detected by the XRD pattern.

The XRD pattern of $Sr_2CrFe_2As_2O_2$ at room temperature and the Rietveld fitting result were shown in Fig. 7-2. All peaks in obtained XRD patterns were consistently assigned to $Sr_2CrFe_2As_2O_2$ assuming the isostructure of tetragonal $Sr_2MCu_2S_2O_2$ (space group: $I4/mmm$) except for a few weak peaks attributed to impurity phases ($(Fe,Cr)_2As$ (~2.3 wt.%), $(Fe,Cr)_3O_4$ (~0.9 wt.%) and $SrFe_2As$ (~0.7 wt.%)). The resulting R_{wp} and R_I values were 12.8 and 4.5,

supporting the assumed structure model reproduces the measured XRD pattern properly. The refined *a*-axis length (0.3998 nm) are close to those of *Ln*FeAsO (0.39~0.40 nm), while the interlayer distance D_{Fe} ~0.92 nm, which is half of the *c*-axis length (1.8439 nm) for this system, is a little larger than those of *Ln*FeAsO (8.3 ~ 8.75 nm).

Table 7-1 shows the refined structure parameters of $Sr_2CrFe_2As_2O_2$. The occupancy of each atom was refined without changing them with the atomic displacement parameters (*B*) simultaneously. The refined FeAs bonding angle (α), ~110º, is close to that of the regular tetrahedron (~109.47º), which suggests $Sr_2CrFe_2As_2O_2$ has a promising structure for Fe-based superconductors considering the empirical rule of relation between As–Fe–As bond angle and T_c [14].

Figure 7-1 shows crystal structure of a homologous system, $[Sr_{n+1}M_nO_{3n-1}][Fe_2As_2]$ with the case of n = 1 and 2. A blocking $[Sr_{n+1}M_nO_{3n-1}]$ layer is constructed of n numbers of MO_2 planes and interstitial Sr atoms, which can be regarded as a part of perovskite structure as well as 21113-type FeAs compounds. A previously-reported 32225-compound, $Sr_3Sc_2Fe_2As_2O_5$ [9] corresponds to the homologous compound of n = 2. The two MO_2 plane in the blocking layer was linked with bridging oxygen atoms, leading to five-fold oxygen coordination of *M* atom. In the case of 21113-type compounds, the *M* atom is also coordinated by five O atoms, which is similar to the coordination geometry of *M* atom in the 32225-compounds. While, in the case of n = 1, a blocking layer unit includes a single MO_2 plane which corresponds to square-planar oxygen coordination of *M* atom if the two As atoms coordinated to the top and bottom of *M* atom were ignored. This structure can be considered that a single MO_2 plane is sandwiched by layer units of $SrFe_2As_2$.

7.3.2. Valence of Cr and Comparison with Other Perovskite-related Iron arsenides

To compare the difference of the coordination and charge states of the *M* atom in each structure, the valence of Cr in $Sr_2CrFe_2As_2O_2$ and $Sr_4Cr_2Fe_2As_2O_6$ was estimated by calculation of bond valence sum [20,21] obeying following formula.

$$s_{ij} = \exp((l_0 - l_{ij})/B)$$

The valence of cation *j* can be estimated from the sum of bond valences (s_{ij}) of each coordinating anion *i*. The bond valence parameters (l_0) are empirically determined value for each cation *j* and anion *i*, l_{ij} is actual bond length determined by structure analysis, and *B* is a empirically defined constant (0.037 nm) which is a common value for all bonds. Not only the nearest O atoms, but also the next nearest As atoms were considered for the calculation. The obtained value, ~2.1 for $Sr_2CrFe_2As_2O_2$ calculated by using the refined structure parameters indicates that the Cr ion in the blocking layer is nearly divalent state in the single MO_2 plane. While, the valence of Cr in $Sr_4Cr_2Fe_2As_2O_6$ estimated by using structure parameters in Ref. 8 was ~3.0, suggesting trivalent state in the five-fold oxygen coordination. The valences of *M* atom in the other compounds estimated by using the structure parameter in Ref. 12–14 were ~3.1 for $Sr_3Sc_2Fe_2As_2O_5$, ~3.0 for $Sr_4Sc_2Fe_2As_2O_6$, and ~2.7 for $Sr_4V_2Fe_2As_2O_6$, which further suggesting *M* atom likely to be trivalent state in the thicker blocking layer owing to the more oxidative coordination. The divalent state of Cr in $Sr_2CrFe_2As_2O_2$ is further supported by the DFT calculation; the calculated d electron number of Cr was ~4.1, suggesting $3d^4$ configuration of the Cr^{2+} ion.

The substitution of the other 3d transition metals for the Fe site of $Sr_2CrFe_2As_2O_2$ in the FeAs layer was tried, and the complete substitution could be achieved in the case of Cr, Mn, Co and Ni. On the other hand, the attempt to fabricate $[Sr_2FeO_2][M_2As_2]$ of which the square-planar site is occupied by Fe atoms resulted in segregation of many of the other impurity phases. These

results suggest that Cr atom is likely to occupy the square-planar site contrast to Fe atom. In the case of square-planar coordination, the d(x^2-y^2) orbital becomes most unstable state among the other 3d orbitals by the ligand field splitting. The $3d^4$ configuration of Cr^{2+} (high spin state) is likely to stabilized by such the energy level structure, which may be the one of reasons why the Cr atom is likely to occupy the site of square-planar coordination in $[Sr_2CrO_2][M_2As_2]$. Cu atom also tends to occupy the square-planar site (ex. $[Sr_2CuO_2][CuS_2]$) attributing to the $3d^9$ configuration of Cu^{2+} for the similar reason.

7.3.3. Electrical and Magnetic Properties and Band Structure

Figure 7-4 shows temperature-dependent resistivity (ρ-T) and magnetic susceptibility (χ-T) of $Sr_2CrFe_2As_2O_2$. The resistivity at room temperature is close to that of metallic LnFeAsO (a few mΩ·cm), while, the resistivity increases with decreasing temperature especially below 100 K, although the increase rate is significantly low compared with semi-conductive compounds such as LaMnAsO [22]. According to the magnetic property, the magnetic susceptibility gradually increases with decreasing temperature, however, the increase rate is too low to fit by the Curie-Weiss law with meaningful parameters. A weak peak observed at around 350 K would be attributed to the antiferromagnetic transition of impurity Fe_2As [23].

Figure 7-5 shows the density of states (DOS) of Fe and Cr atoms in $Sr_2CrFe_2As_2O_2$ calculated by VASP code. The Fermi surface was mainly composed by Fe 3d orbitals, therefore, the FeAs layer critically contributes to the electron conductive property as well as the other FeAs compounds. The widely-broadened Fe3d orbital from −4 to 2 eV also suggests delocalized feature in the FeAs layer. On the other hand, Cr 3d orbitals are located from −2 to 0 eV and show comparatively narrow band width owing to the localized feature of the blocking $[Sr_2CrO_2]$ layer. The overlap of Cr orbitals on Fermi surface is slight, therefore, the CrO2 layer would not

directly contribute to the conductive property.

The measured χ-*T* curve does not obey the Curie-Weiss law as mentioned above, which indicate any paramagnetic components of localized magnetic moments were not observed in the range from 1.9 to 390 K. In addition, the neutron diffraction measurement does not exhibit any magnetic phase transition in the range from 300 K to few K [24]. These results imply that the macroscopic magnetic moments of Cr atoms would be cancelled each other by their antiferromagnetic ordering at least up to room temperature. According to the *ab initio* calculation results, the magnetic moments of Cr order in checkerboard-type antiferromagnetic configuration in CrO_2 plane (i.e. antiferromagnetic ordering to {110} direction) with 3.1 effective moments per each Cr atom. Besides, the calculation results also suggest antiferromagnetic ordering of magnetic moments on Fe atoms with 1.3/1.7 μB, however, actual magnetic property would show itinerant antiferromagnetic or paramagnetic behavior as seen in other FeAs compounds, reflecting delocalized nature of FeAs layer. The detailed magnetic structure would be studied by neutron diffraction or Mossbauer spectroscopy measurements in near future.

Neither superconductivities nor resistivity anomalies as observed in the other iron arsenides have been observed in this system yet. One of the possible reasons is a few percents of Cr substitution for Fe site as reported in $Sr_2CrFeAsO_3$ [25], which is also implied by the fact that gradual increase of the ρ-*T* curve below 100 K (Fig. 3) is similar to the resistivity behavior of Cr-doped iron arsenides [26,27]. Replacement of Cr in the blocking layer with the other divalent elements might be an effective way to prevent the mixing and to change this material to a new superconductor.

7.4. Conclusion

A 21222-type iron arsenide, $Sr_2CrFe_2As_2O_2$ containing a single CrO_2 layer in the blocking layer was successfully fabricated. The structure formula is denoted as $[Sr_2CrO_2][Fe_2As_2]$, which is a homologous member of $[Sr_{n+1}M_nO_{3n-1}][Fe_2As_2]$. An almost single phase of the target material have been obtained by preparing the starting composition with the ~10% O-poor one. The estimated valence of Cr from the bond-valence sum and DFT calculation was nearly divalent, which differs from 32225 and 21113-type compounds containing trivalent 3d elements in the blocking layer. The Cr^{2+} ion would lead $3d^4$ configuration with high spin state due to the square-planar O coordination. The χ-T curve weakly increase with decreasing temperature, but does not obey the Curie-Weiss law at least below 390 K, which implies the Cr spins are cancelled out due to antiferromagnetic order in the CrO_2 plane as supported by the DFT calculation. The ρ-T curve does not show any anomalies but, the resistivity weakly increase below 100 K. A few percent of Cr substitution for the Fe site in FeAs layer may one of the reasons for the increment. The FeAs 21222-compound has the suitable Fe-Fe interlayer distance and $FeAs_4$ bond angle for superior superconductive property, therefore, it is expected to be the parent compound of high-T_c superconductors by further improvement of the constituent elements or doping methods.

Reference

[1] G. F. Chen, Z. Li, D. Wu, J. Dong, G. Li, W. Z. Hu, P. Zheng, J. L. Luo and N. L. Wang, Chin. Phys. Lett. **25**, 2235, (2008).

[2] M. Rotter, M. Tegel, and D. Johrendt, Phys. Rev. Lett. **101**, 107006 (2008).

[3] G. F. Chen, Z. Li, G. Li, W. Z. Hu, J. Dong, J. Zhou, X. D. Zhang, P. Zheng, N. L. Wang and J. L. Luo, Chin. Phys. Lett. **25**, 3403 (2008).

[4] G. Wu, H. Chen, T. Wu, Y. L. Xie, Y. J. Yan, R. H. Liu, X. F. Wang, J. J. Ying and X. H. Chen. J. Phys.: Condens. Matter **20**, 422201 (2008).

[5] X. C. Wanga, Q. Q. Liua, Y. X. Lva, W. B. Gaoa, L. X. Yanga, R. C. Yua, F. Y. Lia and C. Q. Jin, Solid State Commun. **128**, 538 (2008).

[6] D. R. Parker, M. J. Pitcher, P. J. Baker, I. Franke, T. Lancaster, S. J. Blundell, and S. J. Clarke, Chem. Commun. 2189 (2009)

[7] F. C. Hsu, J. Y. Luo, K. W. Yeh, T. K. Chen, T. W. Huang, P. M. Wu, Y. C. Lee, Y. L. Huang, Y. Y. Chu, D. C. Yan, and M. K. Wu. Proc. Natl. Acad. Sci. U.S.A. **105**, 14262 (2008).

[8] H. Ogino, Y. Matsumura, Y. Katsura, K. Ushiyama, S. Horii, K Kishio and J. Shimoyama, Supercond. Sci. Technol. **220**, 75008 (2009)

[9] Y. Kamihara, H. Hiramatsu, M. Hirano, R. Kawamura, H. Yanagi, T. Kamiya, and H. Hosono, J. Am. Chem. Soc. **128**, 10012 (2006).

[10] Z. Deng, X. C. Wang, Q. Q. Liu, S. J. Zhang, Y. X. Lv, J. L. Zhu, R. C. Yu and C. Q. Jin, EuroPhys. Lett. **87**, 37004 (2009).

[11] H. Ogino, Y. Katsura, S. Horii, K. Kishio and J. Shimoyama, Supercond. Sci. Technol. **22**, 085001 (2009)

[12] X. Zhu, F. Han, G. Mu, P. Cheng, B. Shen, B. Zeng, and H. H. Wen, Phys. Rev. B **79**, 220512(R) (2009)

[13] X. Zhu, F. Han, G. Mu, B. Zeng, P. Cheng, B. Shen, and H. H. Wen, Phys. Rev. B **79**, 024516 (2009).

[14] C. H. Lee, A. Iyo, H. Eisaki, H. Kito, M. T. Fernandez-Diaz, T. Ito, K. Kihou, H. Matsuhata, M. Braden and K. Yamada, J. Phys. Soc. Jpn. **77**, 083704 (2008).

[15] K. Kuroki, H. Usui, S. Onari, R. Arita and H. Aoki, Phys. Rev. B, **79**, 224511 (2009).

[16] Kenji Otzschi, Hiraku Ogino, Jun-ichi Shimoyama and Kohji Kishio, J. Low Temp. Phys. **117**, 729 (1999).

[17] W. J. Zhu and P. H. Hor, J. Am. Chem. Soc. **119**, 12398 (1997).

[18] F. Izumi and T. Ikeda, Mater. Sci. Forum **321-324**, 198 (2000).

[19] J. P. Perdew and Y. Wang, Phys. Rev. B **46**, 12947 (1992).

[20] I. D. Brown and D. Altermatt, Acta Cryst. B **41**, 244 (1985).

[21] N. E. Brese and M. O'Keeffe, Acta Cryst. B **47**, 192 (1991).

[22] H.Yanagi, T. Watanabe, K. Kodama, S. Iikubo, S. Shamoto, T. Kamiya, M. Hirano, and H. Hosono. J. Appl. Phys. **105**, 093916 (2009).

[23] H. Katsuraki and N. Achiwa, J. Phys. Soc. Jpn. **21**, 2238 (1966).

[24] private communication.

[25] M. Tegel, F. Hummel, Y. Su, T. Chatterji, M. Brunelli and D. Johrendt, arXiv:0911.0450v1.

[26] S. Matsuishi, Y. Inoue, T. Nomura, Y. Kamihara, M. Hirano and H. Hosono, New J. Phys. **11**, 025012 (2009).

[27] A. S. Sefat, D. J. Singh, L. H. VanBebber, M. A. McGuire, Y. Mozharivskyj, R. Jin, B. C. Sales, V. Keppens, D. Mandrus, arXiv:0903.5546v1.

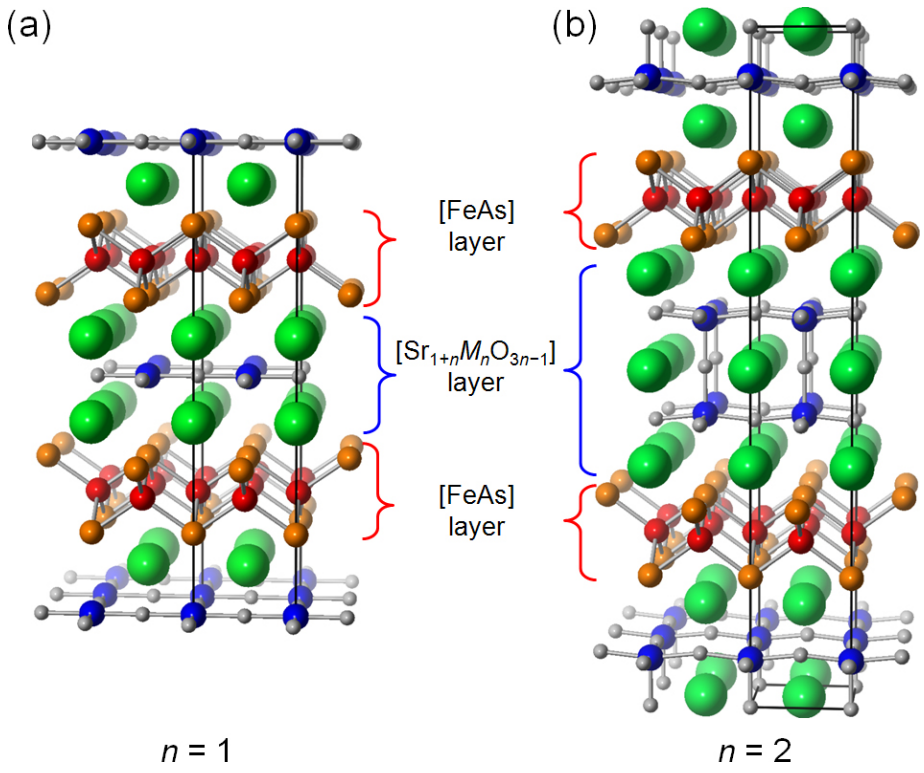

Figure 7-1. Crystal structure of $Sr_2MFe_2As_2O_2$ (a) and $Sr_3M_2Fe_2As_2O_5$ (b). Their structure formulae are generalized as $[Sr_{n+1}M_nO_{3n-1}]$ $[Fe_2As_2]$. Each unit cell is indicated by solid lines.

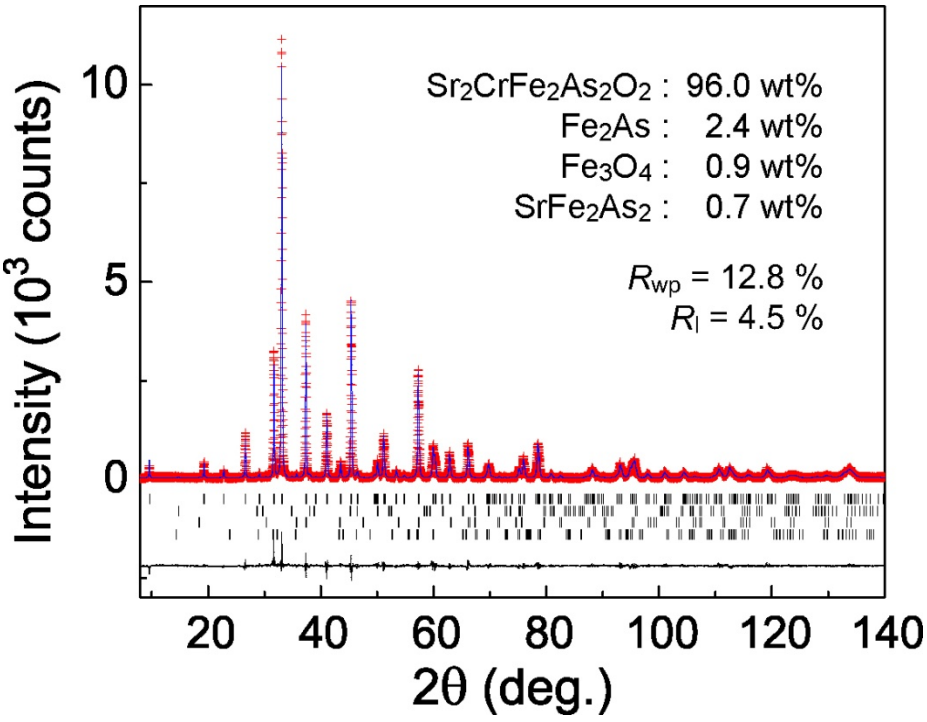

Figure 7-2. Rietveld fitting results of XRD pattern of $Sr_2CrFe_2As_2O_2$ at 300 K. Peak positions of the main phase, Fe_2As and Fe_3O_4 and $SrFe_2As_2$ are marked below the XRD pattern, respectively. The difference between observation and simulation is also shown with black line.

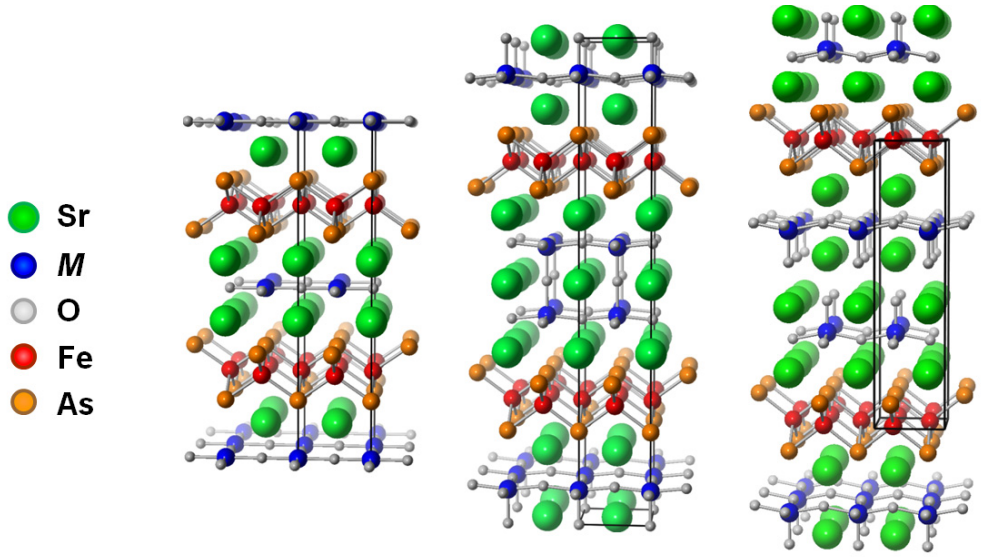

	21222-type (*n*=1)	32225-type (*n*=2)	21113-type
Interlayer distance	~0.92 nm	~1.3 nm	~1.6 nm
Species of *M*	Cr	Sc	Sc, Cr, V, (Mg,Ti)
O coordination number of *M*	4	5	5
Valence of *M* (BVS)	~2.1(Cr)	~3.1(Sc)	~3.0(Cr), ~2.7(V)

Figure 7-3. Comparison of FeAs interlayer distances, possible transition metal (*M*) species for the site in the blocking layer, O coordination number of *M*, and valences estimated by bond-valence sum (BVS) among Perovskite-related FeAs compounds.

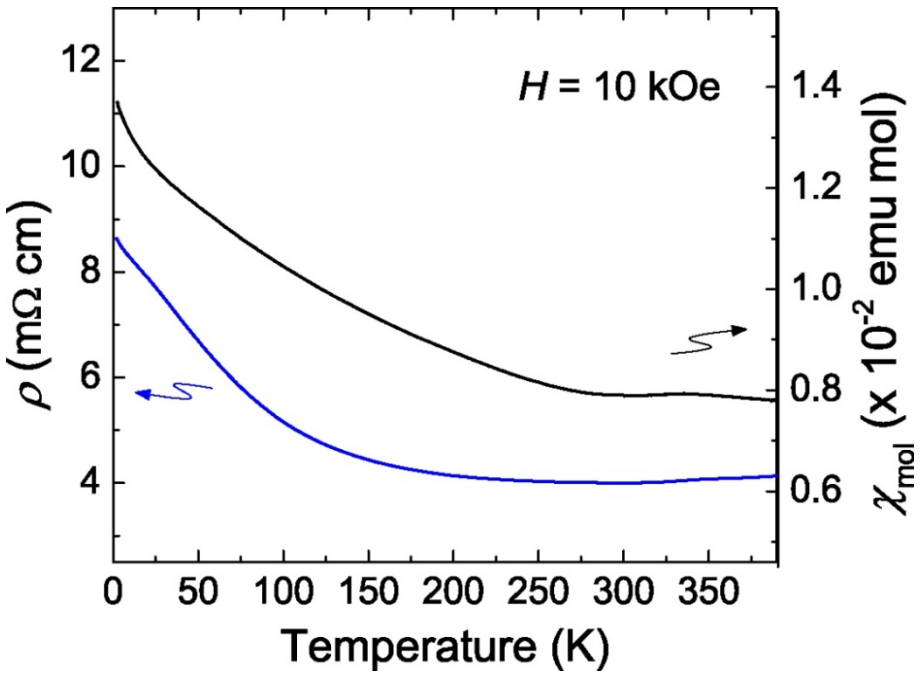

Figure 7-4. Temperature-dependent resistivity (ρ) and molar magnetic susceptibility (χ_{mol}) of $Sr_2CrFe_2As_2O_2$.

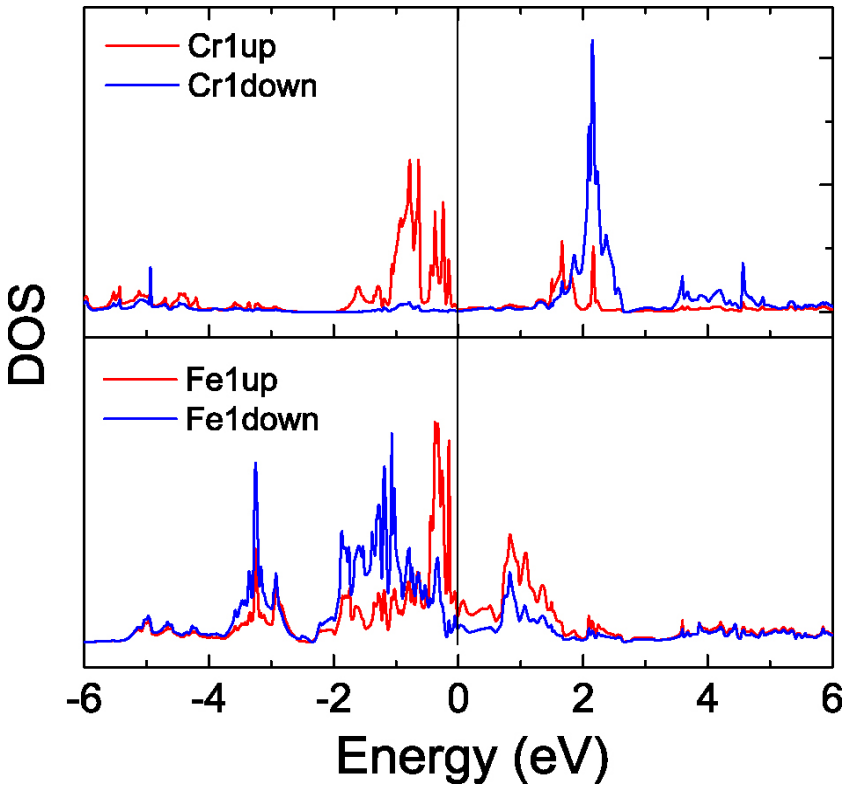

Figure 7-5. The partial density of state (DOS) of Cr and Fe in $Sr_2CrFe_2As_2O_2$ obtained by an *ab initio* calculation. Up and down stated was drown in red and blue, respectively.

Table 7-1. The structure parameters of $Sr_2CrFe_2As_2O_2$ at 300 K refined by Rietveld analysis. Crystal information; *I*4/*mmm* space group, Z = 2, *a* = 0.39965(3) nm, *c* = 1.84311(15) nm, *V* = 0.29438(4) nm^3.

Atom	site	Occ.	*x*	*y*	*z*	*B*(Å^2)
Sr	4*e*	1.0	0.5	0.5	0.08921(5)	0.41(2)
Cr	2*a*	1.0	0.5	0	0.25	0.14(4)
Fe	4*d*	1.0	0.5	0.5	0	0.31(3)
As	4*e*	1.0	0	0	0.17540(5)	0.47(2)
O	4*c*	1.0	0.5	0	0	2.33(15)

Chapter 8: General Conclusion

8.1. Conclusion

In this study, the crystal structures of various anion encaged C12A7 and *Ln*FeAsO-type Fe-based superconductors are investigated. For the C12A7, the distribution of encaged anions and the anion-induced cage deformation are experimentally determined for the first time. The large displacements of Ca ions enable to stabilize the incorporation of various anions even active anions. The cage deformation also realizes the electron incorporation with wide-range concentration, however, present study revealed that the cage deformation is nearly released due to the delocalization of electrons in the fully-electron-doped C12A7. Such the structural change would cause the metal-insulator transition accompanying drastic increase of the mobility at around 1×10^{21} cm^{-3} electron concentrations. In the crystal structure analysis of Fe-based superconductors, the tetragonal-orthorhombic phase transition was demonstrated in the parent LaFeAsO at ~160 K, which causes anomalies of resistivity and magnetic susceptibility. Theoretical calculations in this study demonstrates the structural phase transition stabilize the stripe-type antiferromagnetic Fe spin ordering, which likely to relate with the high-T_c superconductivity. The tetragonal-orthorhombic phase transitions are commonly observed in the parent phase of the other high-T_c Fe-based superconductors, even in the *Ae*FeAsF (Ae = Ca, Sr) of which structures are refined in the present study. The relation of the T_c and the crystal structure is one of the interesting topics in Fe-based superconductors, and the information is useful for the development of T_c. The substitution effects on the $FeAs_4$ tetrahedron shape were examined by the analysis of Co/F-substituted LaFeAsO and $AeFe_{1-x}Co_xAsF$ (*Ae* = Ca or Sr), and some suggestions for high-T_c superconductivity were described. In addition, a new 21222-type iron arsenide, $Sr_2CrFe_2As_2O_2$ was successfully fabricated. Although the superconductivity has

not been achieved yet, it would be a high-T_c superconductor by further improvements. The results of each chapter were summarized as follows:

Chapter 2

The distributions of encaged anions and the anion-induced cage deformation in O^{2-}, OH^- or H^- ion incorporated C12A7 (C12A7:O^{2-}, C12A7:OH^- and C12A7:H^-) were examined by the MEM/Rietveld analysis of the synchrotron XRD data. Each sample was carefully prepared and the stoichiometry was confirmed by IR spectroscopy, ESR and so on. The preliminary MEM analyses of both samples clearly revealed the large displacements of Ca^{2+} ions along the S_4 symmetry axis. Splitting of the Ca site of structure models drastically improved the Rietveld fitting results. The electron density distribution obtained by preliminary MEM analyses also indicated that the OH^- ion is located at the cage center, while the O^{2-} is not likely to occupy the center. The final refined results revealed the different behaviors of the encaged anion between O^{2-} or OH^- ion: An encaged O^{2-} ion induces large asymmetric displacement of two Ca^{2+} ions on the S_4 axis and occupies off-center and off-axis position (48*e* site). In contrast, OH^- ion induces small symmetric displacement of the Ca^{2+} ions, keeping itself at the center position of the cage (12*a* site). These differences would be caused mostly by the different charge states of the extra-framework anions. The position of encaged H^- ion has not been clarified yet due to the weak scattering ability and broadened electron distribution of the H^- ion, however, it is likely to occupy some positions deviated from the cage center and it seems to induce asymmetric Ca displacement like as the encaged O^{2-} ion.

Chapter 3

The crystal structure of fully electron-doped C12A7 electride was examined and the

relation with the metal-insulator transition was discussed. The C12A7 electride was prepared by Ti reduction process using a single crystal of stoichiometric C12A7. The C12A7 electride with metallic σ-*T* and 1500 $S \cdot cm^{-1}$ at 300 K were used for the XRD measurement. The electron density map obtained by the MEM/Rietveld analysis indicated the cage deformation dose not occurred in the prepared sample, which is contrast to the anion-incorporated C12A7 in the last chapter. This fact also indicates the doped electrons are delocalized and distribute each cage equivalently. Little electron density inner the cage also supports the extra-framework oxide ions are almost perfectly extracted by the reduction process. According to the theoretical calculation corresponding to the low doping concentration, the doped electrons are localized in the cage accompanied by the Ca displacements. However, above the critical electron concentration (~1×10^{21} cm^{-3}), the doped electron would be delocalized with the release of the Ca displacements. Such the structural shift contributes the metal-insulator transition with a sharp enhancement of the electron drift mobility from ~0.1 to 4 $cm^2\ V^{-1}\ s^{-1}$. The less structure deformation (i.e. high symmetry) in the highly electron-doped C12A7 also contributes the high conductive state.

Chapter 4

The crystal structures of the parent (unsubsituted) and 14% F-substituted LaFeAsO at low temperature were investigated. Some diffraction peaks of the parent samples were split into doublet below ~160 K. The Rietveld analysis demonstrated that the parent LaFeAsO, belonging to tetragonal (*P4/nmm*) symmetry at room temperature, transforms to orthorhombic (*Cmma*) phases below 160 K. The transition temperature agrees with the temperature where the resistivity suddenly decreases (T_{anom}), which indicates the structure transition is the origin of the resistivity anomaly. On the other hand, F-substituted sample keeps the tetragonal symmetry down to at least 25 K, which suggests that carrier doping suppresses the structural transition and

induces the superconductivity. The spin configurations in the orthorhombic LaFeAsO were calculated by DFT methods. The results demonstrate that stripe-type antiferromagnetic order of Fe is energetically stable at orthorhombic structure. The deduced double minimum potential arranged with the *a*- and *b*-axis length can elucidate the mechanism of the structure and magnetic phase transitions. The calculation results indicate that the antiferromagnetic order is strongly related with the orthorhombic structure, therefore, the magnetic fluctuation inducing the superconductivity would also accompany the structural deformation.

Chapter 5

The effects of substitution for Fe site (direct doping) and the other site (indirect doping) on the crystal structure of LaFeAsO were examined by Rietveld and MEM analysis of Co- and F-substituted LaFeAsO. The $LaFe_{1-x}Co_xAsO$ and $LaFeAsO_{1-x}F_x$ samples with x = 0, 0.06, 0.12 were fabricated, and the temperature-dependent resistivity measurements and the Rietveld analyses were conducted. Co-substitution reduces the *c*-axis length with slight change of *a*-axis length, while, F-substitution reduces both *a*- and *c*-axis lengths. The Co substitution for Fe site only decreases the distance between Fe plane and As plane without the structural change in the LaO layer. On the other hand, F substitution for the O site induces not only the decrease of Fe and As plane, but also other structural changes. The substitution of monovalent F^- ion for divalent O^{2-} ion weakens the Coulomb interaction with coordinating La ions, which enhances the interaction between the La ions and neighboring As ions. These effects result in the La displacement to FeAs layer, which would more or less introduce random structure distortion to the FeAs layer. Such the local structural change can be observed in the anisotropic distribution of La in MEM electron density map. In addition, the F substitution induces the decrease of interlayer distance between LaO and FeAs layers due to the enhancement of charge

polarizations between the layers, which more or less lowers two-dimension nature. Such the structural changes possibly relate with the high-T_c of the indirectly-doped *Ln*FeAsO.

Chapter 6

The superconductive properties of newly found superconductors, newly found members of the Fe-1111 superconductor family, *Ae*FeAsF (*Ae* = Ca or Sr) were discussed from the viewpoint of the crystal structure. The $AeFe_{1-x}Co_xAsF$ with x = 0, 0.06, 0.12 were prepared by solid state reactions. The ρ-T curves indicate that CaFeAsF (T_{cMAX} = 24 K) shows superior superconductive properties than SrFeAsF (T_{cMAX} = 7 K). The powder synchrotron XRD measurements at from 30 to 300 K revealed that the tetragonal to orthorhombic phase transitions as observed in LaFeAsO were observed at ~120 K for parent CaFeAsF and at ~180 K for parent SrFeAsF and the transition temperatures were in good agreement with kinks observed in the temperature-dependent resistivity curves. The transition temperature decreases with x, but the transition is sustained with Co substitution to x = 0.06 in both systems. The comparison of refined structure of each sample at 300 K suggests that distortion of the $FeAs_4$ tetrahedron from the regular tetrahedron mostly originates from the difference of Ae_4F tetrahedron size in the blocking layer. In the SrFeAsF, the $FeAs_4$ tetrahedron shape is flattened along a–b plane by the horizontal tension caused by the larger Sr_4F tetrahedron. On the other hand, $FeAs_4$ tetrahedron shape in the CaFeAsF is close to the regular one because of the smaller mismatch between the $FeAs_4$ and Ca_4F tetrahedrons. Co substitution further removes the distortion in the CaFeAsF contrast to the SrFeAsF. The higher superconductive property of CaFeAsF may caused by the high-symmetric $FeAs_4$ tetrahedron shape, which agrees with the "$FeAs_4$ bond angle rule". CaFeAsF exhibits the higest T_c among the Co-substituted Fe-based superconductors, therefore, the highest T_c would be broken by CaFeAsF if only the "indirect

doping" could be achieved.

Chapter 7

A 21222-type iron arsenide, $Sr_2CrFe_2As_2O_2$ containing a single CrO_2 layer in the blocking layer was successfully fabricated. The structure formula is denoted as $[Sr_2CrO_2][Fe_2As_2]$, which is a homologous member of $[Sr_{n+1}M_nO_{3n-1}][Fe_2As_2]$. An almost single phase of the target material have been obtained by preparing the starting composition with the ~10% O-poor one. The estimated valence of Cr from the bond-valence sum and DFT calculation was nearly divalent, which differs from 32225 and 21113-type compounds containing trivalent 3d elements in the blocking layer. The Cr^{2+} ion would lead $3d^4$ configuration with high spin state due to the square-planar O coordination. The χ-T curve weakly increase with decreasing temperature, but does not obey the Curie-Weiss law at least below 390 K, which implies the Cr spins are cancelled out due to antiferromagnetic order in the CrO_2 plane as supported by the DFT calculation. The ρ-T curve does not show any anomalies but, the resistivity weakly increase below 150 K. A few percent of Cr substitution for the Fe site in FeAs layer may one of the reasons for the increment. The FeAs 21222-compound has the suitable Fe-Fe interlayer distance and $FeAs_4$ bond angle for superior superconductive property, therefore, it is expected to be the parent compound of high-T_c superconductors by further improvement of the constituent elements or doping methods.

8.2. Suggested Future Research

As reported in the chapter 2 and 3, I experimentally examined detailed crystal structures of various anion-incorporated C12A7 crystals for the first time. It was revealed that distribution of the encaged anions and the manners of the displacements of framework Ca ions depend on

the anion species. It is noteworthy that incorporated O^{2-} ion induces the asymmetric Ca displacements, in contrast to the symmetric Ca displacements for the encaged OH^- ion. Such the structure information is important because it would be more or less related with the chemical stabilities of various anion-encaged C12A7 crystals, and the more detail information would helps to develop new functions of C12A7. For example, extend X-ray absorption fine structure (EXAFS) analysis on various anion-incorporated C12A7 would give us further insight into the cage deformation, not only the Ca displacements but also the Al displacement induced by encaged anions. In the case of H^- ion-incorporated C12A7, neutron diffraction is necessary to determine the accurate distribution of the incorporated H^- ion which is difficult to detect by XRD diffraction due to the low electron density. It should be noted that dynamic structures should also be examined by a time-resolved experiment to prove the bimodal Ca distribution is not caused by dynamic process but originated from the disordered structure.

This study also contributed to demonstrate that the MEM/Rietveld analysis is effective to find unexpected local structure changes in the crystal. Conventional MEM analysis is mainly applied to fullerene-related materials (e.g. higher fullerenes, metal-containing fullerenes) and molecularly-adsorbed nanoporous coordination polymers (e.g. CPL-1) to examine the complex structures and distributions of the accommodated atoms or molecules. In the chapter 2 and 5, the MEM/Rietveld analysis was applied to anion-incorporated C12A7 crystals and F-substituted LaFeAsO. These results suggest that local structure deformations induced by the anion incorporations and the atomic substitutions, which are difficult to find with conventional diffraction analysis, can be easily and visually detected by taking advantage of the MEM/Rietveld analysis. Especially, substitution effects on crystal structure have been still unrevealed in many functional materials such as Cu-based superconductors, *n*- or *p*-type semiconductors and so on. Therefore, it is expected that MEM/Rietveld analysis would be

convenient methods to examine disordered structures and local structure changes, although the obtained results should be verified by other experiments and calculations.

Discovery of new iron-based superconductors and improvements of T_c are eagerly anticipated to break the recent stagnation in the superconductivity research. In this study, I have succeeded in the fabrication of a new iron arsenide $Sr_2CrFe_2As_2O_2$ as reported in the chapter 7. Although it has not exhibited the superconductivity yet, it is expected to be high-T_c superconductors because most compounds including FeAs layer exhibit the superconductivity by proper substitution. One of the possible reasons why the $Sr_2CrFe_2As_2O_2$ does not show the superconductivity is the mixing of Fe and Cr of each layer. One of the ways to prevent the mixing is to replace the different divalent elements which hardly replace with Fe with the Cr site in the blocking layer. The FeAs 21222-compound has the suitable Fe-Fe interlayer distance and $FeAs_4$ bond angle for superior superconductive property, therefore further improvement of the constituent elements or doping methods would lead to the high-T_c superconductivity in this system and would contribute to the progress of iron-based superconductors.

Appendix

A-1. Outline of Rietveld Analysis

Rietveld anlaysis is a method by which crystals structures are determined from obtained powder XRD patterns. Crystal structure parameters of an initialized structure model are refined so that the simulated pattern well reproduces the observed XRD pattern. A powder XRD pattern includes crystallographic information as follows,

Peak positions → Lattice constants

Intensity ratios → Structure parameters (Occupancy, Fractional coordinates ..etc)

Peak profiles → Crystallite size, Lattice strain

Extinction rules → Crystal symmetry (Space group)

In the Rietveld analysis, above crystal information is obtained from the XRD pattern fitting. The intensity of an *i*th diffraction peak at angle $2\theta_i$ is calculated by a following formula,

$$Yc_i(x) = s\sum_K m_K \left|F(\boldsymbol{H}_K)\right|^2 P_K L(\theta_K) G(\Delta 2\theta_{iK}) + Y_b(2\theta_{iK}) \qquad \text{(A-1)}$$

where s is the scale factor, K is index of the *hkl* reflection, m_K is the multiplicity of Bragg reflection of K, $\boldsymbol{H}_K$ is a vector of the *hkl* refraction in the Reciprocal lattice space, $F(\boldsymbol{H}_K)$ is a structure factor of $\boldsymbol{H}_K$, P_K is a function for preferred orientation correction, θ_K is Bragg angle, $L(\theta_K)$ is the Lorentz-polarization factor, $G(\Delta 2\theta_{iK})(= G(2\theta_i - 2\theta_K))$ is the profile function, and Y_b is the background function, respectively. The crystal structure information within the unit cell are included in the crystal structure factor $F(\boldsymbol{H}_K)$, which is formulized as follows

$$F(\boldsymbol{H}_K) = \sum_j g_j (f_j + \Delta f_j' + i\Delta f_j'') T_j \exp\left[-2\pi i(hx_j + ky_j + lz_j)\right] \qquad \text{(A-2)}$$

where j is the number of atom in unit cell, g_j is the occupancy of jth atom, f_j is the atomic scattering factor, $\Delta f_j'$ and $\Delta f_j''$ are the real and imaginary parts of the anomalous scattering factor, T_j is the atomic displacement (Debye-Waller) factor, and x_j, y_j and z_j are the fractional coordinates, respectively.

A structure parameter set is determined so that the weighted error sum of squares $S(x)$, which is defined as following formula, is reduced as low as possible.

$$S(x) = \sum_i w_i \left[Yo_i - Yc_i(x) \right]^2 \tag{A-3}$$

The Yo_i and $Yc_i(x)$ represent the observed and calculated intensities of ith reflection peak, respectively. The weighting factor w_i is corresponding to $1/Yo_i$.

In the actual Reitveld analysis, the parameters s, $F(\boldsymbol{H}_K)$ and $G(\Delta 2\theta_{iK})$ in the equation A-1 are mainly refined for pattern fitting. There are some types for the profile function G according to how to combine Lorenzian and Gaussian components and how to asymmetrize the peak profile. The split Pearson VII function is adopted in the Rietveld program used in this study.

A-2. Theory of Maximum Entropy Method (MEM) Analysis

In the maximum entropy method, information entropy is defined as follows;

$$E = -\sum_{\boldsymbol{r}} \rho'(\boldsymbol{r}) \ln \frac{\rho'(\boldsymbol{r})}{\rho_0'(\boldsymbol{r})} \tag{A-4}$$

Here, $\boldsymbol{r}$ corresponds xyz coordinates and $\rho'(\boldsymbol{r})$ and $\rho_0'(\boldsymbol{r})$ are normalized electron densities and expressed by following formulae, respectively;

$$\rho'(\boldsymbol{r}) = \frac{\rho(\boldsymbol{r})}{\int \rho(\boldsymbol{r}) d\boldsymbol{r}} \quad , \quad \rho_0'(\boldsymbol{r}) = \frac{\rho_0(\boldsymbol{r})}{\int \rho_0(\boldsymbol{r}) d\boldsymbol{r}} \tag{A-5}$$

By maximizing the information entropy (E), the electron density distribution with highest "uncertainty", in other words, the most feasible electron density distribution would be obtained. (It should be noted that the information entropy has no relation with the entropy in thermal physics, although both entropies are concerned with measure of disorder or randomness.) However, the maximization of the entropy without any confinements would result in completely-homogeneous electron density distribution. In the normal MEM analysis, the

entropy is maximized under the following three constraints;

1. The difference between $F\mathrm{c}(\boldsymbol{H}_K)$ and $F\mathrm{o}(\boldsymbol{H}_K)$, which are calculated in the MEM analysis process are kept within an error σ_K which is estimated from the obtained structure factor $F\mathrm{o}(\boldsymbol{H}_K)$ in the preliminary Rietveld analysis.
2. The electron density should be constantly a positive value.
3. Specified symmetry of crystal structure is kept in the MEM cycles.

To maximize the entropy, the method of Lagrange multipliers is applied for the equation. Specifically, a function $Q(\boldsymbol{r})$ as shown in the following equation is obtained by adding the above-mentioned confinements to the formula of entropy (A-4).

$$Q(\boldsymbol{r}) = -\sum_{\boldsymbol{r}} \rho'(\boldsymbol{r}) \ln \frac{\rho'(\boldsymbol{r})}{\rho'_0(\boldsymbol{r})} - \frac{\lambda}{2}\left(\frac{1}{N}\sum_K \frac{\left|F\mathrm{c}(\boldsymbol{H}_K) - F\mathrm{o}(\boldsymbol{H}_K)\right|^2}{\sigma_K^2} - 1 \right) \tag{A-6}$$

The $F\mathrm{c}(\boldsymbol{H}_K)$ in the above equation can be calculated with $\rho_0'(\boldsymbol{r})$ by following formula;

$$F\mathrm{c}(\boldsymbol{H}_K) = V \int \rho'_0(\boldsymbol{r}) \exp(-2\pi i \boldsymbol{r}\cdot\boldsymbol{H}_K)\, d\boldsymbol{r} \tag{A-7}$$

Then, the variation method is applied to $Q(\boldsymbol{r})$ to obtain the extreme value where the entropy is maximized;

$$\frac{\partial Q(\lambda)}{\partial \rho'(\boldsymbol{r})} = 0 \tag{A-8}$$

In the actual MEM analysis, the electron density is determined by successive approximation process. A unit cell is divided into multiple grids and the electron density on each pixel is calculated per each cycle using the following formula.

$$\rho'(\boldsymbol{r}) = \exp\left[\ln \rho'_0(\boldsymbol{r}) + \lambda F_0 \sum \frac{1}{\sigma_K^2}\left(F\mathrm{o}(\boldsymbol{H}_K) - F\mathrm{c}(\boldsymbol{H}_K)\right)\exp(-2\pi i \boldsymbol{r}\cdot\boldsymbol{H}_K) \right] \tag{A-9}$$

The initial electron density $\rho_0(\boldsymbol{r})$ is set so that the total number of electrons, which is calculated from the total atomic number in a unit cell, is equally distributed to each pixel. The obtained

electron density $\rho'(\boldsymbol{r})$ calculated from equation A-9 is reset to $\rho_0'(\boldsymbol{r})$ and new density is calculated again. This cycle is repeated, and the final electron density distribution is determined when the difference between $F\mathrm{c}(\boldsymbol{H}_K)$ and $F\mathrm{o}(\boldsymbol{H}_K)$ converges within the range of σ_K.

A-3. Actual Process of MEM/Rietveld Analysis

Figure A-1 illustrates actual procedure of MEM/Rietveld analysis. In the preceding Rietveld analysis, a measured powder XRD pattern is fitted by a simulation pattern calculated from an assumed initial crystal structure model, based on equation A-1 and A-2. The structure parameters are optimized by the least square method so that the simulation pattern reproduces the observed one. Next, MEM analysis is carried out using the structure factors calculated from the determined structure model. The structure factors can be decomposed into "intensity component" and "phase component" for each reflection. Although the intensity component can be obtained from the experimental data, the phase component should be determined from the Rietveld analysis by optimizing the assumed structure model, which is called "phase problem". For the actual MEM analysis, the structure factor $F\mathrm{o}(\boldsymbol{H}_K)$ (equation A-6) is composed of the phase component determined from the preceding Rietveld analysis and the intensity component obtained from the XRD data, which is the reason why the obtained MEM electron density distribution contains hints reflecting the actual structure information. If some differences are found between the Rietveld and the MEM results, the MEM information is feedback to the initial Rietveld structure model, and above process is repeated again. This cycle is repeated until the Rietveld structure model and the MEM electron density distribution become consistent, although the R factors are important indicator to judge the final structure.

The MEM/Rietveld analysis resembles the conventional Fourier synthesis method, however, the former method generally give us more accurate electron density infromation than

the latter method. The Fourier synthesis method deduces the electron density distribution by the inverse Fourier transform of equation A-7, based on a following formula,

$$\rho(\boldsymbol{r}) = \frac{1}{V}\int F(\boldsymbol{H}_K)\exp(-2\pi i\boldsymbol{r}\cdot\boldsymbol{H}_K)\,d\boldsymbol{H}_K \qquad \text{(A-10)}$$

However, the integral range of $\boldsymbol{H}_K$ is finite due to limited measurement range of observed XRD pattern, which often deduces the noisy density distribution including negative density (so-called "ghost peaks"). On the other hand, the MEM analysis directly handles electron density so that the deduced electron density reproduces the observed XRD pattern, which deduces more accurate and presumable results without suffering the missing of high angle region.

The above-mentioned merits would further expand the application range of MEM analysis for various materials in the future.

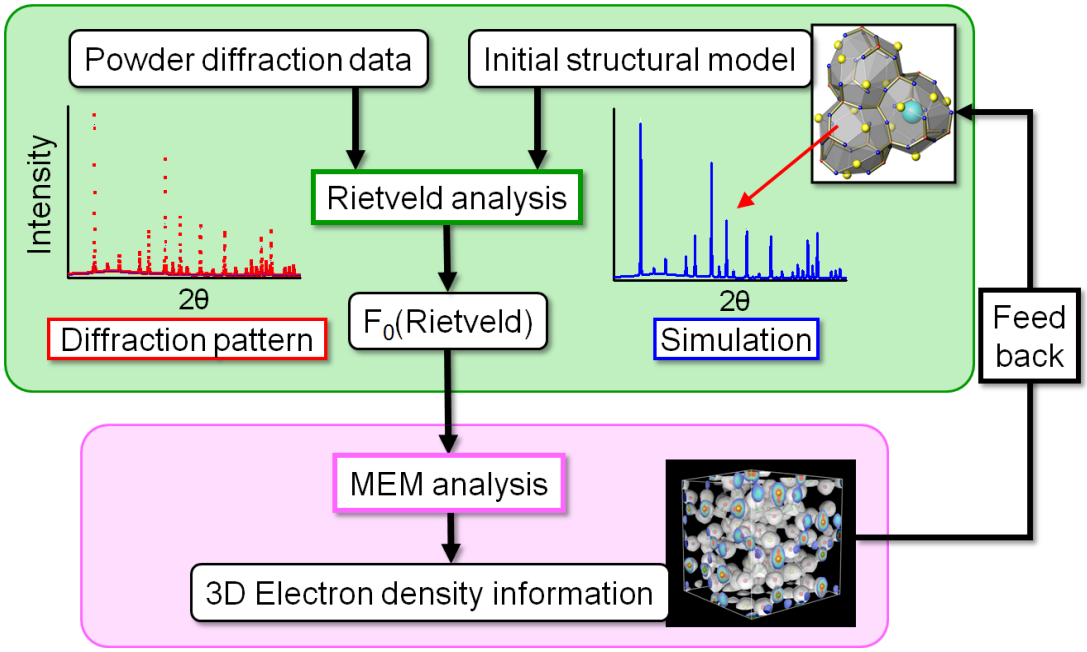

Figure A-1. Actual process of MEM/Rietveld analysis. In the Rietveld analysis, the simulation pattern can be calculated from equation A-1, where the structure factor $F(\boldsymbol{H}_K)$ is calculated from the structure model (red arrow) by using equation A-2. For the subsequent MEM analysis, the structure factor (Fo) is prepared by combining the intensity component obtained from the XRD data and the phase component determined from the preceding Rietveld analysis. In the next MEM/Rietveld cycle, the initial Rietveld structure model is modified in consideration of the obtained MEM electron density distribution.

Acknowledgements

This study was carried out in Hosono & Kamiya Laboratory at Tokyo Institute of Technology from April 2007 to March 2010. First of all, I would like to express my deepest gratitude to Professor Hideo Hosono for his proper guidance and sincere encouragement.

Also, I would like to express my sincere thanks and appreciation to Affiliate Professor Masahiro Hirano, Associate Professor Toshio Kamiya, Associate Professor Katsuro Hayashi, Associate Professor Sung-Wng Kim, Assistant Professor Satoru Matsuishi and Assistant Professor Hiroshi Yanagi (currently Associate Professor of Yamanashi University) for their kind and helpful guidance, discussions and suggestions.

I would like to express my sincere gratitude to Professor Satoshi Sasaki and Associate Professor Toshiyuki Atou at Tokyo Institute of Technology for their critical reading on this paper and for their valuable comments and suggestions on this study.

Further I am also much indebted to Hosono Project members including Dr. Kenichi Kawamura, Dr. Koichi Kajihara, Dr. Hiroshi Mizoguchi, Dr. Masashi Miyakawa, Dr. Kenji Nomura, Dr. Hidenori Hiramatsu, Dr. Yoichi Kamihara, Dr. Kentaro Kayanuma, Dr. Yoshitake Toda, Dr. Ki-Beom Kim, Dr. Quanxin Li and Dr. Seok-Gyu Yoon, for their kind supports and suggestions.

My heartfelt appreciation goes to Professor Masaki Takata, Dr. Kenichi Kato and Dr. Jung-Eng Kim of RIKEN and/or JASRI in SPring-8 for their active collaboration with the XRD measurements in BL02B2 and BL44XU and fruitful discussions. I also wish to express my science gratitude to Professor Yoshiki Kubota of Osaka Prefecture University for his kind suggestion with Rietveld and MEM analysis and allowance for usage of his Rietveld analysis programs.

I am deeply grateful to Professor Alexander L. Shluger and Dr. Peter. V. Sushko in

London University for the active collaboration with *ab initio* calculations and fruitful discussions.

I wish to thank Prof. Izumi and Dr. Momma in National Institute for Material Science (NIMS) for permission of the use of Rietveld analysis program “RIETAN2000” and 3D visualization program “VESTA”.

I wish to express my gratitude to students researching on Fe-based superconductors, Mr. Takumi Watanabe, Mr. Takashi Mine, Mr. Gifun Ryu, Mr. Takayoshi Katase, Mr. Yasunori Inoue, Ms. Saki Matsuo, Mr. Yoshiyuki Muraba and Mr. Ryo Date for their fruitful information exchanges and kind experimental supports.

I would like to acknowledge secretary Ms. Hidemi Mutai, Ms. Kanako Ochiai and Ms. Hiromi Kobayashi, and members of the S2 building including Dr. Akira Saito (currently at assistant professor of Kitami Institute of Technology), Mr. Eiji Motomitsu, Mr. Syunsuke Koide, Mr. Daisuke Yamashita and Mr. Yuji Yamamoto, Mr. Dong-Hee Lee, Mr. Terumasa Shimoyama, Mr. Yutaka Adachi, Mr. Toshihiro Yoshizumi, and members of my class including Mr. Yukimasa Nishio, Mr. Naoto Ando, Mr. Hiroki Muramatsu, Mr. Ryuto Kawamura, Ms. Maiko Kikuchi, Mr. Kentaro Tajima and all the other members of Hosono & Kamiya Laboratory for their kind help in this study.

Finally I deeply appreciate all my family and friends.

March 2010

Takatoshi Nomura

Publication List

Paper include in this thesis

1. Metallic State in a Lime-Alumina Compound with Nanoporous Structure

Sung-Wng Kim, Satoru Matsuishi, **Takatoshi Nomura**, Yoshiki Kubota, Masaki Takata, Katuro Hayashi, Toshio Kamiya, Masahiro Hirano and Hideo Hosono, Nano Letters, **7**, 1138 (2007).

2. Anion Incorporation-induced Cage Deformation in $12CaO \cdot 7Al_2O_3$ Crystal,

Takatoshi Nomura, Katuro Hayashi, Yoshiki Kubota, Toshio Kamiya, Masahiro Hirano, Masaki Takata and Hideo Hosono, Chemistry Letters, **36**, 902 (2007).

3. Crystallographic Phase Transition and High-T_c Superconductivity in LaFeAsO:F

Takatoshi Nomura, Sung-Wng Kim, Yoichi Kamihara, Masahiro Hirano, Peter V Sushko, Kenichi Kato, Masaki Takata, Alexander L Shluger and Hideo Hosono, Supercond. Sci. Technol. **21**, 125028 (2008)

4. Tetragonal-Orthorhombic Phase Transition and F-doping Effects on the Crystal Structure in the Iron-based High-T_c Superconductor LaFeAsO

Takatoshi Nomura, Sung-Wng Kim, Yoichi Kamihara, Masahiro Hirano, Peter V Sushko, Kenichi Kato, Masaki Takata, Alexander L Shluger and Hideo Hosono, J. Phys. Soc. Jpn. Suppl. C **77**, 32 (2008).

5. Superconductivity Induced by Co-Doping in Quaternary Fluoroarsenide CaFeAsF

Satoru Matsuishi, Yasunori Inoue, **Takatoshi Nomura**, Hiroshi Yanagi, Masahiro Hirano and Hideo Hosono, J. Am. Chem. Soc. **130** 14428 (2008).

6. Cobalt-Substitution-Induced Superconductivity in a New Compound with ZrCuSiAs-Type Structure, SrFeAsF

Satoru Matsuishi, Yasunori Inoue, **Takatoshi Nomura**, Hiroshi Yanagi, Masahiro Hirano and Hideo Hosono, J. Phys. Soc. Jpn. **77**, 113709 (2008).

7. Effect of 3d Transition Metal Doping on the Superconductivity in Quaternary Fluoroarsenide CaFeAsF

Satoru Matsuishi, Yasunori Inoue, **Takatoshi Nomura**, Hiroshi Yanagi, Masahiro Hirano and Hideo Hosono, New J. Phys. **11**, 025012 (2009).

8. Comparison of Crystal Structures and Effects of Co Substitution in a New Member of Fe-1111 Superconductor Family *Ae*FeAsF (*Ae* = Ca and Sr): a Possible Candidate for Higher-T_c Superconductor

Takatoshi Nomura, Yasunori Inoue, Satoru Matsuishi, Masahiro Hirano, Jung-Eun Kim, Kenichi Kato, Masaki Takata and Hideo Hosono, Supercond. Sci. Technol. **22**, 055016 (2009).

9. Electromagnetic Properties of Undoped LaFePnO (*Pn* = P, As)

Yoichi Kamihara, Takumi Watanabe, **Takatoshi. Nomura,** Sung-Wng Kim, Toshio Kamiya, Masahiro Hirano and Hideo Hosono, J. Phys.: Conf. Ser., **150**, 052090 (2009)

Reviews

1. 鉄系超伝導物質（物理学会誌 小特集：鉄系超伝導体）

細野秀雄、松石聡、**野村尚利**、平松秀典、日本物理学会誌 **11**, 807 (2009).

2. Tetragonal-Orthorhombic Phase Transition of LaFeAsO; Relevant to High-T_c Superconductivity

Takatoshi Nomura, Hosono Hideo, SPring-8 Research Frontiers, to be published.

International Conference

1. Electron Density Distribution in Metallic $12CaO{\cdot}7Al_2O_3$ Crystal

Takatoshi Nomura, Katuro Hayashi, Yoshiki Kubota, Toshio Kamiya, Masahiro Hirano, Masaki Takata and Hideo Hosono, Euro Mater. Res. Soc., Acropolis Congress Center, Nice, France, May 29-June 2, 2006

2. Tetragonal-Orthorhombic Phase Transition and the Superconductivity in LaFeAsO

Takatoshi Nomura, Sung-Wng Kim, Yoichi Kamihara, Masahiro Hirano, Peter V. Sushko, Kenichi Kato, Masaki Takata, Alexander L. Shluger and Hideo Hosono**,** International Symposium on Fe-Oxipnictide Superconductors, Venue Kokuyo Hall, sinagawa, Tokyo, Japan, June 28-29, 2008

3. Phase Transition and Electron Density Distribution in High-T_c Superconductor $LaFeAsO_{1-x}F_x$

Takatoshi Nomura, Sung-Wng Kim, Yoichi Kamihara, Masahiro Hirano, Peter V. Sushko, Kenichi Kato, Masaki Takata, Alexander L. Shluger and Hideo Hosono, Mater. Res. Soc., Hynes Convention Center, Boston, USA, Dec. 1-5, 2008

Domestic Conference

1. MEM/Rietveld 法によるナノポーラス結晶 $12CaO{\cdot}7Al_2O_3$ のケージ内陰イオンの可視化

野村尚利、林克郎、久保田佳基、神谷利夫、高田昌樹、細野秀雄、日本セラミックス協会 2006 年年会、1J23、東京大学、2006 年 3 月 14 日

2. ナノポーラス結晶 $[Ca_{24}Al_{28}O_{64}]^{4+}{\cdot}4X^-$ の包接陰イオンにより誘起される格子緩和とケージ内電子密度分布

野村尚利、林克郎、久保田佳基、金聖雄、神谷利夫、高田昌樹、細野秀雄、日本セラミックス協会 2007 年年会、3J04、武蔵工業大学、2007 年 3 月 23 日

3. O^{2-} および OH^- イオンを包接した $12CaO{\cdot}7Al_2O_3$ 結晶の異なるケージ構造変化と包接陰イオン分布

野村尚利、林克郎、神谷利夫、久保田佳基、高田昌樹、平野正浩、細野秀雄、日本セラミックス協会 2008 年年会、1L20、長岡技術科学大学、2008 年 3 月 20 日

4. 新規層状超伝導化合物 LaFeAsO の正方晶 - 斜方晶構造相転移

野村尚利、金聖雄、神原陽一、平野正浩、Sushko Peter V.、加藤健一、高田昌樹、Shluger Alexander L.、細野秀雄、2008 年秋季第 69 回応用物理学会学術講演、4p-G-1、中部大学、2008 年 9 月 4 日

5. 新規 Fe-1111 系超伝導体 $AeFe_{1-x}Co_xAsF$ (Ae = Ca,Sr)の結晶構造と超伝導特性

野村尚利、井上泰徳、松石聡、金廷恩、加藤健一、高田昌樹、平野正浩、細野秀雄、日本セラミックス協会 2009 年年会、2C29、東京理科大学、2009 年 3 月 17 日